



FRIEDRICH-SCHILLER-
UNIVERSITÄT
JENA

GENERATION OF SPATIO-TEMPORAL
STRUCTURED HIGH-ORDER HARMONICS

DISSERTATION

zur Erlangung des akademischen Grades

doctor rerum naturalium

(Dr.rer.nat)

vorgelegt dem Rat der

PHYSIKALISCH-ASTRONOMISCHEN FAKULTÄT

der

FRIEDRICH-SCHILLER-UNIVERSITÄT JENA

von

M.Sc. Björn Minneker

geboren am 15.06.1994 in Essen

GUTACHTER:

1. Prof. Dr. Stephan Fritzsche (Friedrich-Schiller-Universität Jena)
2. Prof. Dr. Dejan B. Milošević (University of Sarajevo)
3. Dr. Emilio Pisanty (King's Collage London)

TAG DER DISPUTATION: 6 JULI 2023

ABSTRACT

Strong laser fields are essential for exploring laser-atom dynamics in modern physics. High-order harmonic generation (HHG) represents a prominent strong-field process in which an ionized electron accelerates with the electric field of an incident laser and subsequently recombines with its parent ion. The accelerated electron eventually emits a photon within the recombination process, which yields high-order harmonic radiation at the macroscopic scale. Recent advances in laser technology enable the generation of intense mid-infrared laser fields. These new laser sources extended the parameter range of HHG significantly toward the weakly relativistic regime in which the magnetic field of the incident laser field contributes to the process. This dissertation provides a theoretical model of HHG, which is a formal extension of the well-known strong-field approximation toward the weakly relativistic regime. Generally, the model considers arbitrarily spatially structured light fields, in contrast to current approaches, and therefore provides the opportunity to investigate twisted light beams within the weakly relativistic regime. The developed model explicitly considers an elliptically polarized plane wave laser beam as an example. In addition, more sophisticated laser fields are considered and briefly discussed afterward. In addition, this dissertation investigates phase matching in the context of HHG, which is afflicted with a low conversion efficiency of less than 0.1%. Finding suitable sets of external parameters under which the conversion efficiency is respectively high is therefore of substantial interest to the strong-field community. An analytic expression of the critical intensity is derived that fulfills the phase-matching condition for an arbitrary set of initial parameters. The approach is limited to hydrogen-like noble gases and linearly polarized Gaussian laser pulses with arbitrary laser field parameters that incorporate the commonly utilized configurations. The analytical error compared to numerical computations is less than 1%, while the computation time improves by four to six orders of magnitude.

ZUSAMMENFASSUNG

Starke Laserfelder sind für die Erforschung der Laser-Atom-Dynamik in der modernen Physik unerlässlich. Die Erzeugung von Harmonischen höherer Ordnung (HHG) ist ein bedeutender Starkfeldprozess, bei welchem ein ionisiertes Elektron durch das elektrische Feld des einfallenden Lasers beschleunigt wird und anschließend mit seinem Mutterion rekombiniert. Das beschleunigte Elektron emittiert bei der Rekombination schlussendlich ein Photon, welches auf makroskopischer Ebene höherer harmonische Strahlung entspricht. Jüngste Fortschritte in der Lasertechnologie ermöglichen die Erzeugung intensiver Laserfelder im mittleren Infrarotbereich. Diese neuen Laserquellen erweitern den Parameterbereich der HHG erheblich bezüglich des schwach relativistischen Bereichs, in welchem das Magnetfeld des einfallenden Laserfeldes zu diesem Prozess beiträgt. In dieser Dissertation wird ein theoretisches Modell der HHG vorgestellt, welches eine formale Erweiterung der bekannten Starkfeld-Näherung auf den schwach relativistischen Bereich darstellt. Generell kann das Modell im Gegensatz zu aktuellen Ansätzen beliebig räumlich strukturierte Lichtfelder berücksichtigen und bietet somit die Möglichkeit, verdrehte Lichtstrahlen im schwach relativistischen Regime zu untersuchen. Das hier entwickelte Modell betrachtet explizit einen elliptisch polarisierten ebenen Laserstrahl als Beispiel. Darüber hinaus werden auch komplexere Laserfelder betrachtet und anschließend kurz diskutiert. Darüber hinaus wird in dieser Dissertation die Phasenanpassung im Kontext der HHG untersucht, die mit einer geringen Konversionseffizienz von weniger als 0,1% behaftet ist. Die Suche nach geeigneten externen Parametern, unter denen die Konversionseffizienz entsprechend hoch ist, ist daher von großem Interesse für die Starkfeldgemeinde. Es wird ein analytischer Ausdruck für die kritische Intensität abgeleitet, der die Bedingung der Phasenanpassung für einen beliebigen Satz von Anfangsparametern erfüllt. Der Ansatz ist auf wasserstoffähnliche Edelgase und linear polarisierte Gauß-Laserpulse mit beliebigen Laserfeldparametern beschränkt, die die üblicherweise verwendeten Konfigurationen umfassen. Der analytische Fehler im Vergleich zu numerischen Berechnungen ist kleiner als 1%, während die Berechnungszeit um vier bis sechs Größenordnungen verbessert wird.

ACKNOWLEDGEMENTS

This dissertation would not have been possible without the people who have supported me in different ways over the past years and during the time of writing. First and foremost, I want to thank Prof. Stephan Fritzsche for giving me the opportunity to work on this research topic and for our discussions.

Likewise, I would like to thank all those who have been part of the Atomic Theory Group in Jena during my Ph.D. time. Many helpful discussions and remarks during our seminars and group meetings have advanced my work further than it would have been possible by a single person.

Special thanks go to Birger Böning, who introduced me to strong-field atomic physics and supported me with fruitful discussions and remarkable questions.

Additionally, I thank Darvin Wanisch and Romain Soguel, who started their Ph.D. with me during the beginning of the corona pandemic, for their mutual support and enjoyable evenings.

I would like to thank my parents, Peer and Andrea Minneker, who have always supported me in achieving my goals in life, of which the Ph.D. is only one part.

Finally, I thank Sophie-Marie Minneker, Birger Böning, Shreyas Ramakrishna, Giorgio Visentin, Felix Karbstein, Robert Klas, and Laura Lucia Zech who provided major improvements to the readability of this dissertation and supported me during the turbulent time while writing this dissertation.

PUBLICATIONS

The material presented in this dissertation was contributed to the following publications:

- *Generalized nondipole strong-field approximation of high-order harmonic generation*
Minneker, B.; Böning, B.; Fritzsche, S.
[Phys. Rev. A 2022, 106, 053109.](#) [1]
- *Critical laser intensity of phase-matched high-order harmonic generation in noble gases*
Minneker, B.; Klas, R.; Rothhardt, J.; Fritzsche, S.
[Photonics 2023, 10 \(1\), 24.](#) [2]

The following publications and submitted manuscripts do not contain dissertation work:

- *Torus-knot angular momentum in twisted attosecond pulses from high-order harmonic generation*
Minneker, B.; Böning, B.; Weber, A.; Fritzsche, S.
[Phys. Rev. A 2021, 104, 053116.](#) [3]
- *Generation of elliptically polarized high-order harmonic radiation with bi-elliptical two-color laser beams*
Weber, A.; Böning, B.; Minneker, B.; Fritzsche, S.
[Phys. Rev. A 2021, 104, 063118.](#) [4]
- *Nondipole strong-field approximation for above-threshold ionization in a few-cycle pulse*
Furekh, D.; Minneker, B.; Fritzsche, S.
[Phys. Rev. A 2023, 107, 053102](#) [5]

ACRONYMS

Acronym	Definition
ADK	Ammosov-Delone-Krainov
arb.	arbitrary units
ATI	Above-threshold ionization
GN-SFA	Generalized nondipole strong-field approximation
TDSE	Time-dependent Schrödinger equation
HH	High-order harmonic
HHG	High-order harmonic generation
MPI	Multiphoton ionization
PM	Phase matching
PPT	Perelomov-Popov-Terent'ev
SFA	Strong-field approximation
SPA	Saddle-point approximation
TI	Tunnel ionization
YI	Yudin Ivanov

TOOLS AND METHODS

The content presented in this dissertation consists, to a large extent, of purely analytical work. Wherever results for specific physical parameters are shown, computational tools have been employed to evaluate the respective analytical expressions for numerical values. In particular, *Wolfram Mathematica* v. 12 (Wolfram Research, Inc., 2016) [6] and *Inkscape* [7] were utilized for the generation of several graphics, while the programming language *Julia* [8] was predominantly used in numerical computations.

CONTENTS

LIST OF FIGURES	xv
LIST OF TABLES	xvii
1. INTRODUCTION	1
2. DESCRIPTION OF STRUCTURED LIGHT FIELDS	5
2.1. Maxwell equations	5
2.2. Plane wave solution of the Helmholtz equation	8
2.3. Laser fields in the dipole approximation	11
2.3.1. Plane wave beams	11
2.3.2. Plane wave pulses	11
2.4. Spatially structured light fields	13
3. THEORETICAL APPROACH TO STRONG-FIELD PROCESSES	17
3.1. Overview	17
3.2. Atoms in intense electromagnetic fields	18
3.3. Multiphoton and tunnel ionization	21
3.3.1. PPT theory	22
3.3.2. ADK theory	23
3.4. High-order harmonic generation	24
3.4.1. Dipole Volkov states	26
3.4.2. Gauge invariant strong-field transition amplitude	27
3.4.3. Strong-field approximation	33
3.4.4. Quantum Orbit approach	38
4. HIGH-ORDER HARMONIC GENERATION BY SPATIALLY STRUCTURED LIGHT	43
4.1. Electron dynamics in weakly relativistic laser fields	45
4.1.1. Influence of the spatial laser structure	46
4.1.2. Nondipole Volkov states	47
4.2. Strong-field transition amplitudes beyond the dipole approximation	50

4.3. Generalized nondipole strong-field approximation	53
4.3.1. Nondipole matrix element	57
4.3.2. Saddle-point approximation	61
4.3.3. Results	65
4.4. Elliptically polarized plane wave beam	68
4.4.1. Parameters of the generalized nondipole strong-field approximation	68
4.4.2. Discussion	69
4.5. Outlook: Spatially structured light beams	71
5. CRITICAL INTENSITY OF HIGH-ORDER HARMONIC GENERATION	75
5.1. Model and Method	76
5.1.1. Phase-matching of high-order harmonic radiation	77
5.1.2. Critical intensity in the ADK theory	78
5.1.3. Critical intensity in the PPT theory	85
5.2. Results and Discussion	88
5.2.1. Accuracy of the critical intensity: ADK theory	89
5.2.2. Accuracy of the critical intensity: PPT theory	90
5.2.3. Comparison of the critical intensities: ADK - PPT	91
5.2.4. Comparison of the computation time: Analytical - Numerical . . .	93
5.3. Outlook: Negligible ionization in noble gases	93
6. SUMMARY AND CONCLUSION	97
A. EIGENSTATES OF THE ENERGY OPERATOR	101
B. NONDIPOLE VOLKOV STATES	103
C. NONDIPOLE MATRIX ELEMENT	107
D. ACCURACY CRITICAL INTENSITY	109
BIBLIOGRAPHY	111

LIST OF FIGURES

1.1. High-order harmonic generation setup	3
2.1. Linearly polarized plane-wave beam	8
2.2. Gaussian plane-wave pulses	12
2.3. Bessel beam	16
3.1. Strong-field setup and processes	18
3.2. Strong-field ionization processes	19
3.3. Three-step model of HHG	21
3.4. HHG spectrum within the Lewenstein model	36
3.5. Saddle points within the quantum orbit approach	40
3.6. HHG spectrum within the quantum orbit approach	41
4.1. Schematic comparison of theoretical models	45
4.2. Electron dynamics in spatially structured light fields	46
4.3. HHG spectrum from the generalized nondipole SFA	70
4.4. Ratio of the atomic dipole moment for the generalized nondipole SFA and the dipole SFA	72
4.5. Contribution of the temporal nondipole Volkov phase from a Bessel beam	74
5.1. HHG setup and critical ionization probability	77
5.2. Approximation of a Gaussian pulse envelope	83
5.3. Accuracy critical intensity: ADK	88
5.4. Accuracy critical intensity: PPT	89

5.5. Density plot of the critical intensity within the ADK and PPT theory . .	92
5.6. Ionization intensity of noble gases	94

LIST OF TABLES

3.1. Strong-field ionization processes	20
5.1. Parameters to compute the critical intensity of hydrogen-like noble gases	82
D.1. Accuracy critical intensity: ADK	109
D.2. Accuracy critical intensity: PPT	110

“Remember to look up at the stars and not down at your feet. Try to make sense of what you see and wonder about what makes the universe exist. Be curious.”

— Stephan Hawking

CHAPTER 1.

INTRODUCTION

“If you are not completely confused by quantum mechanics, you do not understand it”

— John Wheeler

The interactions of light and matter are associated with the fundamental understanding of our everyday life. Essentially, everything one can see denotes a direct consequence of this interaction, apart from gravitation and nuclear forces. The nature of light and the constituents of matter have therefore captured the imagination and inspiration of people ever since. From the 19th century to the present, science has revealed increasingly intimate details about the nature of reality. Faraday and many others discovered light as an electromagnetic wave during their studies on the interplay of electric and magnetic fields on itself in the vicinity of charged particles [9]. The investigations converged in 1845 to Maxwell’s classical field theory, which accurately describes the dynamics of the respective electric, magnetic, and electromagnetic fields [10]. Since then, light has been understood as an electromagnetic wave. The Maxwell equations, complemented by equations that account for the state of matter, explain many macroscopic phenomena associated with light-matter interactions. As science proceeded, the limitations of Maxwell’s classical field theory became predominantly visible within the microscopic regime. A famous example is the photoelectric effect, in which a metal plate emits electrons as a light source illuminates the plate. This phenomenon could not be explained by the wave properties of light until Einstein resolved this riddle in 1905 [11]. Einstein forsakes the interpretation of light as a continuous wave to describe it by discrete packages, or quanta, of well-defined energy $E = h\nu$ with the frequency of light ν and Planck’s constant h [12]. The quantization of light indicates the initiation of many discoveries, including a quantized theory of the constituents of matter. These discoveries condense to the Schrödinger equation [13] and later to the Dirac equation [14], which describe

the dynamics of spin 1/2 particles like electrons and later protons and neutrons. These theories describe the stability and structure of atoms so that the attraction between the electrons and the nucleus is associated with the electrostatic force. Further discoveries reveal that electrons can only exist in states of well-defined quantized energy near an atomic nucleus. Pauli discovered a unique property of quantum mechanics, namely that every well-defined quantum state is simultaneously associated with at most a single fermion [15].

However, this approach cannot directly explain the details of these quantized states, like the energetic structure. How can one measure these structures or even influence and control them? Questions similar to those have inspired physicists since the beginning of quantum mechanics. In the middle of the 20th century, the answers became accessible by one of the greatest inventions of that time, maybe ever. The laser, invented by Maiman in 1960, provides a bright and coherent light source with wavelengths $\lambda = \omega/2\pi c$ of extraordinarily narrow bandwidth. This powerful tool enables the decoding of a variety of processes in the microscopic regime. Photoionization represents one of these processes and is also closely related to the photoelectric effect. Photoionization essentially describes a process in which a bound electron absorbs a finite number of photons, or light quanta, to overcome the respective binding potential of the nucleus. The necessary amount of energy an electron needs can originate from single, high-energetic, or many low-energetic photons. The ionization probability drastically decreases with an increasing number of absorbed photons. An increase in the classical electromagnetic field amplitude corresponds to an increase in the photon density per unit volume, which compensates for the decrease in the absorption probability. Further increasing the electric and magnetic amplitude of the laser field directs to the regime of *strong-field atomic physics*.

In his 1964 work [16], Keldysh proposed a method to classify the strong-field regime by three parameters. These parameters are the incident laser field intensity I_0 , the wavelength λ , and the ionization potential of the atomic species I_p . One may observe various processes within the strong-field regime by irradiating a gas cloud of atomic targets with an intense laser field. Generally, these processes separate into two categories: First, electron emissions, such as *strong-field ionization*, and second, photon emission processes such as *high-order harmonic generation* (HHG) [17]. The simplest form of strong-field ionization occupies a particular position as it is the building block for more complex processes such as non-sequential double ionization [18] in which two electrons are nonsequentially ionized or HHG. HHG denotes a process in which an initially ionized electron propagates throughout the continuum and, eventually, recombines radiatively

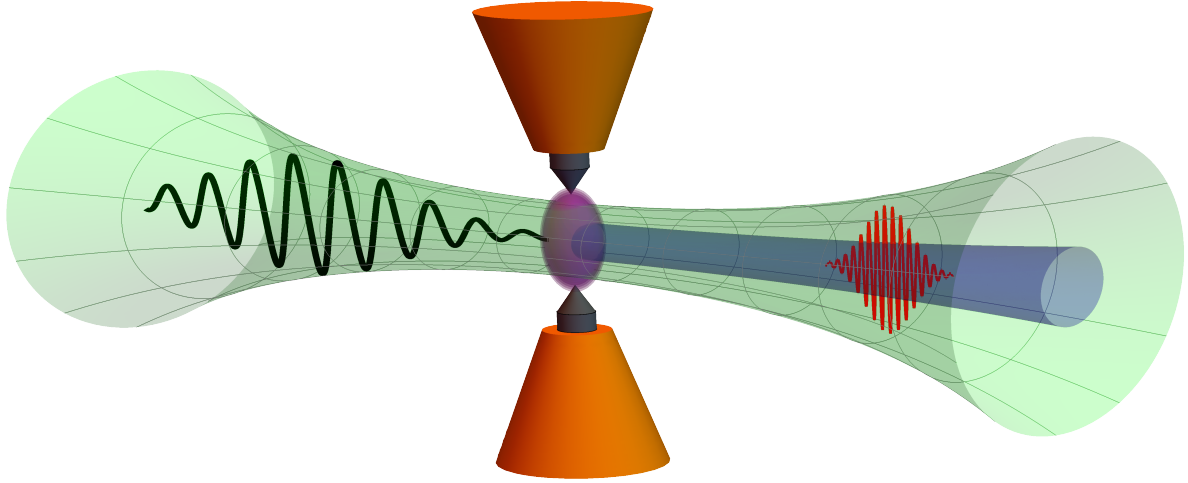


Figure 1.1.: High-order harmonic generation setup with the incident laser field (green), the gas emitter (orange), the gas cloud (purple), and the high-order harmonic radiation (blue). The incident laser pulse is colored in black, while the emitted High-order harmonics pulse is shown in red.

with its parent ion. During propagation in the continuum, the electron receives energy from the electric field. The electron's kinetic energy finally converts into a single high-order harmonic photon within the recombination process. Figure 1.1 illustrates a classical HHG setup, which has been extensively utilized in previous decades and helped to significantly improve our understanding of laser-atom interactions.

Photons generated in the HHG process preserve the coherence of the incident laser field and further lead to extraordinarily short laser pulses [19]. The pulse length of these laser pulses, which lies at the attosecond time scale, in combination with its coherency, provides an excellent instrument to probe matter on its natural time scale [20–22]. The strong-field community has always been interested in developing experimental and theoretical methods to achieve shorter pulse lengths, which are directly associated with large high-order harmonic photon energies. These high photon energies are usually realized by either increasing the field intensity or the wavelength of the respective incident laser field. The generation of high-order harmonics under normal conditions is well described within the nonrelativistic regime. However, for a drastically increased intensity or wavelength of the incident laser field, the nonrelativistic description of HHG is not valid anymore [23, 24]. Recent advances in laser technology provide high-intensity laser systems in the mid-infrared regime, which induce weakly relativistic dynamics within the generation of high-order harmonics [25, 26]. Consequently, new models and methods that incorporate these weakly relativistic contributions need to be investigated to gain deeper insight into the underlying dynamics.

This dissertation provides a generalized version of the dipole strong-field approximation (SFA) towards the weak relativistic limit. While many other nondipole approaches are limited to a tailored laser structure, the framework developed in this dissertation represents a proper generalization of the dipole SFA as the structure of the incident laser field remains arbitrary. In addition, this dissertation provides an analytical approach to compute the critical intensity above which phase-matched HHG is no longer possible. The error of the analytical expression is less than 1% for a wide range of parameters compared to numerical computations. This astonishing accuracy may simplify many experimental and theoretical investigations in the future.

Structure of the dissertation

Chapter 2 begins with the Maxwell equations, which generally describe the dynamics of light in Sec. 2.1, followed by the introduction of plane waves in Sec. 2.2. Afterward, Sec. 2.3 mentions laser fields in the dipole approximation, while spatially structured light fields are generally introduced in Sec. 2.4. Chapter 3 discusses strong-field physics and begins with a short overview in Sec. 3.1. Atoms in strong electromagnetic fields are considered in Sec. 3.2, followed by an elaborated analysis of strong-field processes such as strong-field ionization in Sec. 3.3 and high-order harmonic generation in Sec. 3.4. The generalized nondipole SFA is derived in Chap. 4 where Sec. 4.1 reviews the electron dynamics in spatially structured laser fields. The spatially dependent ionization and recombination matrix elements are derived in Sec. 4.2, while the final expression of the atomic dipole moment within the weakly relativistic regime is highlighted in Sec. 4.3. The atomic dipole moment of an elliptically polarized plane wave is explicitly discussed in Sec. 4.4, where Sec. 4.5, finally, motivates potential features of HHG with Bessel beams in the weakly relativistic regime. Chapter 5 discusses the analytically derived expression of the critical intensity, where the model and the derivation are presented in Sec. 5.1, while the results are mentioned in Sec. 5.2. Furthermore, a short outlook for future applications is given in Sec. 5.3. Finally, Sec. 6 summarizes and concludes the findings of this dissertation.

This dissertation is written in atomic units ($\hbar = e = m_e = 4\pi\epsilon_0 = 1$) unless stated otherwise.

CHAPTER 2.

DESCRIPTION OF STRUCTURED LIGHT FIELDS

“ It is our choices, Harry, that show what we truly are, far more than our abilities”

— Albus Dumbledore

2.1. Maxwell equations

An accurate mathematical description of light fields propagating in the vacuum is essential to model the interaction of intense laser fields with atoms. The Maxwell equations describes the dynamics of light within the context of electromagnetic waves. In the absence of free electric charges, the electric and magnetic fields denoted as $\mathbf{E}(\mathbf{r}, t)$ and $\mathbf{B}(\mathbf{r}, t)$, respectively are known solutions of the Maxwell equations [27]

$$\hat{\nabla}_{\mathbf{r}} \cdot \mathbf{E}(\mathbf{r}, t) = 0, \quad \hat{\nabla}_{\mathbf{r}} \times \mathbf{E}(\mathbf{r}, t) = -\hat{\partial}_t \mathbf{B}(\mathbf{r}, t), \quad (2.1a)$$

$$\hat{\nabla}_{\mathbf{r}} \cdot \mathbf{B}(\mathbf{r}, t) = 0, \quad \hat{\nabla}_{\mathbf{r}} \times \mathbf{B}(\mathbf{r}, t) = \frac{1}{c^2} \hat{\partial}_t \mathbf{E}(\mathbf{r}, t), \quad (2.1b)$$

with the speed of light in a vacuum c ¹. It is advantageous for further investigations to reformulate both fields by means of a scalar $\Phi(\mathbf{r}, t)$ and a vector $\mathbf{A}(\mathbf{r}, t)$ potential via

$$\mathbf{E}(\mathbf{r}, t) = -\hat{\nabla}_{\mathbf{r}} \Phi(\mathbf{r}, t) - \hat{\partial}_t \mathbf{A}(\mathbf{r}, t), \quad (2.2a)$$

$$\mathbf{B}(\mathbf{r}, t) = \hat{\nabla}_{\mathbf{r}} \times \mathbf{A}(\mathbf{r}, t). \quad (2.2b)$$

¹The partial derivative concerning the quantity x is defined by $\hat{\partial}_x \equiv \frac{\partial}{\partial x}$

However, the definition of physical fields $\mathbf{E}(\mathbf{r}, t)$ and $\mathbf{B}(\mathbf{r}, t)$ with respect to their associated potentials $\Phi(\mathbf{r}, t)$ and $\mathbf{A}(\mathbf{r}, t)$ is not unambiguous. By adding an arbitrary scalar field $\Lambda(\mathbf{r}, t)$, also known as the gauge field, one defines a new pair of potentials as

$$\tilde{\Phi}(\mathbf{r}, t) = \Phi(\mathbf{r}, t) - \hat{\partial}_t \Lambda(\mathbf{r}, t), \quad (2.3a)$$

$$\tilde{\mathbf{A}}(\mathbf{r}, t) = \mathbf{A}(\mathbf{r}, t) + \hat{\nabla}_r \Lambda(\mathbf{r}, t), \quad (2.3b)$$

which leave the physical fields invariant for any (smooth) function $\Lambda(\mathbf{r}, t)$. These types of transformation are known as *gauge transformations* and are of fundamental importance in practically all fields of physics. Imposing gauge conditions on the potentials $\Phi(\mathbf{r}, t)$ and $\mathbf{A}(\mathbf{r}, t)$ determines the specific potentials from the Maxwell equations. This dissertation focuses on the Coulomb gauge which is frequently applied in nonrelativistic electrodynamics [28] and reads as

$$\hat{\nabla}_r \cdot \mathbf{A}(\mathbf{r}, t) = 0, \quad \Phi(\mathbf{r}, t) = 0, \quad (2.4)$$

in which the scalar potential $\Phi(\mathbf{r}, t)$ vanishes as a consequence of the absence of free charges. Inserting Eq. (2.2) into the Maxwell equations (2.1) and simultaneously utilizing the Coulomb gauge (2.4) reduces the respective Maxwell equations to the wave equation

$$\hat{\nabla}_r^2 \mathbf{A}(\mathbf{r}, t) - \frac{1}{c^2} \hat{\partial}_t^2 \mathbf{A}(\mathbf{r}, t) = \mathbf{0}. \quad (2.5)$$

The superposition of an arbitrary number of monochromatic electromagnetic waves represents a set of solutions to this wave equation. Note that electromagnetic waves in the vacuum are unambiguously defined by their respective vector potential with no need for a scalar potential. However, for a single monochromatic light field, like a laser field, the respective vector potential is written as

$$\mathbf{A}(\mathbf{r}, t) = \text{Re} \left[\mathbf{A}(\mathbf{r}) e^{-i\omega t} \right], \quad (2.6)$$

with the frequency ω , while $\text{Re}[x]$ denotes the respective real part of an expression x . Inserting this definition of the vector potential into the wave equation (2.5) reduces it to the Helmholtz equation

$$\left(\hat{\mathbf{p}}^2 - k^2 \right) \mathbf{A}(\mathbf{r}) = \mathbf{0}, \quad (2.7)$$

DEFINITION 2.1: SPATIAL STRUCTURE LIGHT FIELDS

A light field is called *spatially structured* if one of the following equivalent statements is fulfilled:

- The laser field has a spatial structure $\mathbf{A}(\mathbf{r}) \neq \text{const.}$
- The magnetic field of the laser beam does not vanish $\mathbf{B} \neq 0$
- The linear photon momentum does not vanish $\mathbf{k} \neq 0$

If one of these statements is fulfilled, the remaining statements are fulfilled simultaneously, which results as a consequence of their equivalence.

with the wave number $k = |\mathbf{k}| = \omega/c$ and the linear momentum operator $\hat{\mathbf{p}} = -i\hat{\nabla}_{\mathbf{r}}$. The spatial dependence of the vector potential $\mathbf{A}(\mathbf{r})$ defines the *spatial structure* of the associated laser field. Important insight can be drawn from the general spatial structure of any laser field. Supposing no spatial structure exists $\mathbf{A}(\mathbf{r}) = \text{const.}$, results in a vanishing linear momentum $\hat{\mathbf{p}}\mathbf{A}(\mathbf{r}) = \mathbf{k}\mathbf{A}(\mathbf{r}) \Rightarrow \mathbf{k} = 0$ in Eq. (2.7), and consequently a vanishing magnetic field which is nonphysical. A general definition of spatially structured light fields is introduced in Def. 2.1. Generally, the dispersion relation $k = \omega/c$ forbids the existence of oscillating light fields with a constant spatial structure. Nevertheless, in many atom-light interactions, the contribution of the spatial structure is small and therefore omitted. This approximation scheme refers to as *dipole approximation* which is extensively discussed in Sec. 2.3. Under specific conditions, the error of the dipole approximation increases significantly. In this case, the spatial structure, namely the magnetic field in classical electrodynamics or the photon momentum in quantum mechanics, must be considered. However, Chap. 4 presents a new approach to high-order harmonic generation and discusses effects beyond the dipole regime.

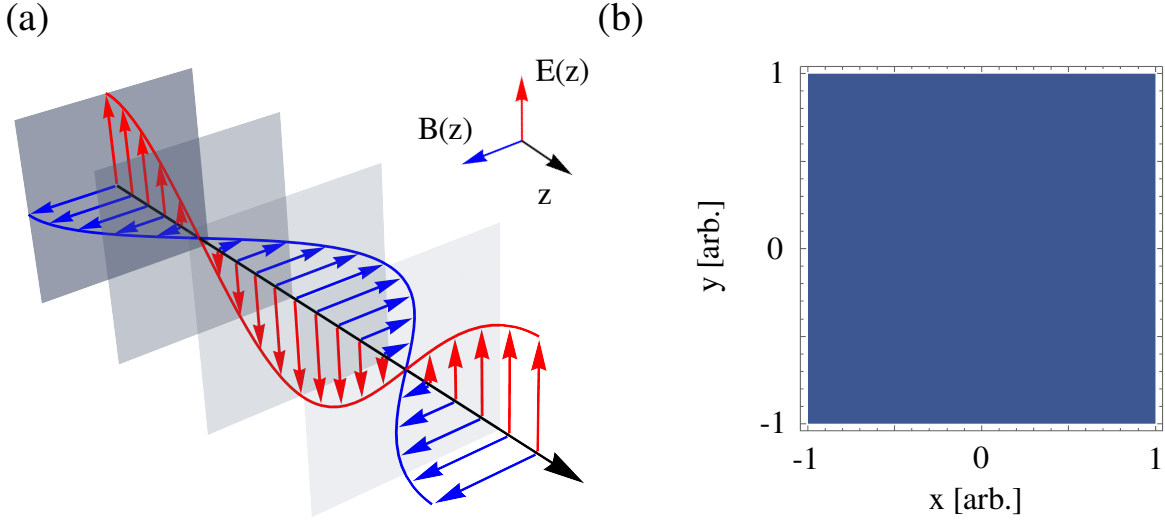


Figure 2.1.: Linearly polarized plane-wave beam (a) with the electric field (red) and the magnetic field (blue). Both fields are plotted as a function of the z coordinate for a fixed time $t = t_0$. The phase in the transverse plane is visualized in (b) for a fixed time $t = t_0$ and z -coordinate $z = z_0$. Here, the origin of the name *transverse plane wave* can clearly be seen since the phase in the transverse plane is constant or *plane*.

2.2. Plane wave solution of the Helmholtz equation

The spatially dependent vector potential of a transverse plane wave is an elementary solution of the Helmholtz equation (2.7)

$$\mathbf{A}(\mathbf{r}) = A_0 e^{i\mathbf{k}\cdot\mathbf{r}} \boldsymbol{\epsilon}, \quad (2.8)$$

with the field amplitude A_0 , the wave vector $\mathbf{k} = k\mathbf{e}_z$, and the polarization vector

$$\boldsymbol{\epsilon} = \frac{1}{\sqrt{1 + \varepsilon^2}} (\mathbf{e}_x + i\Lambda\varepsilon\mathbf{e}_y). \quad (2.9)$$

Here, ε denotes the ellipticity of the transverse plane wave, while Λ defines its helicity. Throughout this dissertation, the focus lies on transverse plane waves for which the short-term *plane waves* is used in the following. Time-dependent plane waves are characterized by their respective wavelength λ , field amplitude A_0 , ellipticity ε , and helicity Λ . Figure 2.1a illustrates the electric and magnetic field of a linearly polarized plane wave field, while Fig. 2.1b shows its respective phase for a fixed position $z = z_0$ on the optical axis. The name *plane waves* originates from the phase of the respective light field, which does not change throughout the transverse x - y plane (polarization plane). This

DEFINITION 2.2: MONOCHROMATIC PLANE WAVE

A general monochromatic plane wave is defined as

$$\mathbf{A}(\mathbf{r}, t) = \text{Re} \left[A_0 e^{i(\mathbf{r} \cdot \mathbf{k} - \omega t)} \boldsymbol{\epsilon} \right],$$

with the orthonormalized basis set $\{\mathbf{e}_1, \mathbf{e}_2, \mathbf{e}_k\}$ which obeys

$$\boldsymbol{\epsilon} = \frac{1}{\sqrt{1 + \varepsilon^2}} (\mathbf{e}_1 + i\Lambda\varepsilon\mathbf{e}_2) \quad \text{and} \quad \boldsymbol{\epsilon} \cdot \mathbf{k} = 0.$$

is additionally highlighted in Fig. 2.1a by planes of constant phase (gray) and decreasing opacity along the optical axis (z). The field intensity is also a characteristic property of plane waves and is defined by the cycle-averaged Poynting vector $\mathbf{P} = \frac{1}{\mu_0} \mathbf{E}(\mathbf{r}, t) \times \mathbf{B}(\mathbf{r}, t)$ as [29]

$$\begin{aligned} I(\mathbf{r}, t) &= \frac{1}{T} \left| \int_t^{t+T} d\tau \mathbf{P}(\mathbf{r}, t) \right|, \\ &= \frac{A_0^2 \omega^3 c}{8\pi^2 (1 + \varepsilon^2)} \int_t^{t+T} d\tau \left(\sin^2(kz - \omega t) + \varepsilon^2 \cos^2(kz - \omega t) \right) = \frac{A_0^2 \omega^2 c}{8\pi}. \end{aligned} \quad (2.10)$$

In the Coulomb gauge, the dependence of the cycle-averaged intensity is limited to the electric field amplitude $E_0 = -A_0\omega$ if one utilizes the respective electric and magnetic field (2.2) in the Coulomb gauge (2.4).

For specific cases, e.g. the superposition of plane-wave beams [30,31], it is advantageous to generalize the definition of the vector potential by considering a general orthonormalized basis set $\{\mathbf{e}_1, \mathbf{e}_2, \mathbf{e}_k\}$. The respective definition for a monochromatic plane wave can be found in Def. 2.2.

The full vector potential with respect to Eq. (2.8) then reads

$$\mathbf{A}(\mathbf{r}, t) = \frac{A_0}{\sqrt{1 + \varepsilon^2}} \left(\cos(\mathbf{k} \cdot \mathbf{r} - \omega t) \mathbf{e}_1 - \varepsilon\Lambda \sin(\mathbf{k} \cdot \mathbf{r} - \omega t) \mathbf{e}_2 \right). \quad (2.11)$$

For now, the essential case of circular polarization $\varepsilon = 1$ is investigated to discuss the physical interpretation of the helicity Λ in more detail. To do so, one follows the ideas of

Matula et al. [32] and defines the propagation direction of the plane-wave beam via

$$\mathbf{e}_{\mathbf{k}} = \begin{pmatrix} \sin \vartheta_{\mathbf{k}} \cos \varphi_{\mathbf{k}} \\ \sin \vartheta_{\mathbf{k}} \sin \varphi_{\mathbf{k}} \\ \cos \vartheta_{\mathbf{k}} \end{pmatrix}, \quad (2.12)$$

with the polar $\varphi_{\mathbf{k}}$ and azimuthal angle $\vartheta_{\mathbf{k}}$ of the wave vector \mathbf{k} , respectively. Since the polarization vector is orthogonal to the wave vector, the Coulomb gauge condition $\boldsymbol{\epsilon} \cdot \mathbf{k} = 0$ still holds and defines the polarization vector as

$$\boldsymbol{\epsilon}_{\mathbf{k}\Lambda} = -\frac{\Lambda}{\sqrt{2}} \begin{pmatrix} \cos \vartheta_{\mathbf{k}} \cos \varphi_{\mathbf{k}} - i\Lambda \sin \varphi_{\mathbf{k}} \\ \cos \vartheta_{\mathbf{k}} \sin \varphi_{\mathbf{k}} + i\Lambda \cos \varphi_{\mathbf{k}} \\ -\sin \vartheta_{\mathbf{k}} \end{pmatrix}. \quad (2.13)$$

It is often convenient to represent the polarization vector within the basis of spin-momentum operators

$$\boldsymbol{\epsilon}_{\mathbf{k}\Lambda} = \sum_{m_s=0,\pm 1} c_{m_s} e^{-im_s \varphi_{\mathbf{k}}} \boldsymbol{\eta}_{m_s}, \quad (2.14)$$

$$\hat{S}_z \boldsymbol{\eta}_{m_s} = m_s \boldsymbol{\eta}_{m_s}, \quad \boldsymbol{\eta}_{\pm 1} = \frac{\mp 1}{\sqrt{2}} \begin{pmatrix} 1 \\ \pm i \\ 0 \end{pmatrix}, \quad \boldsymbol{\eta}_0 = \begin{pmatrix} 0 \\ 0 \\ 1 \end{pmatrix}, \quad (2.15)$$

with the expansion coefficients $c_0 = \frac{\Lambda}{\sqrt{2}} \sin \vartheta_{\mathbf{k}}$ and $c_{\pm 1} = \frac{1}{2}(1 \pm \Lambda \cos \vartheta_{\mathbf{k}})$. Setting the polar and azimuthal angle to zero determines the z-axis as the optical axis. The helicity is, within this context, understood as the photon's spin projection onto its own momentum \mathbf{k} [32]. Laser fields of ellipticity $\varepsilon \neq 1$ are described as a superposition of circularly polarized plane waves such that the photon-spin interpretation is still valid for an extension to elliptically polarized plane waves.

Overall, monochromatic plane-wave beams are characterized by their respective wavelength $\lambda = 2\pi c/\omega$, helicity $\Lambda = \pm 1$, ellipticity $0 \leq \varepsilon \leq 1$, and intensity I .

2.3. Laser fields in the dipole approximation

2.3.1. Plane wave beams

So far, plane waves as solutions to the Maxwell equations in vacuum have been discussed. To simplify the respective equations, the Coulomb gauge (2.4) has been chosen which condenses the respective Maxwell equations to Eq. (2.5). Furthermore, it was demonstrated that the remaining Maxwell equation for a monochromatic laser field is then defined by the Helmholtz equation (2.7). However, even simpler fields may solve the Helmholtz equation, in which the radial dependency implicitly vanishes. The theoretical analysis of several strong-field processes such as above-threshold ionization (ATI) and HHG is extensively simplified by neglecting the spatial structure of the incident laser field $\mathbf{A}(\mathbf{r}_0 + \mathbf{r}, t) \rightarrow \mathbf{A}(\mathbf{r}_0, t) \equiv \mathbf{A}(t)$. Here, the respective atom is located at the parametric position \mathbf{r}_0 . Strong-field processes, however, do not significantly depend on the spatial structure of the laser field. The contribution of the spatial structure essentially depends on the wave vector, which is proportional to the speed of light $\mathbf{k} \propto 1/c$ and consequently affects strong-field processes only marginally. The respective contribution of the spatial structure, therefore, consists of a small correction and is neglected in the first instance. The resulting vector potential of a continuous linearly polarized *plane wave beam* therefore reads

$$\mathbf{A}(t) = A_0 \sin(\omega t) \mathbf{e}_1, \quad (2.16)$$

with the spatial dependent vector potential $\mathbf{A}(\mathbf{r}) = A_0 \mathbf{e}_1$.

2.3.2. Plane wave pulses

In the experiment, light-matter interactions are often realized by laser pulses instead of continuous laser beams. The plane-wave pulse has, in contrast to a plane-wave beam, a modulating function that defines the pulse duration and the concrete temporal structure. This function is known as the *envelope* of the pulse. The electric field of a linearly polarized plane wave pulse reads [33]

$$\mathbf{E}(t) = E_0 f(t) \cos(\omega t + \varphi_0) \mathbf{e}_1, \quad (2.17)$$

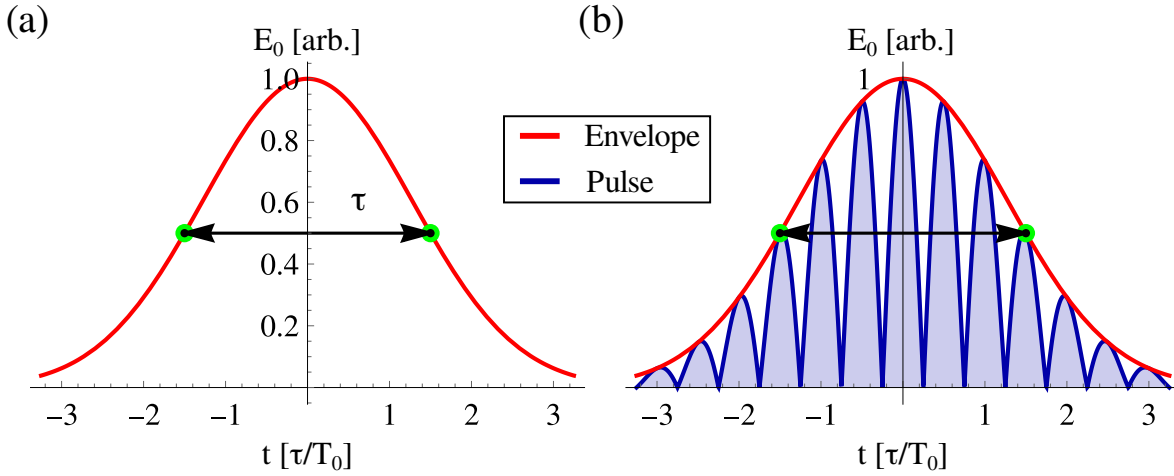


Figure 2.2.: Gaussian plane-wave pulses: (a) The envelope (red) that encloses the pulse is characterized by its finite pulse width (FWHM) τ , which is indicated by the arrow and the associated dots (green-black). (b) Modulus of the electric field for the complete laser pulse (blue) and its envelope, mentioned in (a).

with envelope $f(t)$, electric field amplitude E_0 , and constant phase φ_0 . A commonly used pulse shape is the Gaussian pulse which is defined via

$$f(t) = e^{-4\ln(2)(t/\tau)^2}. \quad (2.18)$$

The pulse duration τ is defined in terms of the so-called full width at half maximum (FWHM), which indicates the time span between t_1 and t_2 . Here, $t_{1/2}$ denotes the respective instance in time that obeys $f(t_{1/2}) = \frac{1}{2}$. The envelope (red) is visualized in Fig. 2.2a, with the pulse duration τ (arrow) while Fig. 2.2b illustrates the modulus of the electric field for the complete laser pulse.

However, the actual structure of a Gaussian pulse envelope is often too complicated for analytical purposes. In strong-field physics, it is often convenient to approximate the envelope as a sine square pulse defined by

$$f(t) = \begin{cases} \sin^2\left(\frac{\omega t}{2n_p}\right) & 0 \leq t \leq \tau \\ 0 & \text{otherwise} \end{cases}, \quad (2.19)$$

with the pulse duration $\tau \equiv n_p T_0$. The Gaussian envelope is reasonably well approximated by the sine-square envelope, especially for times close to the peak of the pulse. The probability amplitude of strong-field processes generally decreases exponentially with the respective instantaneous field strength. Therefore, even larger deviations of the sine

DEFINITION 2.3: GENERALIZED VECTOR POTENTIAL

The generalized vector potential is a continuous superposition of transverse plane waves

$$\mathbf{A}(\mathbf{r}, t) = \int d^3\mathbf{k} \mathbf{A}(\mathbf{k}, t) = \int d^3\mathbf{k} \operatorname{Re} [\mathbf{a}_{\mathbf{k}} e^{iu_{\mathbf{k}}}],$$

with the transverse plane wave mode $\mathbf{A}(\mathbf{k}, t)$, the complex amplitude $\mathbf{a}_{\mathbf{k}}$, the plane wave phase $u_{\mathbf{k}} = \mathbf{r} \cdot \mathbf{k} - \omega_{\mathbf{k}}t$, and the wave vector \mathbf{k} . The complex amplitude $\mathbf{a}_{\mathbf{k}}$ obeys the orthogonality relation of transverse plane waves as $\mathbf{k} \perp \mathbf{a}_{\mathbf{k}}$.

square approximation are insignificant apart from the peak of the pulse. A benefit of a sine square envelope is its simple representation as a superposition of three monochromatic plane wave beams in the respective time interval [34] which denotes a great advance in contrast to the Gaussian envelope. In the case of sufficiently long laser pulses ($n_p \rightarrow \infty$), a general laser pulse may be approximated as a single laser beam with a constant envelope $f(t) \rightarrow 1$.

To summarize, the sine square approximation of the Gaussian envelope denotes an accurate approximation for strong-field processes like ATI or HHG while its representation remains reasonably simple. Another, more sophisticated approximation of the Gaussian envelope is discussed within the context of phase-matched HHG in Chap. 5.

2.4. Spatially structured light fields

In the previous section, the properties of plane-wave laser beams and pulses within the dipole approximation have been discussed. However, beyond these fairly simple solutions of the Maxwell equations, there exist more elaborated approaches. In modern atomic and strong-field physics, a particularly interesting class of light is called *twisted light*. Twisted light beams and pulses have been shown to induce many interesting features which are related to their specific spatial (twisted) structure. The most prominent feature is the orbital angular momentum that is uniquely associated with twisted light [35, 36] and is, for example, realized in Laguerre-Gaussian or Bessel beams. These beams, as well as many more, can be represented as the continuous superposition of plane waves [32].

The Fourier coefficient or namely the complex amplitude $\mathbf{a}_{\mathbf{k}}$ characterizes the spatial structure as well as the polarization of the respective laser field. Individual plane waves

implicitly satisfy the Coulomb gauge with $\mathbf{k} \cdot \mathbf{a}_{\mathbf{k}} = 0$. This can be seen by interchanging the order of the partial derivatives in Eq. (2.4) with the integral over the respective wave vector in Def. (2.3). Therefore, not only do the separate plane waves need to obey the Coulomb gauge but the vector potential in general. The vector potential of an elliptically polarized plane wave (2.11) is obtained with the respective complex amplitude as

$$\mathbf{a}_{\mathbf{k}} = \frac{A_0}{\sqrt{1 + \epsilon^2}} (\mathbf{e}_1 + i\Lambda\epsilon\mathbf{e}_2) \delta(\mathbf{k} - \mathbf{k}_0). \quad (2.20)$$

Twisted light: Bessel beam

Plane waves as introduced in the previous section represent the most straightforward class of solutions to the Maxwell equations. A more elaborate class of solutions is associated with *twisted light* beams. Laguerre-Gaussian or Bessel beams are commonly used examples of these twisted light beams and represent particular families of solutions to the Helmholtz equation (2.7). Twisted light beams possess helical phase fronts that rotate or *twist*, around their propagation axis, illustrated in Fig. 2.3a.

This dissertation focuses on monochromatic Bessel beams that are eigenstates of the total angular momentum projection

$$\hat{J}_z = \hat{L}_z + \hat{S}_z, \quad \Rightarrow \quad \hat{J}_z \mathbf{A}(\mathbf{r}) = m_\gamma \mathbf{A}(\mathbf{r}), \quad (2.21)$$

with the orbital angular momentum operator $\hat{L}_z = -i\hat{\partial}_\varphi$. In addition, the Bessel beam is assumed to have a well-defined longitudinal momentum via

$$\hat{p}_z^2 \mathbf{A}(\mathbf{r}) = k_z^2 \mathbf{A}(\mathbf{r}). \quad (2.22)$$

Therefore, the transverse momentum is well defined by $k_\perp \equiv |\mathbf{k}_\perp| = \sqrt{k^2 - k_z^2}$, with $k = \omega/c$, as a result of Eqs. (2.7) and (2.22).

An explicit expression of the spatially dependent vector potential $\mathbf{A}(\mathbf{r})$ needs to be constructed such that it fulfills the Helmholtz equation (2.7), the eigenvalue equations (2.21) and (2.22), and the Coulomb gauge (2.4), simultaneously. These conditions are fulfilled for a superposition of circularly polarized plane waves [32, 37] by

$$\mathbf{A}(\mathbf{r}) = \frac{A_0}{(2\pi)^2} \int d^2\mathbf{k}_\perp \mathbf{a}_{\kappa m_\gamma}(\mathbf{k}_\perp) \boldsymbol{\epsilon}_{\mathbf{k}\Lambda} e^{i\mathbf{k}\cdot\mathbf{r}}, \quad (2.23)$$

with the polarization vector $\boldsymbol{\epsilon}_{\mathbf{k}\Lambda}$ defined in Eq. (2.15) and the helicity $\Lambda = \pm 1$. Here, the plane waves are weighted by a transverse-wave-vector-dependent amplitude

$$\mathbf{a}_{\kappa m_\gamma}(\mathbf{k}_\perp) = (-i)^{m_\gamma} \sqrt{\frac{2\pi}{\kappa}} e^{im_\gamma \varphi_{\mathbf{k}}} \delta(k_\perp - \kappa). \quad (2.24)$$

The Dirac delta distribution specifies the orientation of the corresponding plane waves that form the Bessel beam. These plane waves have a well-defined transverse momentum κ and lie on a cone in momentum space with opening angle $\theta_{\mathbf{k}} = \arctan(\kappa/k_z)$; see Fig. 2.3b. After performing the integration of Eq. (2.23) in momentum space, the spatial-dependent vector potential of the Bessel beam reads

$$\mathbf{A}(\mathbf{r}) = \sum_{m_s=-1}^1 A_{m_s}(\mathbf{r}) \boldsymbol{\eta}_{m_s}, \quad (2.25a)$$

$$A_{m_s}(\mathbf{r}) = (-i)^{m_s} \sqrt{\frac{\kappa}{2\pi}} c_{m_s} J_{m_\gamma - m_s}(\kappa r) e^{i(m_\gamma - m_s)\varphi_{\mathbf{r}}} e^{ik_z z}, \quad (2.25b)$$

with the Bessel function of the first kind $J_n(x)$, the azimuthal angle in real space $\varphi_{\mathbf{r}}$, and the coefficients

$$c_0 = \frac{\Lambda}{\sqrt{2}} \sin(\theta_{\mathbf{k}}), \quad c_{\pm 1} = \frac{1}{2} \left(1 \pm \Lambda \cos(\theta_{\mathbf{k}}) \right). \quad (2.26)$$

Paraxial Bessel beams are often of particular interest in strong-field physics. In the paraxial regime, the opening angle $\theta_{\mathbf{k}}$ is small such that transverse momentum equivalently fulfills $\kappa \ll k_z$. The dominant contribution in the summation of Eq. (2.25a) is then associated with $m_s = \Lambda$ and condenses to the respective spatial-dependent vector potential [32, 37, 38]

$$\mathbf{A}(\mathbf{r}) \approx (-i)^\Lambda \sqrt{\frac{\kappa}{2\pi}} c_\Lambda J_{m_\gamma - \Lambda}(\kappa r) e^{i(m_\gamma - \Lambda)\varphi_{\mathbf{r}}} e^{ik_z z} \boldsymbol{\eta}_\Lambda. \quad (2.27)$$

The circularly polarized paraxial Bessel beam is simultaneously the eigenfunction of the spin and orbital angular momentum operators. The spin and orbital angular momentum are therefore separably measurable observables and defined via

$$\hat{S}_z \mathbf{A}(\mathbf{r}) = \Lambda \mathbf{A}(\mathbf{r}), \quad \hat{L}_z \mathbf{A}(\mathbf{r}) = m_\ell \mathbf{A}(\mathbf{r}), \quad (2.28)$$

with orbital angular momentum $m_\ell = m_\gamma - \Lambda$. Here, the helical phase fronts obey $m_\ell \varphi_{\mathbf{r}} + k_z z \equiv 0$ in accordance with Eq. (2.27) and can be seen in Fig. 2.3a while the respective intensity profile is illustrated in Fig. 2.3c.

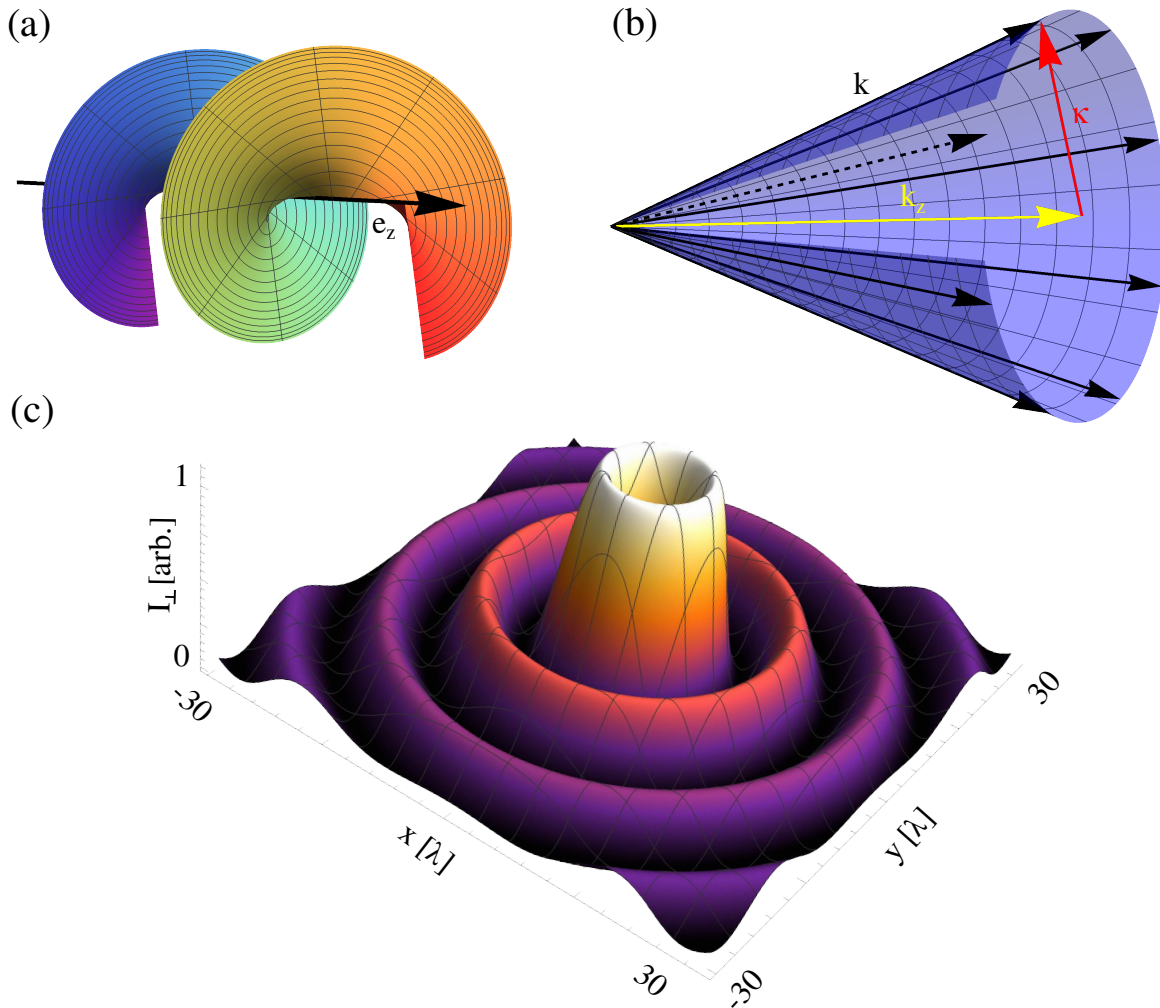


Figure 2.3.: (a) Helical phase front of a paraxial Bessel beam with orbital angular momentum $m_\ell = 1$ and opening angle $\theta_{\mathbf{k}} = 3^\circ$ that winds around the optical (z) axis. (b) Bessel beams are built as a superposition of transverse plane waves with wave vectors \mathbf{k} (black). These consist of a longitudinal k_z (yellow) and a transverse-wave-vector component κ (red). The superposition of the transverse plane waves is visualized by the sliced cone with opening angle $\theta_{\mathbf{k}} = 20^\circ$. (c) The transverse intensity of the paraxial Bessel beam as defined in Ref. [32] for the respective beam parameters in (a).

CHAPTER 3.

THEORETICAL APPROACH TO STRONG-FIELD PROCESSES

“Not only is the Universe stranger than we think, it is stranger than we can think.”

— Werner Heisenberg

3.1. Overview

This chapter provides an introduction to the theory of strong-field ionization and high-order harmonic generation (HHG). A variety of targets may generate High-order harmonic (HH) radiation, such as atoms [17,39], ions [40], molecules [41], solids [42], and crystals [43]. This dissertation particularly focuses on HHG from atomic and ionic gas targets, since the respective microscopic theories differ significantly. Moreover, HHG from atomic and ionic targets has been shown to be most efficient in the generation of ultra-short coherent laser pulses from tabletop-sized devices and is utilized in many domains of science [44–46].

Strong-field processes are light-atom interactions in which an intense light field irradiates an atomic gas target; see Fig. 3.1a, and significantly affects the target system at a microscopic scale. The intense *classical light field* interacts with *quantized atomic targets* and induces transitions of a bound electron into the continuum, also known as strong-field ionization. The essential difference to processes in other branches of atomic physics originates from the high intensity of the incident light field, which leads to the distortion of the atomic binding potential. The contribution of this distortion is of the same order of magnitude as or slightly lower than the contribution of the atomic binding

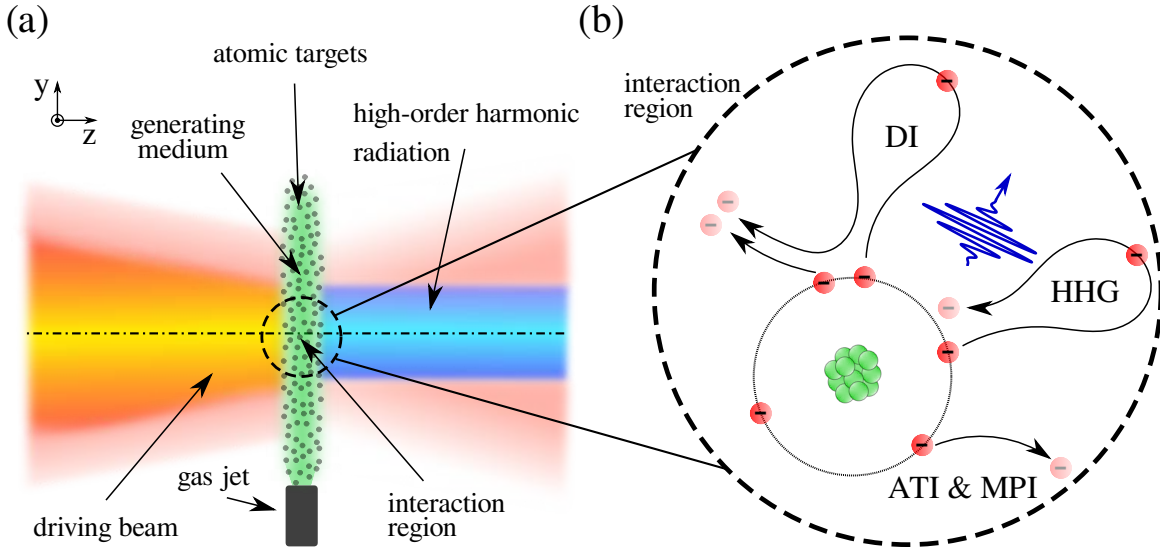


Figure 3.1.: (a) Geometry of a strong-field setup and (b) the associated strong-field processes, namely ionization (ATI & MPI), sequential and nonsequential double ionization (DI), and high-order harmonic generation (HHG).

potential. The perturbative descriptions of the respective processes do therefore not fit. Strong-field processes are, consequently, often referred to be *nonlinear* or *nonperturbative* in nature.

The ionization of a valence shell electron is an elementary process in strong-field physics. Starting from this elementary ionization subsequently leads to more complex processes such as HHG or double ionization. Here, Figure 3.1b schematically illustrates some of these processes. The intense light fields are frequently utilized as quasi-monochromatic plane wave pulses generated by high-intensity lasers like the titanium-sapphire laser [47,48] or the yttrium-aluminum-garnet (YAG) laser [49]. The induced dynamics of these lasers in strong-field ionization and other processes essentially depend on the physical parameters of the atomic target and the laser field. For the sake of simplicity, the discussion in this chapter is restricted to plane-wave laser fields within the dipole approximation as defined in Sec. 2.3.

3.2. Atoms in intense electromagnetic fields

Keldysh's work in the middle of the 1960 years [16] offers a parameter to characterize different strong-field regimes. This so-called *Keldysh parameter* γ is dimensionless and

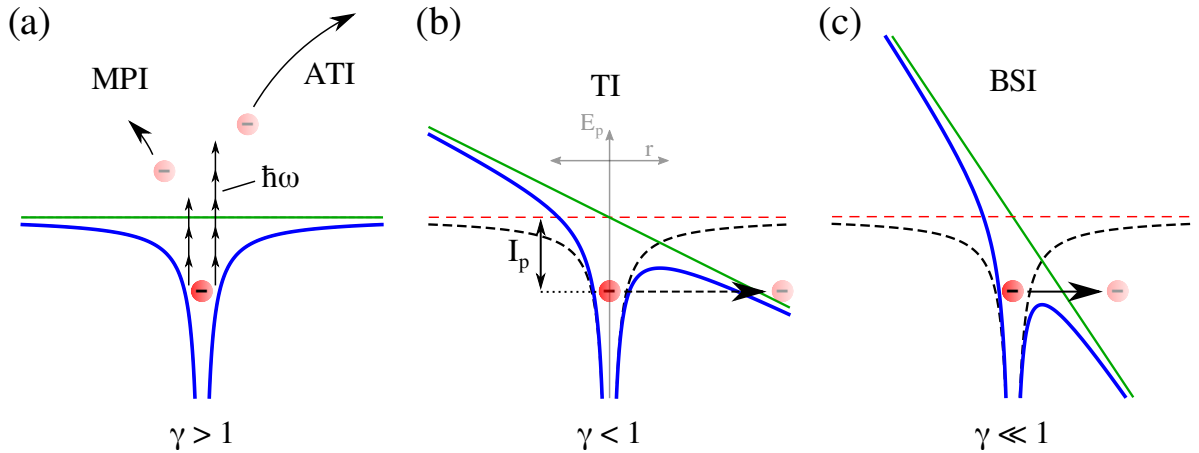


Figure 3.2.: Strong-field ionization processes. The coordinate system represents the spatial distance r (x-axis) and the potential energy E_p (y-axis): (a) multiphoton ionization (MPI) and above-threshold ionization (ATI), (b) tunnel ionization (TI), and (c) barrier suppression ionization (BSI).

depends on the atomic target and the laser beam via

$$\gamma = \sqrt{\frac{I_p}{2U_p}} = \frac{\omega}{E_0} \sqrt{2I_p}. \quad (3.1)$$

Here, I_p denotes the ionization potential of the respective atom, ω the frequency of the laser beam, and E_0 is the strength of the electric field. Furthermore, the cycle-averaged kinetic energy of an electron propagating in a linearly polarized plane-wave laser beam is introduced as the ponderomotive energy with

$$U_p = \frac{E_0^2}{4\omega^2}. \quad (3.2)$$

The Keldysh parameter γ belongs to the positive real numbers and divides strong-field ionization into three regimes, where each regime is associated with a specific ionization process [50]. First, *multiphoton ionization* (MPI) and *high-order above-threshold ionization* (ATI) dominate the regime for Keldysh parameters $\gamma > 1$. In both processes, the bound electron ionizes by absorption of at least q_{min} photons with a single photon energy $E_{ph} = \hbar\omega$, such that the combined photon energy $E_q = qE_{ph}$ is equal to or greater than the ionization potential I_p , shown in Fig. 3.2a. One particularly observes multiphoton ionization if the energy of the absorbed photons $E_{q_{min}}$ approaches the ionization potential. If the number of absorbed photons increases, $q > q_{min}$, the ionization process is defined as above-threshold ionization. For Keldysh parameters $\gamma < 1$, *tunnel ionization* (TI) dominates, in which the electric field suppresses the binding

Table 3.1.: Ionization processes: Operating conditions and Keldysh parameters of the respective ionization processes in terms of single-photon energy E_{ph} , atomic ionization potential I_p , and ponderomotive energy U_p .

Ionization regime	Operating condition	Keldysh parameter
Single-photon ionization	$E_{ph} > I_p \gg U_p$	$\gamma \gg 1$
Multiphoton ionization	$I_p > E_{ph} \gg U_p$	$\gamma \gg 1$
Above-threshold ionization	$I_p > U_p > E_{ph}$	$\gamma > 1$
Tunnel ionization	$U_p > I_p > E_{ph}$	$\gamma < 1$
Barrier-suppression ionization	$U_p \gg I_p > E_{ph}$ (restricted to increasing E_0)	$\gamma \ll 1$

potential of the atom such that the bound electron may tunnel ionize into the continuum; see Fig. 3.2b. With an increasing electric field strength the Keldysh parameter $\gamma \ll 1$ decreases further. The binding potential is consequently strongly suppressed by the electric field so that the bound state of the electron is no longer associated with the energetic minimum. This results in the so-called over-the-barrier ionization or *barrier-suppression ionization* (BSI), illustrated in Fig. 3.2c. Note that there exists a crucial difference in the ionization processes for Keldysh parameters larger than or smaller than one. On the one side ($\gamma > 1$) electrons directly absorb a fixed number of photons, while on the other side ($\gamma < 1$ and $\gamma \ll 1$) the binding potential is suppressed by the incident laser field. This suppression enables the electrons to ionize without directly interacting with the laser field. However, Tab. 3.1 lists the dominant ionization processes and their associated operating conditions.

High-order harmonic generation, on the other hand, is a higher-order process that is understood within the vivid model of Corkum [51]. Corkum divides the HH process into three individual processes. Therefore, the model is also known as *three-step model* of HHG, illustrated in Fig. 3.3. Initially, the bound electron tunnel ionizes into the continuum; see Fig. 3.3a. Subsequently, the electron appears in the continuum, dressed by the laser field as illustrated in Fig. 3.3b. The electron enters the continuum roughly ten atomic units apart from the nucleus, which validates the neglect of a comparable weak contribution from the atomic binding potential. Corkum refers to the second step as the propagation of the electron in the dressed continuum. For linearly polarized light, the electron returns to its parent ion after a half optical period and eventually recombines radiatively, which denotes the third step in Fig. 3.3c. Besides the recombination, the electron may similarly scatter at the electron cloud of the parent ion. The scattering

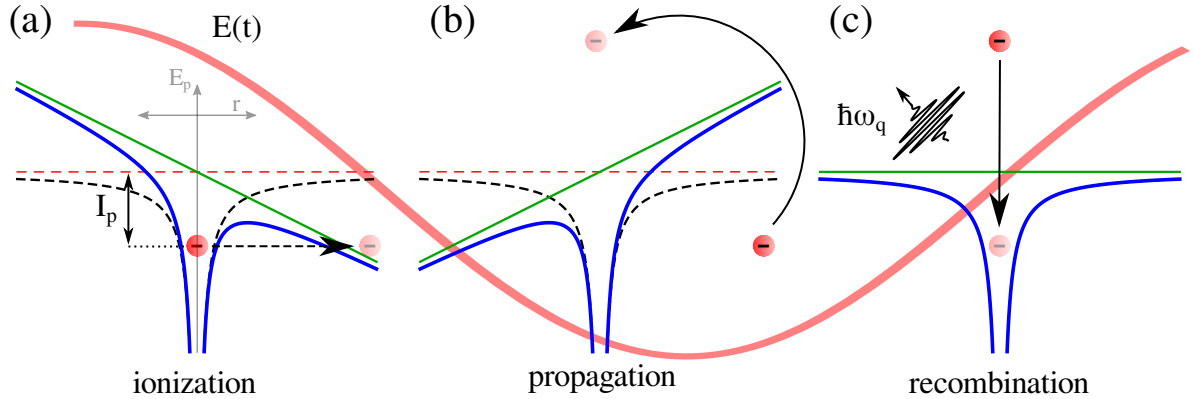


Figure 3.3.: Three-step model of HHG illustrated by the electric field (red-solid line), electron (red circle), atomic binding potential (black-dashed line), laser potential (green-solid line), combined laser-atom potential (blue-solid line), and the vacuum potential (red-dashed line). The coordinate system represents the spatial distance r (x-axis) and the potential energy E_p (y-axis): (a) tunnel ionization of the electron at the peak of the electric field, (b) propagation within the continuum, (c) recombination of the electron with simultaneous emission of a high-order harmonic photon.

potentially leads to the so-called nonsequential double ionization [18] as well as high-order above-threshold ionization, by Paulus et al. Ref. [52]; see Fig. 3.1b. However, these processes are not investigated in this dissertation and are therefore omitted.

3.3. Multiphoton and tunnel ionization

The macroscopic ionization of gas targets significantly influences the generation of high-order harmonic radiation, which essentially highlights the importance of strong-field ionization within the context of HHG. HHG predominantly operates within the multiphoton, above-threshold, and tunnel ionization regimes. For the sake of simplicity, multiphoton and above-threshold ionization will, together, be referred to as multiphoton ionization without loss of generality. Strong-field ionization for arbitrary Keldysh parameters and hydrogen-like atoms is well described by the Yudin-Ivanov (YI) theory [53], apart from solving the time-dependent Schrödinger equation numerically [54]. It is advantageous to limit the investigations in this dissertation to approximations of the YI theory that incorporate the respective ionization processes to simplify the computation. The approximations of the YI theory are known as the ADK theory [55], which describes tunnel ionization within the regime of small Keldysh parameters $\gamma \ll 1$ and the earlier developed PPT theory [56], that incorporates the tunnel- and multiphoton ionization

regime. The PPT theory describes strong field ionization sufficiently well for Keldysh parameters of $\gamma \sim 1$ [57]. However, the PPT theory is accurate even for $\gamma \approx 3$ to 4 as long as the photon energy is small compared to the ionization potential with $E_{ph} \ll I_p$ [53], which holds for the vast majority of HHG configurations.

3.3.1. PPT theory

The PPT theory describes ionization into the continuum from a bound state of a three-dimensional hydrogen-like atom (or ion). The respective ionization rates are derived for an arbitrary initial state of OAM ℓ and magnetic quantum number m . These ionization rates are utilized in Chap. 5, which investigates phase-matched HHG.

In recent years, interest in shorter laser wavelengths has increased throughout the HHG community [58–61]. For these short wavelengths, the Keldysh parameter increases $\gamma \gtrsim 1$ so that strong-field ionization by wavelengths shorter than $\lambda \leq 800$ nm is not sufficiently well described by the ADK theory. Therefore, the more sophisticated PPT theory is utilized, which additionally incorporates multiphoton ionization and matches the experimental observation within the respective parameter region; see Tab. 3.1.

The hydrogen-like atomic target is characterized by the quantum numbers n, ℓ, m and its respective *effective quantum numbers* $n^* \equiv Z/\sqrt{2I_p}$, $\ell^* \equiv n^* - 1$ with the charge of the remaining ion Z and the ionization potential I_p . Furthermore, two atom-specific parameters are defined as

$$|C_{n^*, \ell^*}| = \frac{2^{2n^*}}{n^* \Gamma(n^* + \ell^* + 1) \Gamma(n^* - \ell^*)}, \quad G_{lm} = \frac{(2\ell + 1)(l + |m|)!}{2^{|m|} |m|! (l - |m|)!}, \quad (3.3)$$

with the gamma function $\Gamma(z)$. The coefficients $|C_{n^*, \ell^*}|$ and G_{lm} are normalization constants associated to the radial and azimuthal parts of the hydrogen-like wave function, respectively. The PPT ionization rate of an electron in the magnetic sub-state m then reads [33, 56]

$$w_m^{PPT}(t) = |C_{n^*, \ell^*}|^2 G_{lm} I_p \left(\frac{2(2I_p)^{3/2}}{E(t)} \right)^{2n^* - |m| - 1} e^{-\frac{2(2I_p)^{3/2}}{3E(t)} G(\gamma)} \times \frac{4}{|m|! \sqrt{3\pi}} \frac{\gamma^2}{1 + \gamma^2} (1 + \gamma^2)^{(|m|+1)/2} \sum_{q \geq q_{thr}}^{\infty} A_q(\omega, \gamma), \quad (3.4)$$

with the Keldysh parameter γ defined in Eq. (3.1) and the electric field of the incident laser as $E(t)$. Note that the dominant contribution to the ionization rate is associated with the exponential term, while minor contributions are related to the long-range interaction term by $\left(\frac{2(2I_p)^{3/2}}{E(t)}\right)^{2n^*-|m|-1}$. The functions $A_q(\omega, \gamma)$, $G(\gamma)$ and their respective constituents are listed in the following:

$$A_q(\omega, \gamma) = e^{-\alpha(q-v)} D_m \left(\sqrt{\beta(q-v)} \right), \quad (3.5a)$$

$$G(\gamma) = \frac{3}{2\gamma} \left[\left(1 + \frac{1}{2\gamma^2} \right) \sinh^{-1}(\gamma) - \frac{\sqrt{1+\gamma^2}}{2\gamma} \right], \quad (3.5b)$$

$$\alpha(\gamma) = 2 \left(\sinh^{-1}(\gamma) - \frac{\gamma}{\sqrt{1+\gamma^2}} \right), \quad (3.5c)$$

$$\beta(\gamma) = \frac{2\gamma}{\sqrt{1+\gamma^2}}, \quad (3.5d)$$

$$v = \frac{I_p + U_p}{\omega}, \quad (3.5e)$$

$$D_m(x) = \frac{x^{2|m|+1}}{2} \int_0^1 dt \frac{e^{-x^2 t |m|}}{\sqrt{1-t}} = e^{-x^2} \int_0^x dy e^{y^2} (x^2 - y^2)^{|m|}. \quad (3.5f)$$

Note, the function $D_m(x)$ is closely related to the Dawson function $Dawson(x) = e^{-x^2} \int_0^x dy e^{y^2}$ [62]. Finally, the average ionization rate from all $2\ell + 1$ sub-states reads as

$$w^{PPT}(t) = \frac{1}{2\ell + 1} \sum_{m=-\ell}^{\ell} w_m^{PPT}(t). \quad (3.6)$$

3.3.2. ADK theory

The ADK ionization rate approximates the respective PPT rate reasonably well within the tunnel ionization regime $\gamma < 1$; see Tab. 3.1. In the limiting case of $\gamma \ll 1$, the second line of Eq. (3.4) and $G(\gamma)$ approach unity [56] such that the ADK ionization rate reads [33]

$$w_m^{ADK}(t) = |C_{n^*\ell^*}|^2 G_{\ell m} I_p \left(\frac{2(2I_p)^{3/2}}{E(t)} \right)^{2n^*-|m|-1} e^{-\frac{2(2I_p)^{3/2}}{3E(t)}}. \quad (3.7)$$

To have a convenient notation for further investigations the following parameters are defined

$$\kappa_m = 3^{g_m+1} \frac{|C_{n^*\ell^*}|^2 G_{\ell m} I_p}{2\ell + 1}, \quad (3.8a)$$

$$g_m = 2n^* - |m| - 2, \quad (3.8b)$$

$$F_0 = \frac{2}{3} (2I_p)^{3/2}, \quad (3.8c)$$

such that the ADK ionization rate reads

$$w^{ADK}(t) = \sum_{m=-\ell}^{\ell} \kappa_m \left(\frac{F_0}{E(t)} \right)^{g_m+1} e^{-\frac{F_0}{E(t)}}. \quad (3.9)$$

Even though both ionization models are rough approximations, they are widely used e.g. in theoretical models considering ground state depletion [63] or phase-matching simulations [64,65]. They consequently represent an important and valuable tool for the strong-field community.

3.4. High-order harmonic generation

Since the early days of HHG, the HH process was qualitatively understood utilizing the three-step model proposed by Corkum [51]. The three-step model approximates the wave function of the initial and final states as hydrogen-like, while the electron propagation in the continuum remains classical. More sophisticated theoretical approaches like the Lewenstein model, are available today. An important component of the Lewenstein model is the *strong-field approximation* (SFA) which is investigated beyond the dipole approximation in Chap. 4.

The Lewenstein model assumes that high-order harmonic radiation is emitted by electric dipoles. The respective electric dipole moment $\mathbf{D}(t) = q\langle \mathbf{r}(t) \rangle$ within the quantum mechanical realm is defined as the expectation value of the position operator

$$\mathbf{D}(t) = q \langle \Psi(\mathbf{r}, t) | \hat{\mathbf{r}} | \Psi(\mathbf{r}, t) \rangle. \quad (3.10)$$

Since the numerical solution of the *time-dependent Schrödinger equation* (TDSE) is computationally expensive, it is advantageous to approximate the system within a

DEFINITION 3.1: MAJOR ASSUMPTIONS OF THE SFA

- (i) The laser field only interacts with a single electron of the valence shell.
- (ii) The laser field does not couple to any bound state other than the ground state of the atomic target.
- (iii) The continuum states are described by Volkov states which neglect contributions of the atomic potential.
- (iv) The ground state wave function is known.
- (v) The incident laser field is locally homogeneous with regard to the atomic length scale.

meaningful context. The major assumptions of the SFA are highlighted below, while others are discussed later. However, the full set of assumptions is listed in Def. 3.1. The Hamiltonian of a charged particle dressed by an electromagnetic field and a static potential is given via

$$\hat{\mathcal{H}} = \frac{1}{2} \left(\hat{\mathbf{p}} - q\mathbf{A}(\mathbf{r}, t) \right)^2 + \hat{V}(\mathbf{r}) + q\Phi(\mathbf{r}, t), \quad (3.11)$$

with the scalar potential $\Phi(\mathbf{r}, t)$ and vector potential $\mathbf{A}(\mathbf{r}, t)$ of the incident laser field, the momentum operator $\hat{\mathbf{p}} = -i\hat{\nabla}_r$, the particle charge q , and the static potential $V(\mathbf{r})$. Here, the static potential is anticipated as the binding potential of the target atom or ion. The standard conditions of HHG are well-known [50, 66] and approximately lie at intensities of $I \sim 10^{14} \text{ W/cm}^2$, wavelengths of $\lambda \sim 1000 \text{ nm}$ and hydrogen-like atoms like argon with ionization potential $I_p = 15.76 \text{ eV}$. The respective Keldysh parameter (3.1) results as $\gamma \sim 0.3$, which lies within the tunnel ionization regime; see Tab. 3.1. Since the charged particle in the electromagnetic field is an electron, the respective charge reads $q = -1$. Furthermore, the system fulfills Def. 3.1(v) as the wavelength of the incident laser field is much larger than the diameter of the target atom, which validates the neglect of the spatial structure of the respective laser. This approximation is known as *dipole approximation* and condenses Eq. (3.11) to

$$\hat{\mathcal{H}} = \frac{1}{2} \left(\hat{\mathbf{p}} + \mathbf{A}(t) \right)^2 + \hat{V}(\mathbf{r}) - \Phi(\mathbf{r}, t). \quad (3.12)$$

The Hamiltonian in the dipole approximation essentially represents the nonrelativistic Coulomb Hamiltonian and is further termed the *dipole Hamiltonian* $\hat{\mathcal{H}}$ with its associated

dipole wavefunction Ψ . Since any spatial dependence of the vector potential would induce magnetic field contributions via $\mathbf{B}(\mathbf{r}, t) = \hat{\nabla}_{\mathbf{r}} \times \mathbf{A}(\mathbf{r}, t)$, they are associated with relativistic corrections as $\mathbf{B}(\mathbf{r}, t) \propto \frac{1}{c}$.

3.4.1. Dipole Volkov states

The dynamics of a charged particle in an external oscillating laser field are essential to accurately describe strong-field processes. The state which describes this system, the Volkov state, was first derived by Volkov [67] in 1935 as solutions of the Dirac equation for a superposition of monochromatic plane waves. The derivation of the nonrelativistic *dipole Volkov state* from the TDSE is shown in length and velocity gauge, which are commonly used in strong-field physics. Within the dipole approximation, the TDSE of a charged particle dressed by an electromagnetic field reads

$$i\hat{\partial}_t |\chi(t)\rangle = \hat{\mathcal{H}}_{le} |\chi(t)\rangle, \quad \hat{\mathcal{H}}_{le} = \frac{1}{2}(\hat{\mathbf{p}} + \mathbf{A}(t))^2 - \Phi(\mathbf{r}, t). \quad (3.13)$$

The vector potential vanishes in *length gauge* $\mathbf{A}(t) = 0$ such that the resulting dipole Hamiltonian reads

$$\hat{\mathcal{H}}_{le}^L = \frac{\hat{\mathbf{p}}^2}{2} - \Phi(\mathbf{r}, t), \quad \Phi(\mathbf{r}, t) = -\mathbf{r} \cdot \mathbf{E}(t), \quad (3.14)$$

while the scalar potential vanishes in *velocity gauge* $\Phi(\mathbf{r}, t) = 0$ and yields

$$\hat{\mathcal{H}}_{le}^V = \frac{1}{2}(\hat{\mathbf{p}} + \mathbf{A}(t))^2, \quad \mathbf{A}(t) = -\int^t d\tau \mathbf{E}(\tau). \quad (3.15)$$

The gauge function $\Lambda(\mathbf{r}, t) = -\mathbf{r} \cdot \mathbf{A}(t)$ in Eq. (2.3) transforms the velocity gauge dipole Hamiltonian into length gauge. Here, the derivation of the Volkov state in velocity gauge is rather simple and yields the TDSE in momentum space

$$i\hat{\partial}_t \chi(\mathbf{p}, t) = \frac{1}{2}(\hat{\mathbf{p}} + \mathbf{A}(t))^2 \chi(\mathbf{p}, t), \quad (3.16)$$

which is integrated and yields the Volkov state in the momentum space as

$$\chi(\mathbf{p}, t) = e^{-iS_V(\mathbf{p}, t)}, \quad S_V(\mathbf{p}, t) \equiv S_V(\mathbf{p}, t, -\infty) = \frac{1}{2} \int_{-\infty}^t d\tau \left(\mathbf{p} + \mathbf{A}(t) \right)^2, \quad (3.17)$$

with the *Volkov phase* $S_V(\mathbf{p}, t)$. Inverse Fourier transforming the state from momentum into real space then yields

$$\chi(\mathbf{r}, t) = \frac{1}{(2\pi)^{3/2}} e^{i\mathbf{r} \cdot \mathbf{p}} e^{-iS_V(\mathbf{p}, t)}. \quad (3.18)$$

The Volkov states in real space finally read

$$\chi_{\mathbf{p}}^{VG}(\mathbf{r}, t) = \frac{1}{(2\pi)^{3/2}} e^{i\mathbf{r} \cdot \mathbf{p} - iS_V(\mathbf{p}, t)}, \quad (3.19a)$$

$$\begin{aligned} \chi_{\mathbf{p}}^{LG}(\mathbf{r}, t) &= \chi_{\mathbf{p}}^{VG}(\mathbf{r}, t) e^{-i\Lambda(\mathbf{r}, t)} = \frac{1}{(2\pi)^{3/2}} e^{i\mathbf{r} \cdot [\hat{\mathbf{p}} + \mathbf{A}(t)]} e^{-iS_V(\mathbf{p}, t)}, \\ &= \langle \mathbf{r} | \mathbf{p} + \mathbf{A}(t) \rangle e^{-iS_V(\mathbf{p}, t)}. \end{aligned} \quad (3.19b)$$

Here, a gauge transformation, with gauge function $\Lambda(\mathbf{r}, t) = -\mathbf{r} \cdot \mathbf{A}(t)$, is applied to obtain the position space Volkov state in length gauge.

3.4.2. Gauge invariant strong-field transition amplitude

Invariant observables

Quantum mechanics is generally known to fulfill gauge invariance, which implies that physical observables do not depend on the chosen gauge. However, in recent years many theoretical investigations revealed an explicit gauge dependency in strong-field processes like ATI [68] or HHG [69]. This broken gauge invariance originates from insufficient approximations of the exact system. This section derives a gauge-invariant strong-field amplitude while following the gauge-fixing procedure presented in Ref. [70]. A similar approach within the relativistic regime is presented in Ref. [71, 72] for plane wave lasers. Furthermore, this section outlines the general issue that induces explicit gauge dependency within an intuitive context.

The choice of a particular gauge does not affect the physical fields, namely the electric and magnetic fields, as discussed in Sec. 2.1. In classical electrodynamics, the

scalar potential and the vector potential are valuable tools to describe the respective physical fields, even though these potentials are not mandatory for their description. Quantum mechanical systems, on the other hand, require these potentials [73] such that the respective gauge must be considered properly. In general, physical observables necessarily fulfill gauge invariance, which includes mathematically exact perturbation schemes. The expectation value of an arbitrary operator \hat{O} and its associated eigenstate Ψ can consequently be rewritten as a perturbative expansion. The expansion state Ψ_i and its associated operator \hat{O}_{ij} build up the exact expectation value via

$$\langle \Psi | \hat{O} | \Psi \rangle = \langle \Psi_0 | \hat{O}_{00} | \Psi_0 \rangle + \langle \Psi_1 | \hat{O}_{10} | \Psi_0 \rangle + \langle \Psi_0 | \hat{O}_{01} | \Psi_1 \rangle + \langle \Psi_1 | \hat{O}_{11} | \Psi_1 \rangle + \dots, \quad (3.20)$$

where the right-hand side needs to obey gauge invariance independently of its specific eigenstate expansion Ψ_i . This expansion does not explicitly determine the value of the respective perturbative contribution $\langle \Psi_i | \hat{O}_{ij} | \Psi_j \rangle$, but the sum of these contributions. In other words, $\langle \Psi_i | \hat{O}_{ij} | \Psi_j \rangle$ is indefinite, which naturally leads to a gauge dependency; see Ref. [68, 74–76]. In particular, interest lies in gauge-invariant expectation values for each perturbative order, such that the respective expansion of the expectation value, \hat{O} , may stop at a finite order $i \rightarrow i_{\text{end}}$ while still yielding physical (gauge invariant) observables. Therefore, it requires special care within the choice of the respective eigenstate expansion. Many investigations have shown that the so-called energy operator yields gauge-invariant strong-field amplitudes within a perturbative eigenstate expansion [77–79]. The following derivation explicitly highlights the gauge-invariant strong-field ionization amplitude.

The time evolution of the dipole Hamiltonian (3.12) is defined by the TDSE as

$$i\hat{\partial}_t |\Psi(\mathbf{r}, t)\rangle = \left[\frac{1}{2} (\hat{\mathbf{p}} + \mathbf{A}(t))^2 + \hat{V}(\mathbf{r}) - \Phi(\mathbf{r}, t) \right] |\Psi(\mathbf{r}, t)\rangle. \quad (3.21)$$

The dipole wave function $\Psi(\mathbf{r}, t)$ in combination with the arbitrary gauge function $\Lambda(\mathbf{r}, t)$ fulfills gauge invariance

$$\Psi' = U\Psi, \quad U = e^{-i\Lambda}, \quad U^\dagger U = 1, \quad (3.22)$$

if it satisfies the Schrödinger equation (3.21). Furthermore, an operator $\hat{O}(\mathbf{p}, \mathbf{r}, \mathbf{A}, \Phi)$ is referred to as gauge invariant and consequently represents a physical quantity [80] if the following identity holds

$$\hat{O}(\mathbf{p}, \mathbf{r}, \mathbf{A}, \Phi) = U \hat{O}(\mathbf{p}, \mathbf{r}, \mathbf{A}, \Phi) U^\dagger. \quad (3.23)$$

While the canonical momentum \mathbf{p} and the vector potential \mathbf{A} generally do not fulfill this condition

$$\begin{aligned}\hat{\mathbf{p}}' &= U\hat{\mathbf{p}}U^\dagger = \hat{\mathbf{p}} + \hat{\nabla}_r\Lambda(\mathbf{r}, t) \quad \Rightarrow \quad \hat{\mathbf{p}}' \neq \hat{\mathbf{p}}, \\ \mathbf{A}'(\mathbf{r}, t) &\stackrel{(2.3)}{=} \mathbf{A}(\mathbf{r}, t) + \hat{\nabla}_r\Lambda(\mathbf{r}, t) \quad \Rightarrow \quad \mathbf{A}'(\mathbf{r}, t) \neq \mathbf{A}(\mathbf{r}, t),\end{aligned}\quad (3.24)$$

the kinetic momentum $m_e\mathbf{v}_e = \mathbf{v}_e = \mathbf{p} + \mathbf{A}(\mathbf{r}, t)$ and the so-called *energy operator*

$$\begin{aligned}\hat{\mathcal{E}}(t) &= \frac{1}{2}(\hat{\mathbf{p}} + \mathbf{A}(t))^2 + \hat{V}(\mathbf{r}) \\ \Rightarrow \hat{\mathcal{E}}'(t) &= U\hat{\mathcal{E}}(t)U^\dagger = \frac{1}{2}(\hat{\mathbf{p}} + \mathbf{A}(t))^2 + \hat{V}(\mathbf{r}) = \hat{\mathcal{E}}(t),\end{aligned}\quad (3.25)$$

do. The dipole Hamiltonian (3.12) may decompose in terms of the energy operator and the scalar potential via

$$\hat{\mathcal{H}} = \hat{\mathcal{E}}(t) - \Phi(\mathbf{r}, t). \quad (3.26)$$

Consider an orthonormalized basis set $|\Psi_n(t)\rangle$ (bound states) of the field-free Hamiltonian $\hat{\mathcal{H}}_0 = \hat{\mathbf{p}}^2/2 + V(\mathbf{r})$ that obeys

$$\hat{\mathcal{H}}_0 |\Psi_n(t)\rangle = \epsilon_n |\Psi_n(t)\rangle \quad \text{and} \quad |\Psi_n(t)\rangle = e^{-i\epsilon_n t} |\Psi_n\rangle, \quad (3.27)$$

which leads to the associated *energy eigenstate* $|\Psi_n^\epsilon\rangle$ ¹

$$|\Psi_n^\epsilon(t)\rangle = e^{-ir \cdot \mathbf{A}(t)} |\Psi_n(t)\rangle \quad \Rightarrow \quad \hat{\mathcal{E}}(t) |\Psi_n^\epsilon(t)\rangle = \epsilon_n |\Psi_n^\epsilon(t)\rangle. \quad (3.28)$$

Time evolution operator

The time evolution operator $\hat{\mathcal{U}}(t, t')$ of the general wave function Φ fulfills

$$|\Phi(t)\rangle = \hat{\mathcal{U}}(t, t') |\Phi(t')\rangle, \quad (3.29)$$

¹Note, the energy operator generally depends on the vector potential of the laser field, while the respective eigenvalues ϵ_n do not

while the operator obeys the respective TDSE for a general Hamiltonian $\hat{\mathcal{H}}$ via

$$i\hat{\partial}_t\hat{\mathcal{U}}(t, t') = \hat{\mathcal{H}}(t)\hat{\mathcal{U}}(t, t'), \quad \text{with} \quad \hat{\mathcal{U}}(t, t) = 1 \quad (3.30)$$

The time evolution operator of the energy eigenstate (3.28) is then defined by

$$\begin{aligned} \hat{\mathcal{U}}_{\mathcal{E}}(t, t') &= \sum_n |\Psi_n^{\mathcal{E}}(t)\rangle \langle \Psi_n^{\mathcal{E}}(t')|, \\ &= e^{-ir \cdot \mathbf{A}(t)} \hat{\mathcal{U}}_0(t, t') e^{ir' \cdot \mathbf{A}(t')}, \end{aligned} \quad (3.31)$$

with the time evolution operator $\hat{\mathcal{U}}_0$ of the field-free Hamiltonian $\hat{\mathcal{H}}_0$ and the n -th eigenstate Ψ_n ($n = 0 \leftrightarrow$ ground state). $\hat{\mathcal{U}}_{\mathcal{E}}$ consequently fulfills the TDSE via

$$i\hat{\partial}_t\hat{\mathcal{U}}_{\mathcal{E}}(t, t') = \left(\hat{\mathcal{E}}(t) + \mathbf{r} \cdot \hat{\partial}_t \mathbf{A}(t) \right) \hat{\mathcal{U}}_{\mathcal{E}}(t, t'). \quad (3.32)$$

A convenient method to consider the time evolution of the system is to decompose the dipole Hamiltonian as

$$\begin{aligned} \hat{\mathcal{H}}(t) &= \hat{\mathcal{E}}(t) - \Phi(\mathbf{r}, t) = \hat{\mathcal{H}}_{\mathcal{E}}(t) + \hat{\mathcal{H}}_{int}(t), \\ \Rightarrow \hat{\mathcal{H}}_{\mathcal{E}}(t) &= \hat{\mathcal{E}}(t) + \mathbf{r} \cdot \hat{\partial}_t \mathbf{A}(t) \quad \text{and} \quad \hat{\mathcal{H}}_{int}(t) = - \left(\Phi(\mathbf{r}, t) + \mathbf{r} \cdot \hat{\partial}_t \mathbf{A}(t) \right), \end{aligned} \quad (3.33)$$

while further expressing the time evolution operator of the decomposed dipole Hamiltonian in terms of a Dyson series, defined in Def. 3.2. The respective Dyson series of the dipole time evolution operator consequently reads as

$$\hat{\mathcal{U}}(t, t') = \hat{\mathcal{U}}_{\mathcal{E}}(t, t') - i \int_{t'}^t d\tau \hat{\mathcal{U}}(t, \tau) \hat{\mathcal{H}}_{int}(\tau) \hat{\mathcal{U}}_{\mathcal{E}}(\tau, t'). \quad (3.34)$$

This representation holds for both length and velocity gauge where it considers the dipole time evolution operator (3.29) in the single electron approximation; see Def. 3.1(i).

Strong-field transition amplitude

Transition amplitudes are an essential component for describing many phenomena in nature and, particularly, in atomic physics. Strong-field ionization is associated with such amplitudes by the interaction of an atom with an intense laser field. The corresponding ionization amplitude is written in terms of the temporal evolution (3.34) of the dipole

DEFINITION 3.2: DYSON SERIES

The Hamiltonian of a system is defined as $\hat{\mathcal{H}}_C = \hat{\mathcal{H}}_A + \hat{\mathcal{H}}_B$ where the time evolution operator $\hat{\mathcal{U}}_j(t, t')$ of the Hamiltonian $\hat{\mathcal{H}}_j$ with $j \in \{A, B, C\}$ solves

$$i\hat{\partial}_t \hat{\mathcal{U}}_j(t, t') = \hat{\mathcal{H}}_j \hat{\mathcal{U}}_j(t, t') \quad \text{under} \quad \hat{\mathcal{U}}_j(t, t) = 1.$$

In terms of the Dyson series, the time evolution operator of the system reads as

$$\hat{\mathcal{U}}_C(t, t') = \hat{\mathcal{U}}_A(t, t') - i \int_{t'}^t d\tau \hat{\mathcal{U}}_C(t, \tau) \hat{\mathcal{H}}_B(\tau) \hat{\mathcal{U}}_A(\tau, t').$$

wave function via

$$\begin{aligned} M_{p,0} &= \lim_{t \rightarrow \infty} \langle \Psi_p(t) | \Psi(t) \rangle, \\ &= \lim_{t \rightarrow \infty, t_0 \rightarrow -\infty} \langle \Psi_p(t) | \hat{\mathcal{U}}(t, t_0) | \Psi_0(t_0) \rangle, \\ &= \lim_{t \rightarrow \infty, t_0 \rightarrow -\infty} \left[\langle \Psi_p(t) | \hat{\mathcal{U}}_{\mathcal{E}}(t, t_0) | \Psi_0(t_0) \rangle \right. \\ &\quad \left. - i \int_{t_0}^t d\tau \langle \Psi_p(t) | \hat{\mathcal{U}}(t, \tau) \hat{\mathcal{H}}_{int}(\tau) \hat{\mathcal{U}}_{\mathcal{E}}(\tau, t_0) | \Psi_0(t_0) \rangle \right]. \end{aligned} \quad (3.35)$$

Here, the first term in Eq. (3.35) vanishes in the limiting process, $(t, t_0) \rightarrow (\infty, -\infty)$, since the ground state $|\Psi_0\rangle$ and the continuum plane wave state $|\Psi_p\rangle$ are orthogonal eigenstates of the field-free Hamiltonian $\hat{\mathcal{H}}_0$. Iterative replacement of the dipole time evolution operator in the second term of Eq. (3.35) with its respective Dyson series (3.34) leads to higher-order contributions. However, the direct ionization amplitude is of particular interest and is calculated by utilizing the assumptions in Def. 3.1(i)-(iii)

$$M_{p,0} = \lim_{t \rightarrow \infty, t_0 \rightarrow -\infty} -i \int_{t_0}^t d\tau \langle \Psi_p(t) | \hat{\mathcal{U}}_{le}(t, \tau) \hat{\mathcal{H}}_{int}(\tau) \hat{\mathcal{U}}_{\mathcal{E}}(\tau, t_0) | \Psi_0(t_0) \rangle, \quad (3.36)$$

where the higher-order contributions of the Dyson series are neglected. The dipole time evolution operator subsequently reduces to the laser electron evolution operator $\hat{\mathcal{U}}_{le}$ by further assuming a vanishing contribution of the binding potential. Therefore, the laser electron time evolution operator replaces the dipole time evolution operator $\hat{\mathcal{U}} \Rightarrow \hat{\mathcal{U}}_{le}$, in the last line of Eq. (3.36). The Volkov state (3.19) finally describes the state of the ionized particle in the electromagnetic field, which was previously discussed in Sec. 3.4.1. Inserting the Volkov state into Eq. (3.36) and further utilizing Eq. (3.31) to evolve the bound state via $\hat{\mathcal{U}}_{\mathcal{E}}(\tau, t_0) | \Psi_0(t_0) \rangle = e^{-ir \cdot \mathbf{A}(\tau)} | \Psi_0(\tau) \rangle$ and the continuum state via

$\langle \Psi_{\mathbf{p}}(t) | \hat{\mathcal{U}}_e = \langle \chi_{\mathbf{p}}(\tau) |$ yields the direct ionization amplitude as ²

$$M_{\mathbf{p},0} = i \int_{-\infty}^{\infty} d\tau \langle \chi_{\mathbf{p}}(\tau) | e^{-i\mathbf{r} \cdot \mathbf{A}(\tau)} \left(\Phi(\mathbf{r}, \tau) + \mathbf{r} \cdot \hat{\partial}_{\tau} \mathbf{A}(\tau) \right) | \Psi_0(\tau) \rangle. \quad (3.37)$$

The remaining part of this section verifies and discusses the gauge invariance of the strong-field ionization amplitude (3.37) in length and velocity gauge. The ionization amplitude within the length gauge $\mathbf{A}(t) = 0 \rightarrow \Phi(\mathbf{r}, t) = -\mathbf{r} \cdot \mathbf{E}(t)$ results as

$$M_{\mathbf{p},0} = -i \int_{-\infty}^{\infty} d\tau \langle \chi_{\mathbf{p}}^{LG}(\tau) | \mathbf{r} \cdot \mathbf{E}(\tau) | \Psi_0(\tau) \rangle, \quad (3.38)$$

while the amplitude in velocity gauge $\Phi(\mathbf{r}, t) = 0 \rightarrow \mathbf{E}(t) = -\hat{\partial}_t \mathbf{A}(t)$ follows with

$$\begin{aligned} M_{\mathbf{p},0} &= i \int_{-\infty}^{\infty} d\tau \langle \chi_{\mathbf{p}}^{VG}(\tau) | e^{-i\mathbf{r} \cdot \mathbf{A}(\tau)} \mathbf{r} \cdot \hat{\partial}_t \mathbf{A}(\tau) | \Psi_0(\tau) \rangle, \\ &= -i \int_{-\infty}^{\infty} d\tau \langle \chi_{\mathbf{p}}^{LG}(\tau) | \mathbf{r} \cdot \mathbf{E}(\tau) | \Psi_0(\tau) \rangle. \end{aligned} \quad (3.39)$$

Note that the relation between the Volkov states in length and velocity gauge is equivalent to the hermitian conjugate of Eq. (3.19b) for the gauge function $\Lambda(\mathbf{r}, t) = -\mathbf{r} \cdot \mathbf{A}(t)$.

Overall, gauge invariance concerning length and velocity gauge is achieved after careful approximation of the system. In particular, this is done by perturbatively expanding the dipole wave function in terms of the energy eigenstate $|\Psi_n^{\mathcal{E}}(t)\rangle$. The eigenvalue of the energy operator is then associated with a *physical quantity* within this approximation scheme. The energy operator in *length gauge* reduces to the field-free Hamiltonian $\hat{\mathcal{H}}_0$ which guarantees gauge invariance since the latter corresponds to a physical quantity of the respective eigenstate $|\Psi_n(t)\rangle$. However, the field-free Hamiltonian is *generally a nonphysical quantity*, since the associate state is not an eigenstate of the energy operator. This is noticeable in *velocity gauge* where the Hamiltonian expands as $\hat{\mathcal{H}} = \hat{\mathcal{H}}_0 + \hat{\mathcal{H}}_{rad}$ with $\hat{\mathcal{H}}_{rad} = \mathbf{A}(t) \cdot \hat{\mathbf{p}} + \frac{1}{2} \mathbf{A}^2(t)$ and $\hat{\mathcal{H}}_0 = \hat{\mathbf{p}}^2/2 + V(\mathbf{r})$, respectively. The energy operator does not match the field-free Hamiltonian such that the expansion in terms of the eigenstates $|\Psi_n(t)\rangle$ results in gauge-dependent ionization amplitudes. Beyond this, there exists a vivid interpretation within an intuitive context. The Dyson series denotes a perturbative expansion in which $\hat{\mathcal{U}}$ is iteratively replaced by itself on the right-hand side

²The incident laser is turned off for $\tau \rightarrow -\infty$ which reduces the second exponential function of $\hat{\mathcal{U}}_{\mathcal{E}}(\tau, t_0)$ in Eq. (3.36) to one.

DEFINITION 3.3: HYDROGEN-LIKE DIPOLE MATRIX ELEMENT

The dipole matrix element of a hydrogen-like atom in the ground state reads

$$\mathbf{d}(\mathbf{p}) = \langle \mathbf{p} | \hat{\mathbf{r}} | \Psi_0 \rangle = -i \frac{2^{19/4} I_p^{5/4}}{\pi} \frac{\mathbf{p}}{(\mathbf{p}^2 + 2I_p)^3},$$

with the hydrogen-like ground state $|\Psi_0\rangle$ and the plane-wave state $\langle \mathbf{p} |$

$$|\Psi_0\rangle = \frac{(2I_p)^{3/4}}{\sqrt{\pi}} e^{-|r|\sqrt{2I_p}}, \quad \langle \mathbf{p} | \mathbf{r} \rangle = \frac{e^{-i\mathbf{r}\cdot\mathbf{p}}}{(2\pi)^{3/2}}.$$

of Eq. (3.34). Each iteration introduces further interactions to the dipole time evolution operator. The direct ionization amplitude corresponds to the first-order contribution and represents a single light-atom interaction at time τ . Even though the laser field affects the bound-state electron, these effects are associated with higher-order contributions and are consequently omitted in the first order. Therefore, the single interaction of the direct ionization amplitude is directly related to the ionization process itself. In such a system, the ground state $|\Psi_0(\tau)\rangle$ is not affected by the laser field. The respective energy eigenvalue ϵ_n of the bound-state electron in Eq. (3.28) is then time and laser field independent. The eigenvalue is consequently associated with the ionization potential as a physical quantity and is therefore gauge-independent.

3.4.3. Strong-field approximation

The strong-field approximation (SFA) by Lewenstein et al. [81] was developed in 1994 as a quantum mechanical approach for describing HHG on a microscopic scale. Alongside Lewenstein and his coworkers, Kulander [40, 82] performed crucial investigations, which led to the development of the three-step model.

However, starting from the dipole Hamiltonian (3.12) the TDSE reads

$$i\hat{\partial}_t |\Psi(t)\rangle = \hat{\mathcal{H}} |\Psi(t)\rangle = \hat{\mathcal{E}}(t) - \Phi(\mathbf{r}, t) |\Psi(t)\rangle, \quad (3.40)$$

with the energy operator $\hat{\mathcal{E}}$, defined in Eq. (3.25). The dipole wave function is then rewritten by the dipole time evolution operator (3.34) as

$$\begin{aligned} |\Psi(t)\rangle &= \hat{\mathcal{U}}(t, t_0) |\Psi(t_0)\rangle, \\ &\approx \hat{\mathcal{U}}_{\mathcal{E}}(t, t_0) |\Psi_0(t_0)\rangle - i \int_{t_0}^t d\tau \hat{\mathcal{U}}_{le}(t, \tau) \hat{\mathcal{H}}_{int}(\tau) \hat{\mathcal{U}}_{\mathcal{E}}(\tau, t_0) |\Psi_0(t_0)\rangle, \end{aligned} \quad (3.41)$$

while the time evolution operator in the second line is approximated by $\hat{\mathcal{U}} \Rightarrow \hat{\mathcal{U}}_{le}$, within the same context as discussed below Eq. (3.36). Here, t_0 denotes a time at which the laser pulse does not affect the system, so the system is well described by the field-free Hamiltonian. Inserting the approximate dipole wave function (3.41) into the atomic dipole moment (3.10) yields

$$\begin{aligned} \mathbf{D}(t) &= - \underbrace{\int_{t_0}^t \int_{t_0}^t d\tau d\tau' \langle \Psi_0(\tau') | e^{i\mathbf{r}\cdot\mathbf{A}(\tau')} \hat{\mathcal{H}}_{int}(\tau') \hat{\mathcal{U}}_{le}(\tau', t) \hat{\mathbf{r}} \hat{\mathcal{U}}_{le}(t, \tau) \hat{\mathcal{H}}_{int}(\tau) e^{-i\mathbf{r}\cdot\mathbf{A}(\tau)} | \Psi_0(\tau) \rangle}_{\approx 0} \\ &+ i \int_{t_0}^t d\tau \langle \Psi_0(t) | e^{i\mathbf{r}\cdot\mathbf{A}(t)} \hat{\mathbf{r}} \hat{\mathcal{U}}_{le}(t, \tau) \hat{\mathcal{H}}_{int}(\tau) e^{-i\mathbf{r}\cdot\mathbf{A}(\tau)} | \Psi_0(\tau) \rangle \\ &- i \int_{t_0}^t d\tau' \langle \Psi_0(\tau') | e^{i\mathbf{r}\cdot\mathbf{A}(\tau')} \hat{\mathcal{H}}_{int}(\tau') \hat{\mathcal{U}}_{le}(\tau', t) \hat{\mathbf{r}} e^{-i\mathbf{r}\cdot\mathbf{A}(t)} | \Psi_0(t) \rangle \\ &- \underbrace{\langle \Psi_0(t) | \hat{\mathbf{r}} | \Psi_0(t) \rangle}_{=0}, \end{aligned} \quad (3.42)$$

where the last term vanishes identically, and the first term denotes a higher-order contribution that is neglected. The remaining equation reads as follows

$$\begin{aligned} \mathbf{D}(t) &= i \int_{t_0}^t d\tau \langle \Psi_0(t) | e^{i\mathbf{r}\cdot\mathbf{A}(t)} \hat{\mathbf{r}} \hat{\mathcal{U}}_{le}(t, \tau) \hat{\mathcal{H}}_{int}(\tau) e^{-i\mathbf{r}\cdot\mathbf{A}(\tau)} | \Psi_0(\tau) \rangle, \\ &= i \int_{t_0}^t d\tau \int d^3\mathbf{p} \langle \Psi_0(t) | e^{i\mathbf{r}\cdot\mathbf{A}(t)} \hat{\mathbf{r}} | \chi_{\mathbf{p}}(t) \rangle \\ &\quad \times \langle \chi_{\mathbf{p}}(\tau) | \hat{\mathcal{H}}_{int}(\tau) e^{-i\mathbf{r}\cdot\mathbf{A}(\tau)} | \Psi_0(\tau) \rangle, \\ &= i \int_{t_0}^t d\tau \int d^3\mathbf{p} \langle \Psi_0 | \hat{\mathbf{r}} | \mathbf{p} + \mathbf{A}(t) \rangle \langle \mathbf{p} + \mathbf{A}(\tau) | \hat{\mathcal{H}}_{int}(\tau) | \Psi_0 \rangle \\ &\quad \times e^{i\epsilon_0(t-\tau)} e^{-iS_V(\mathbf{p}, t, \tau)}, \end{aligned} \quad (3.43)$$

where one inserts the definition of the Volkov state (3.19) and further uses $\hat{\mathcal{U}}_{le}(t, \tau) = \int d^3\mathbf{p} |\chi_{\mathbf{p}}(t)\rangle \langle \chi_{\mathbf{p}}(\tau)|$ as well as the definition of $|\Psi_n(t)\rangle$ (3.27). After inserting the interaction Hamiltonian (3.33) and selecting a respective gauge, the atomic dipole

moment reads

$$\mathbf{D}(t) = i \int_{t_0}^t dt' \int d^3\mathbf{p} \overbrace{\mathbf{d}^\dagger(\mathbf{p} + \mathbf{A}(t))}^{\text{recombination}} \underbrace{\left[\mathbf{E}(t') \cdot \mathbf{d}(\mathbf{p} + \mathbf{A}(t')) \right]}_{\text{ionization}} \overbrace{e^{-iS(\mathbf{p}, t, t')}}^{\text{propagation}}, \quad (3.44)$$

$$S(\mathbf{p}, t, t') = \frac{1}{2} \int_{t'}^t d\tau \left[(\mathbf{p} + \mathbf{A}(t))^2 + 2I_p \right], \quad (3.45)$$

where one changes the integration parameter $\tau \rightarrow t'$, inserts the ionization potential $I_p = -\epsilon_0$ and introduces the quasi-classical action $S(t, t')$. Furthermore, the *dipole matrix element* and its Hermitian conjugation are defined as

$$\mathbf{d}(\mathbf{p}) = \langle \mathbf{p} | \hat{\mathbf{r}} | \Psi_0 \rangle, \quad \mathbf{d}^\dagger(\mathbf{p}) = \langle \Psi_0 | \hat{\mathbf{r}} | \mathbf{p} \rangle, \quad (3.46)$$

which are associated with the ionization and recombination of an electron and its parent ion, respectively. The atomic dipole moment (3.44) is related to the three-step model by a quasi-classical interpretation. First, the factor $\mathbf{E}(t') \cdot \mathbf{d}(\mathbf{p} + \mathbf{A}(t'))$ considers the laser-field-induced ionization, while second, the electron propagation in the continuum is imprinted on the quasi-classical action in $\exp(-iS(\mathbf{p}, t, t'))$. In the end, the dipole matrix element $\mathbf{d}^\dagger(\hat{\mathbf{p}} + \mathbf{A}(t))$ represents the recombination of the continuum electron with its parent ion. These matrix elements denote the transitions between a hydrogen-like ground state and a plane-wave continuum state. Even though this approximation is generally limited to hydrogen and helium, elements with a similar structure, e.g. other noble gases, may be considered as well. The respective dipole matrix element is defined in Def. 3.3.

Saddle-point approximation

The effort to compute Eq. (3.44) numerically is often too high for practical purposes. This effort originates from the three-dimensional momentum integral in combination with the rapid phase oscillation of the exponential $\exp(-iS(\mathbf{p}, t, t'))$. There exist different approaches to simplify the respective momentum integral extensively. However, this section discusses a commonly utilized approach, namely the so-called *saddle-point approximation* (SPA). The SPA, defined in Def. 3.4, is an analytical technique to approximate rapidly oscillating integrals in which the accuracy increases for faster oscillating functions. Here, the scalar function in Def. 3.4 is associated with the quasi-classical action $\phi(\mathbf{p}) \Leftrightarrow S(\mathbf{p}, t, t')$ while $\mathbf{G}(\mathbf{p})$ identifies with the residual integrand. The dominant contribution of the canonical momentum \mathbf{p} in the quasi-classical action is proportional to $\exp(i\mathbf{p}^2)$, which

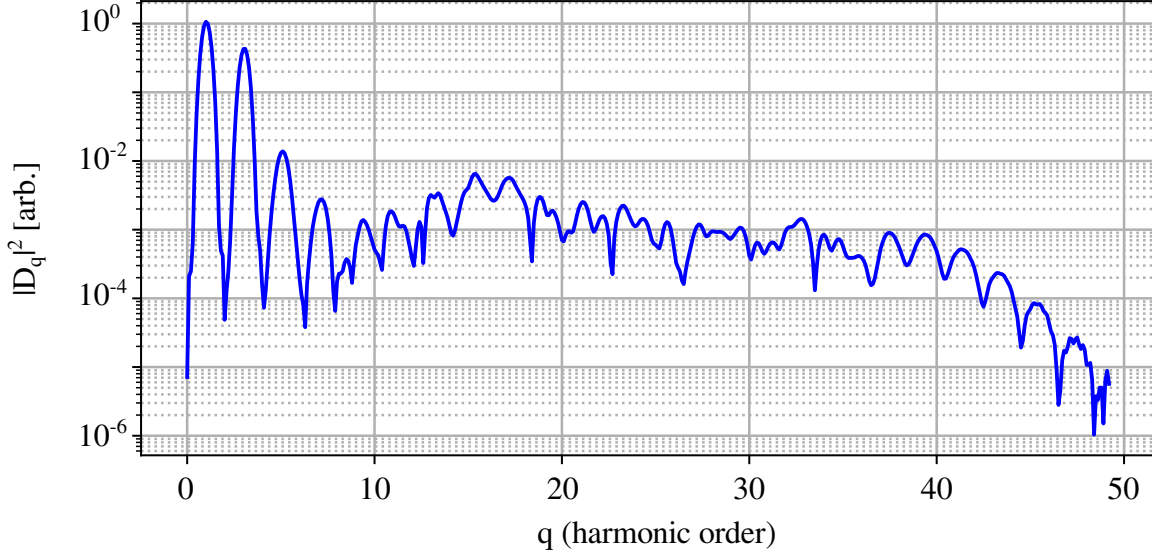


Figure 3.4.: HHG spectrum within the Lewenstein model. The atomic dipole moment $|D_q|$ of an argon atom is shown about the harmonic order q for an incident \sin^2 laser pulse (2.19) of three optical periods with a fundamental wavelength of $\lambda = 1030$ nm (Yb:YAG-laser) and intensity $I_0 = 1 \cdot 10^{14}$ W/cm².

DEFINITION 3.4: SADDLE-POINT APPROXIMATION

Let \mathbf{F} be the m -dimensional complex vector given by

$$\mathbf{F} = \int_{x_0}^{x_1} d\mathbf{x} \mathbf{G}(\mathbf{x}) e^{i\phi(\mathbf{x})},$$

with the m -dimensional function $\mathbf{G}(\mathbf{x})$ and the scalar function $\phi(\mathbf{x})$ that depend on the n -dimensional vector \mathbf{x} . Let $\mathbf{G}(\mathbf{x})$ vary much slower than $e^{i\phi(\mathbf{x})}$ for all $\mathbf{x} \in [x_0, x_1]$. The saddle-point approximation of \mathbf{F} is then defined via

$$\mathbf{F} = \int_{x_0}^{x_1} d\mathbf{x} \mathbf{G}(\mathbf{x}) e^{i\phi(\mathbf{x})} \approx \sum_s \sqrt{\frac{(2\pi i)^n}{H_x(\phi(\mathbf{x}))|_{\mathbf{x}=\mathbf{x}_s}}} \mathbf{G}(\mathbf{x}_s) e^{i\phi(\mathbf{x}_s)},$$

where $H_x(\phi(\mathbf{x}))$ denotes the Hessian determinant of $\phi(\mathbf{x})$ at the saddle point \mathbf{x}_s . The saddle points \mathbf{x}_s fulfill the condition $0 = \hat{\nabla}_x \phi(\mathbf{x})|_{\mathbf{x}=\mathbf{x}_s}$. More detailed information about the saddle-point approximation can be found at Ref. [83–86].

oscillates much faster than the remaining integrand. The momentum dependence of \mathbf{G} is encoded in the dipole matrix elements, where the dominant contribution obeys $\mathbf{G} \propto \mathbf{p}^{-2}$.

The SPA consequently applies since the exponential function evolves significantly faster as a function of the canonical momentum than the remaining integrand.

The saddle-point momentum \mathbf{p}_s is unambiguously identified by the quadratic dependency of the kinetic momentum $\mathbf{p} + \mathbf{A}(\tau)$ in the action as

$$\begin{aligned}\hat{\nabla}_{\mathbf{p}}S(\mathbf{p}, t, t') &\equiv 0 = \int_{t'}^t d\tau (\mathbf{p} + \mathbf{A}(t)) \\ \Rightarrow \mathbf{p}_s(t, t') &= -\frac{1}{t-t'} \int_{t'}^t d\tau \mathbf{A}(\tau),\end{aligned}\quad (3.47)$$

$$H_{\mathbf{p}}(S(\mathbf{p}))|_{\mathbf{p}=\mathbf{p}_s} = |\hat{\nabla}_{\mathbf{p}}\hat{\nabla}_{\mathbf{p}}S(\mathbf{p})|_{\mathbf{p}=\mathbf{p}_s} = -(t-t')^3, \quad \forall t > t', \quad (3.48)$$

while $H_{\mathbf{p}}(\phi(\mathbf{p}))$ is the determinant of the respective Hesse matrix. Applying the SPA (Def. 3.4) to the atomic dipole moment in Eq. (3.44) then yields

$$\begin{aligned}\mathbf{D}(t) &= i \int_{-\infty}^t dt' \left(\frac{-2\pi i}{t-t'}\right)^{3/2} \\ &\times \mathbf{d}^\dagger(\mathbf{p}_s + \mathbf{A}(t)) \left[\mathbf{E}(t') \cdot \mathbf{d}(\mathbf{p}_s + \mathbf{A}(t')) \right] e^{-iS(\mathbf{p}_s, t, t')}.\end{aligned}\quad (3.49)$$

where t_0 approaches infinity. The saddle-point momentum is associated with the kinetic momentum of the electron in the continuum, whereas the momentum integration corresponds to the interference of different *quantum-paths* in the spirit of Feynman's path integral formalism [87].

Computations of Eq. (3.49) are performed for a Yb: YAG-laser [88] with an argon target atom. Figure 3.4 illustrates the respective harmonic spectrum, which represents the Fourier transform of Eq. (3.49) from the time, into the frequency domain. The characteristic plateau region ($8 < q < 39$) is clearly visible and results in the consequence of the nonlinear laser-atom interaction. The atomic dipole moment decreases exponentially outside of the plateau region, where the region of low-order harmonics ($q < 8$) is referred to as the perturbative region, while the region with higher-order harmonics ($q > 39$) is associated with the high-order harmonic (HH) cutoff $q_c = (3.17U_p + I_p)/\omega$.

3.4.4. Quantum Orbit approach

The *Quantum-Orbit* (QO) approach denotes a further approximation of the atomic dipole moment within the frequency domain

$$\begin{aligned} \mathbf{D}(q) &\equiv \mathbf{D}_q = \int_{-\infty}^{\infty} dt \mathbf{D}(t) e^{i\omega_q t}, \\ &= i \int_{-\infty}^{\infty} dt \int_{-\infty}^t dt' \left(\frac{-2\pi i}{t-t'} \right)^{3/2} \mathbf{d}^\dagger(\mathbf{p}_s + \mathbf{A}(t)) \\ &\quad \times \left[\mathbf{E}(t') \cdot \mathbf{d}(\mathbf{p}_s + \mathbf{A}(t')) \right] e^{-i\Theta(t,t')}, \end{aligned} \quad (3.50)$$

with the intrinsic phase $\Theta(t, t') \equiv S(\mathbf{p}_s, t, t') - i\omega_q t$ and the energy ω_q of the q -th order harmonic. The QO approach utilizes the SPA to approximate both temporal integrals, where the SPA applies to the rapidly oscillating complex exponential $\exp(-i\Theta(t, t'))$, similar to the SPA discussed in Sec. 3.4.3. The temporal saddle points are significantly more difficult to determine compared to the closed analytic form of the respective saddle-point momentum in Eq. (3.47). The temporal saddle points (t_s, t'_s) must satisfy their respective saddle-point condition, which reads

$$0 \equiv \hat{\partial}_{t'} \Theta(t, t')|_{(t,t')=(t_s,t'_s)} \Rightarrow \frac{1}{2} (\mathbf{p}_s(t_s, t'_s) + \mathbf{A}(t'_s))^2 = -I_p, \quad (3.51a)$$

$$0 \equiv \hat{\partial}_t \Theta(t, t')|_{(t,t')=(t_s,t'_s)} \Rightarrow \frac{1}{2} (\mathbf{p}_s(t_s, t'_s) + \mathbf{A}(t_s))^2 = \omega_q - I_p. \quad (3.51b)$$

The saddle points t'_s and t_s quasi-classically represent the *ionization* and *recombination* time of the electron, respectively. By physical means, Eq. (3.51a) and Eq. (3.51b) separately ensure energy conservation in the instance of ionization and recombination. The saddle points explicitly depend on the specific time evolution of the laser field such that no general solution can be drawn, in contrast to Eq. (3.47). The complexity increases even further as the saddle points are complex numbers, which may be deduced from Eq. (3.51a) where the kinetic energy of the continuum electron needs to be below zero to obey the saddle-point condition. The ionization time consequently possesses an imaginary part that is associated with the tunneling time. The separate equations in (3.51) are coupled to each other via the saddle-point momentum \mathbf{p}_s , which depends on t_s and t'_s . The saddle-point momentum \mathbf{p}_s and recombination time t_s are, consequently, complex numbers as well. For a set of saddle points with complex values (t_s, t'_s) , the dimensionality of the coupled nonlinear equations rises from two to four, which substantially increases the complexity of the saddle-point condition. In general, the saddle-point condition

(3.47) is a four-dimensional system of coupled nonlinear equations that needs to be solved numerically as a consequence of its algebraic complexity.

Solutions to the saddle-point condition

The numerical solution of Eq. (3.51) reveals two distinct sets of saddle points within one optical cycle. Lewenstein et al. [81] phrased them as *short* and *long* solutions, which refers to the (real) travel time of the electron in the continuum with its characteristic short and long trajectory. Figure 3.5 explicitly shows the solution of the saddle-point condition (3.51) for a linearly polarized laser beam with fundamental wavelength $\lambda = 1000$ nm, intensity $I_0 = 4 \cdot 10^{14}$ W/cm² and ionization potential of $I_p = 21.56$ eV (Ne). The short and long trajectories are colored red and green, respectively, while the ionization and recombination times differentiate via a star- and circular-shaped marker. The solid-blue line refers to a positive electric field amplitude, while the dotted-blue line indicates a negative one. Generally, continuous beams possess an infinite number of saddle-point sets that obey the respective saddle-point condition. The set associated with the dominant contribution is discussed in the following, while others are neglected. A more detailed discussion is presented in Ref. [89]. One remarkable feature is observed for increasing energies E_q where the ionization and recombination times of the respective trajectories (same shape) approach each other. Note that the short trajectory is neglected close to the cutoff energy $E_c = q_c \omega \approx 140$ eV. This neglect results due to the unphysical character of the respective solution for the short trajectory, which originates in the imaginary component of the ionization and recombination time; see Ref. [90].

However, with the shorthand notation of the Hessian determinant

$$\det(\Theta''(t_s, t'_s)) \equiv H_{(t,t')}(\Theta(t, t')) \Big|_{(t,t')=(t_s,t'_s)}, \quad (3.52)$$

the atomic dipole moment in the QO approach finally reads

$$\begin{aligned} \mathbf{D}_q = & \sum_{s=(t_s, t'_s)} \left(\frac{-2\pi i}{t_s - t'_s} \right)^{3/2} \frac{2\pi}{\sqrt{\det(\Theta''(t_s, t'_s))}} \mathbf{d}^\dagger(\mathbf{p}_s(t_s, t'_s) + \mathbf{A}(t_s)) \\ & \times [\mathbf{E}(t'_s) \cdot \mathbf{d}(\mathbf{p}_s(t_s, t'_s) + \mathbf{A}(t'))] e^{-i\Theta(t_s, t'_s)}. \end{aligned} \quad (3.53)$$

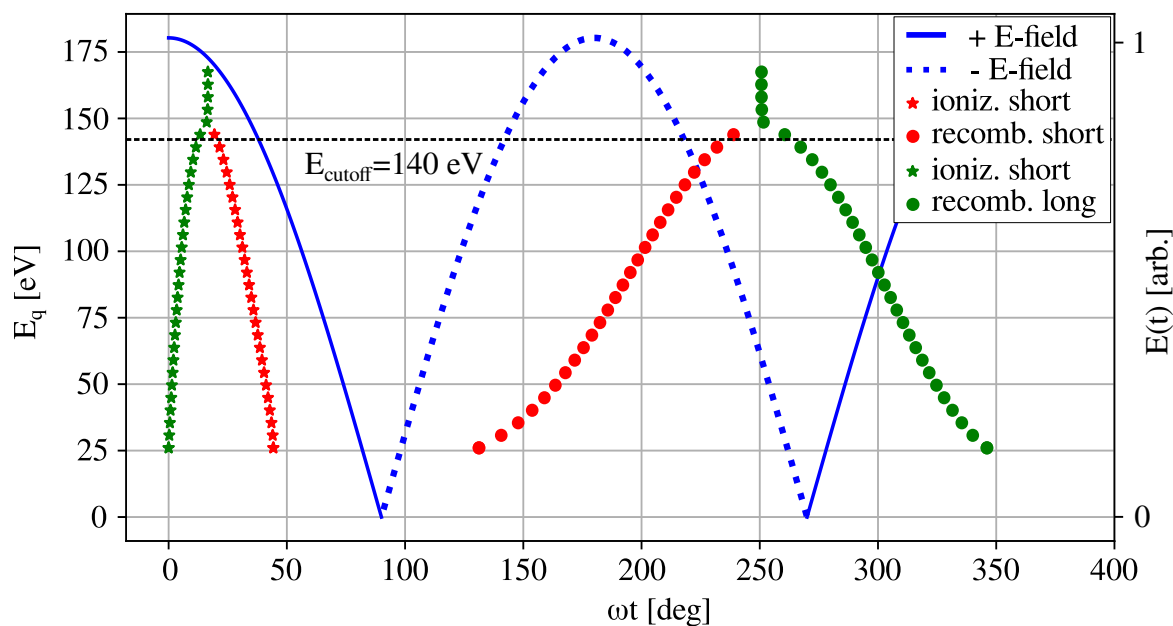


Figure 3.5.: The real part of the ionization and recombination times (3.51) is shown (see legend) for increasing photon energies within one optical period of the incident laser field. The classical cutoff energy is indicated by the dashed-black line while the setup parameters are chosen as, $\lambda = 1000$ nm, $I_0 = 4 \cdot 10^{14}$ W/cm², and $I_p = 21.56$ eV (Ne).

This formulation of the atomic dipole moment not only avoids extended numerical computations of highly oscillating five-dimensional integrals but also yields a quasi-classical interpretation of the physical process. The quasi-classical picture reveals sets of solutions (t_s, t'_s) that are associated with characteristic electron trajectories [89]. The spectrum associated with the saddle points in Fig. 3.5 is visualized in Fig. 3.6 (solid-blue line) alongside other spectra that are computed within the QO approach with intensity $I_0 = 4 \cdot 10^{14}$ W/cm² and ionization potential of $I_p = 21.56$ eV. The HH cutoff q_c matches the one illustrated in Fig. 3.5. The QO approach has been shown to provide deep insight into the underlying dynamics of HHG.

The discussed dipole SFA is unfortunately not able to properly describe the generation of HH radiation with an energy range of several keV's. To do so, the SFA needs to be extended toward the weakly relativistic regime which is done in Chap.5.

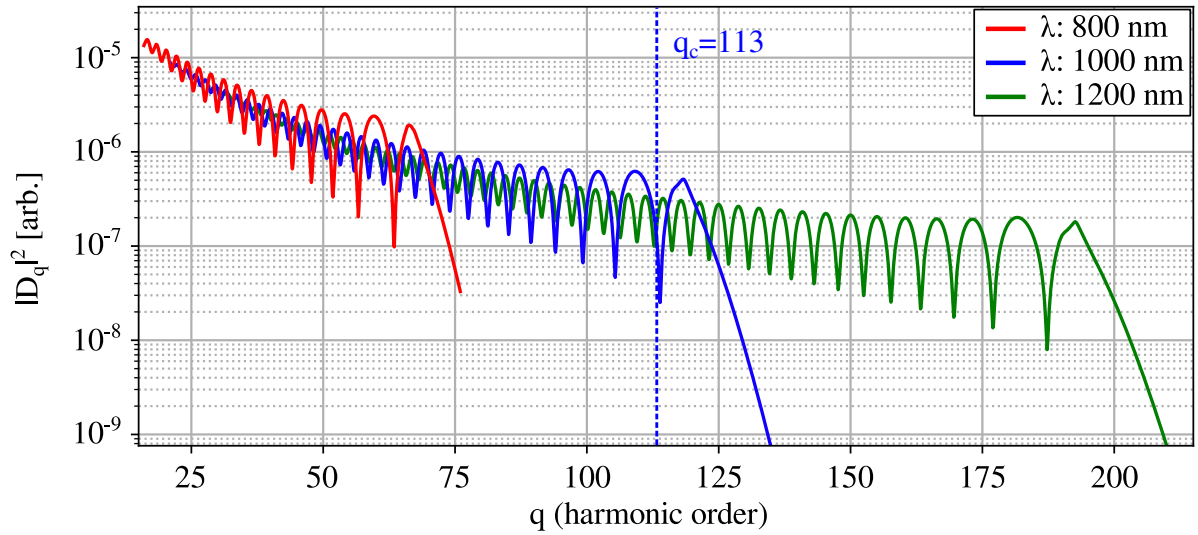


Figure 3.6.: HHG spectrum within the quantum orbit approach, where only the two dominant trajectories are considered. The highlighted HH cutoff (dashed-blue line) corresponds to the cutoff energy of $E_c = q_c \omega \approx 140$, eV, which is also indicated in Fig. 3.5.

CHAPTER 4.

HIGH-ORDER HARMONIC GENERATION BY SPATIALLY STRUCTURED LIGHT

“What we observe is not nature itself, but nature exposed to our method of questioning”

— Werner Heisenberg

Light-atom interactions induced by intense laser fields have attracted much attention in recent decades. Several applications like pump-probe experiments [91] and imaging techniques [92] have benefited from extremely short and energetic pulses from HHG. These short pulses are a direct consequence of the huge spectral bandwidth of the high-order harmonic (HH) radiation. The generation of extremely short pulses by HHG, therefore, often requires high cutoff energies. Unfortunately, these cutoff energies are associated with a weakly and fully relativistic treatment of the HHG process [23, 24, 93, 94]. An extension of the nonrelativistic models toward weakly relativistic dynamics is of interest since current laser technologies approach the respective nonrelativistic limits of the SFA. The weakly relativistic regime is in contrast to the fully relativistic regime, mathematically less complex, and offers the opportunity to consider the spatial structure of an incident laser field within the microscopic realm.

Parts of the material presented in this chapter were previously published in:

Generalized nondipole strong-field approximation of high-order harmonic generation.

Minneker, B.; Böning, B.; Fritzsche, S.

[Phys. Rev. A 2022, 106, 053109.](#)

Ongoing research in strong-field physics led to different approaches to solving the time-dependent Schrödinger equation (TDSE). One of the most successful approaches, apart from numerical solution [95], is the strong-field approximation (SFA) [81, 96]; see Chap. 3. The standard SFA requires analytic electron states in a dressed continuum Def. 3.1(iii), also known as Volkov states. The Volkov states were initially constructed as solutions of the fully relativistic Dirac equation [67], where the nonrelativistic Volkov states also refer to as dipole Volkov states; see Sec. 3.4.1. The latter consists of a plane wave with an additionally purely time-dependent phase, the so-called dipole Volkov phase. The associated nonrelativistic or *dipole SFA* has been thoroughly compared to HHG experiments and found valid for a broad range of parameters. However, laser fields have recently approached the limits of these nonrelativistic models [97]. Therefore, more sophisticated models towards the weakly relativistic regime are required to investigate HHG with those lasers. The weakly relativistic extension of the dipole SFA is also known as *nondipole SFA* and incorporates contributions proportional to $1/c$. Many investigations on the nondipole SFA, and in particular the one on HHG, introduce the weakly relativistic contributions, by Taylor expanding the electromagnetic potentials of the respective laser field to the first relativistic order [30, 93, 98–103]. Other investigations further extended the strong-field processes toward electric and magnetic nondipole effects [104] or compared different nondipole approaches [105]. While HHG induced by plane-wave lasers is well described by current nondipole models, other classes of light fields such as Gaussian or Bessel beams are not.

This chapter provides a nondipole strong-field approximation that incorporates analytically accurate nondipole Volkov states. These Volkov states consider weakly relativistic contributions of arbitrarily spatially structured light fields. In addition, the developed nondipole SFA is valid for complicated beam arrangements and is especially not limited to collinear beam arrangements. In general, one can not only incorporate an arbitrary number of laser fields but also account for their individual weakly relativistic contribution. Overall, the developed nondipole SFA is valid for the same laser field configurations that are available in the dipole SFA. Explicitly, the developed model supports an arbitrary superposition of *paraxial/nonparaxial*, *collinear/noncollinear*, *polychromatic*, and *spatially structured light fields*. Accordingly, it truly represents a generalization of the dipole SFA to the weakly relativistic regime. Therefore, the model is referred to as *generalized nondipole SFA* (GN-SFA). Figure 4.1 illustrates the respective validity interval, compared to the dipole SFA and standard nondipole SFA. As in the standard dipole SFA, several microscopic and macroscopic effects like phase matching or ground state depletion are not explicitly considered in this dissertation. Although further research is necessary

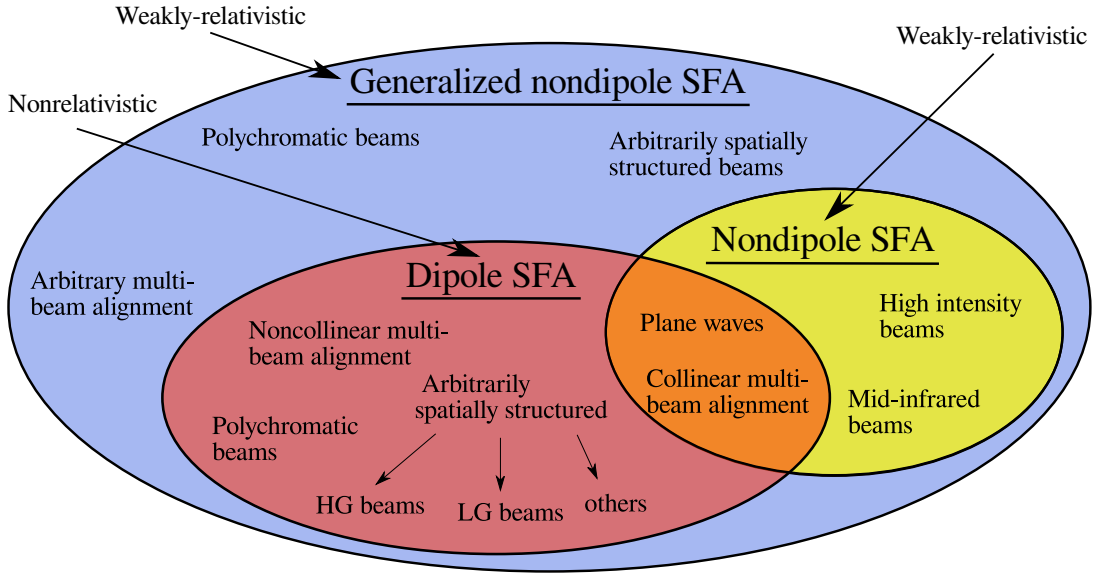


Figure 4.1.: Incident laser field configurations that can be described by the dipole SFA (red ellipse), standard nondipole SFA (yellow ellipse), and the generalized nondipole SFA (blue ellipse). Terms that appear twice differ in their interval of validity concerning nonrelativistic and weakly relativistic effects.

to incorporate these effects, the general results presented in this dissertation are not affected.

4.1. Electron dynamics in weakly relativistic laser fields

A preliminary discussion on electron dynamics in an intense electromagnetic field is advantageous to develop an intuitive understanding of nondipole effects. Let the laser field be a linearly polarized plane wave with a wave vector $\mathbf{k} = k\mathbf{e}_z$. In the dipole approximation, the vector potential parametrically depends on its respective spatial structure $\mathbf{A}(\mathbf{r}, t) \approx \mathbf{A}(\mathbf{r}_0, t)$, as discussed in Sec. 2.3. The vector potential is consequently a purely time-dependent field in the microscopic regime. This absent spatial structure of the laser field essentially enables and simplifies the development of analytic models. Including the spatial structure of a light field is in the first instance understood as considering its respective magnetic field $\mathbf{B} \neq 0$ or weakly relativistic effects; see Def. 2.1. The effects of spatially structured light fields on electrons are therefore usually known as magnetic, nondipole, or weakly-relativistic effects. The resulting classical electron motion in a plane wave laser field is determined by the relativistic Lorentz equation [106]. In

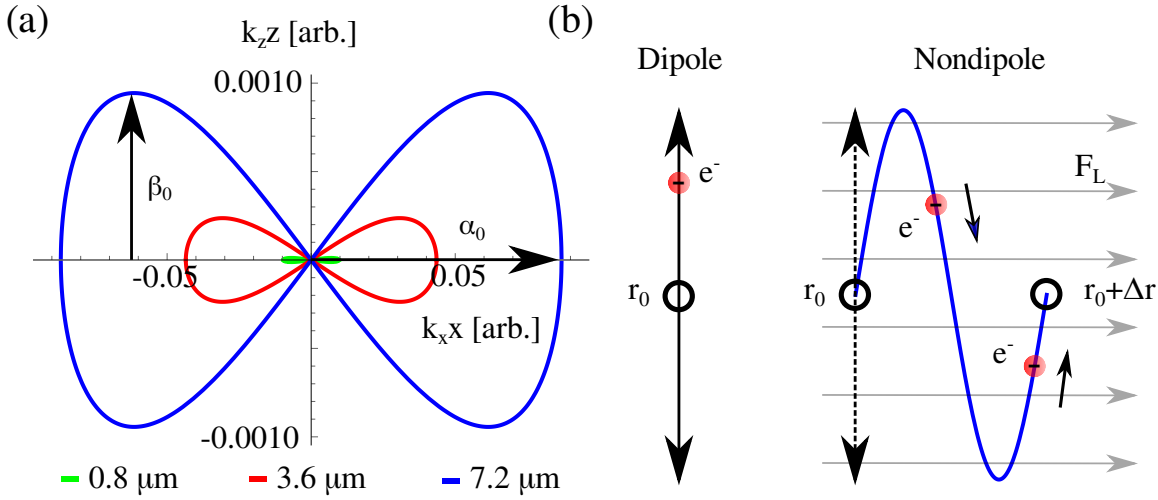


Figure 4.2.: Motion of an electron in a linearly polarized plane wave field within one optical period. (a) Averaged rest frame: The electron motion is shown in its averaged rest frame. Oscillations within the dipole regime are associated with α_0 (x-axis), while β_0 (y-axis) accounts for the nondipole ones. (b) Lab frame: The electron (red) is driven by the dipole field of the plane wave (left) with initial and final position \mathbf{r}_0 (ring). Nondipole contributions additionally lead to an electron drift, induced by the Lorentz force. The electron drifts apart from its initial position along the propagation axis such that the final position does not match the initial one. This drift $\Delta\mathbf{r}$ is referred to as the magnetic displacement.

addition to the motion related to the dipole approximation, the magnetic field induces a so-called *magnetic displacement*, which continuously drifts the electron toward the beam propagation direction \mathbf{k} . This magnetic displacement is associated with the Lorentz force of a plane-wave laser field.

In other words, the drift direction of the electron is constant and leads to a continuous drift apart from its initial position along the optical axis.

4.1.1. Influence of the spatial laser structure

The 1970 work of Sarachik and Schappert [107] investigates the relativistic motion of electrons within intense electromagnetic fields. The influence of the laser field's spatial structure is quantified by transforming the equation of motion into the averaged rest frame of the electron. Within this frame, the electron motion extends from the one-dimensional x-axis (nonrelativistic) to the two-dimensional x-z-plane (relativistic). The latter essentially represents a two-dimensional oscillation induced by the electric (x-axis) and magnetic field (z-axis) of the laser. The two-dimensional oscillation is also

known as *figure-eight motion* and is visualized in Fig. 4.2a. The figure-eight motion is characterized by the two amplitudes α_0 and β_0 . Here, β_0 represents the amplitude in the laser propagation direction and is defined by [108]

$$\beta_0 \approx \frac{U_p}{4c\omega} = \frac{E_0^2}{16c\omega^3} \propto I_0\lambda^3, \quad (4.1)$$

with the ponderomotive energy U_p (3.2), the intensity I_0 (2.10), the wavelength λ and the frequency ω of the laser beam. In general, the dipole approximation remains valid for small amplitudes β_0 compared to the Bohr radius $a_0 = 4\pi\epsilon_0\hbar^2/m_e e^2 = 1 \text{ a.u.} \approx 0.05 \text{ nm}$ [109], while relativistic effects significantly influence the electron motion if β_0 approaches the Bohr radius $\beta_0 \approx 1$. However, nondipole effects already affect the electron's motion below the latter threshold. Figure 4.2a shows the figure-eight motion for different incident wavelengths and a constant intensity of $I_0 = 2 \cdot 10^{14} \text{ W/cm}^2$. The separate figure eight motions are associated with the dipole regime for $\lambda = 0.8 \mu\text{m}$ (green), the border to the nondipole regime with $\lambda = 3.2 \mu\text{m}$ (red), and the nondipole regime by $\lambda = 7.2 \mu\text{m}$ (blue). The typical parameter space of laser fields utilized in HHG is associated with wavelengths in the near- to mid-infrared and intensities of $10^{13} - 10^{16} \text{ W/cm}^2$. The upper end of this parameter space, namely mid-infrared wavelengths and intensities up to 10^{16} W/cm^2 , is known to induce significant nondipole effects, which properly need to be considered in the theoretical models.

4.1.2. Nondipole Volkov states

The TDSE yields a quantum mechanical description of a continuum electron dressed by an electromagnetic field. These continuum states are eigenstates of the laser-electron Hamiltonian. Within velocity gauge, the Hamiltonian is also known as the minimal coupling Hamiltonian and reads

$$\hat{\mathcal{H}}_{le} = \frac{1}{2}(\hat{\mathbf{p}} + \mathbf{A}(\hat{\mathbf{r}}, t))^2 = \frac{1}{2}(\hat{\mathbf{p}}^2 + 2\hat{\mathbf{p}} \cdot \mathbf{A}(\hat{\mathbf{r}}, t) + \mathbf{A}^2(\hat{\mathbf{r}}, t)). \quad (4.2)$$

It is beneficial to name the respective contributions within a physical context to simplify further discussions. The contribution that depends linearly on the vector potential and the canonical momentum $\hat{\mathbf{p}} \cdot \mathbf{A}(\mathbf{r}, t)$ is defined as *particle-field contribution*, while the term $\mathbf{A}^2(\mathbf{r}, t)/2$ refers to as the respective *field-field contribution*. Note, the position operator has changed as $\hat{\mathbf{r}} \rightarrow \mathbf{r}$ since this chapter mainly operates in real space in which the position operator is trivial. So far, no general solution of the TDSE exists concerning

the minimal coupling Hamiltonian (4.2) for vector potentials of an arbitrary spatial structure

$$i\hat{\partial}_t|\chi_{\mathbf{p}}^{ND}(t)\rangle = \frac{(\hat{\mathbf{p}} + \mathbf{A}(\mathbf{r}, t))^2}{2} |\chi_{\mathbf{p}}^{ND}(t)\rangle. \quad (4.3)$$

However, there exist solutions for a general vector potential, defined in Def. 2.3. These solutions are the so-called *nondipole Volkov states* $|\chi_{\mathbf{p}}^{ND}(t)\rangle$, which are analytically exact up to the first relativistic order and are given by [110–112]

$$\langle \mathbf{r} | \chi_{\mathbf{p}}^{ND}(t) \rangle = \frac{1}{(2\pi)^{3/2}} e^{-i(E_{\mathbf{p}}t - \mathbf{p}\cdot\mathbf{r}) - i\Gamma(\mathbf{r}, t)} = e^{-i[E_{\mathbf{p}}t + \Gamma(\mathbf{r}, t)]} \langle \mathbf{r} | \mathbf{p} \rangle, \quad E_{\mathbf{p}} = \mathbf{p}^2/2. \quad (4.4)$$

These nondipole Volkov states consist of a plane wave $e^{-i(E_{\mathbf{p}}t - \mathbf{p}\cdot\mathbf{r})}$, tailored by the nondipole Volkov phase $e^{-i\Gamma(\mathbf{r}, t)}$, which is explicitly defined in App. B. Note that the nondipole Volkov state is not a pure plane wave as the $\Gamma(\mathbf{r}, t)$ depends on \mathbf{r} . Before going on, it is beneficial to discuss the individual contributions of the nondipole Volkov phase by its physical means. The respective contributions are listed in the following

$$\mathbf{p} \cdot \mathbf{A}(\mathbf{k}, t) = \lambda_{\mathbf{k}} \cos(u_{\mathbf{k}} + \theta_{\mathbf{k}}), \quad (4.5a)$$

$$\frac{1}{4} \mathbf{a}_{\mathbf{k}} \cdot \mathbf{a}_{\mathbf{k}'} = \Delta_{\mathbf{k}\mathbf{k}'}^+ \exp(i\theta_{\mathbf{k}\mathbf{k}'}^+), \quad (4.5b)$$

$$\frac{1}{4} \mathbf{a}_{\mathbf{k}} \cdot \mathbf{a}_{\mathbf{k}'}^* = \Delta_{\mathbf{k}\mathbf{k}'}^- \exp(i\theta_{\mathbf{k}\mathbf{k}'}^-), \quad (4.5c)$$

$$-\mathbf{k} \cdot \mathbf{A}_{\mathbf{k}'}(t) = \sigma_{\mathbf{k}\mathbf{k}'} \cos(u_{\mathbf{k}'} + \xi_{\mathbf{k}\mathbf{k}'}), \quad (4.5d)$$

$$\eta_{\mathbf{k}} = \mathbf{p} \cdot \mathbf{k} - \omega_{\mathbf{k}}, \quad (4.5e)$$

$$\rho_{\mathbf{k}} = \frac{\lambda_{\mathbf{k}}}{\eta_{\mathbf{k}}}, \quad (4.5f)$$

$$\alpha_{\mathbf{k}\mathbf{k}'}^{\pm} = \frac{\Delta_{\mathbf{k}\mathbf{k}'}^{\pm}}{\eta_{\mathbf{k}} \pm \eta_{\mathbf{k}'}}. \quad (4.5g)$$

A detailed discussion of the respective terms is presented below, while the mathematical notation is discussed in Ref. [112] (chap. 4) and Ref. [111].

- (a): The term $\mathbf{p} \cdot \mathbf{A}(\mathbf{k}, t)$ is directly associated with the particle-field contribution in the minimal coupling Hamiltonian (4.2), where the respective plane wave mode $\mathbf{A}(\mathbf{k}, t)$ is introduced in Def. 2.3. The dot product of these vectors is rewritten as the scalar $\lambda_{\mathbf{k}}$ with an orientation-dependent factor $\cos(u_{\mathbf{k}} + \theta_{\mathbf{k}})$. The phase $\theta_{\mathbf{k}}$ encodes the

initial orientation of both vectors, whereas spatial and temporal dependency is imprinted on $u_{\mathbf{k}} = \mathbf{k} \cdot \mathbf{r} - \omega_{\mathbf{k}}t$.

- (b,c): The field-field contribution, $\mathbf{A}^2(\mathbf{r}, t)/2$, essentially consists of four separate terms, proportional to $\mathbf{a}_{\mathbf{k}} \cdot \mathbf{a}_{\mathbf{k}'}$ and $\mathbf{a}_{\mathbf{k}} \cdot \mathbf{a}_{\mathbf{k}'}^*$ as well as their complex conjugation. These terms follow from the reformulation of the vector potential $\mathbf{A}(\mathbf{r}, t)$ by using the identity $\text{Re}[z] = (z + z^*)/2$ and replacing $z \rightarrow \mathbf{a}_{\mathbf{k}}e^{iu_{\mathbf{k}}}$; see Def. 2.3. The amplitude $\Delta_{\mathbf{k}\mathbf{k}'}^{\pm}$ and its respective phase $\theta_{\mathbf{k}\mathbf{k}'}^{\pm}$ are reformulated by the same approach as in (a), where both depend on two separate wave vectors \mathbf{k} and \mathbf{k}' . The superscript \pm denotes the composition of $\mathbf{a}_{\mathbf{k}} \cdot \mathbf{a}_{\mathbf{k}'}$ and $\mathbf{a}_{\mathbf{k}} \cdot \mathbf{a}_{\mathbf{k}'}^*$, respectively ¹.
- (d): The term $-\mathbf{k} \cdot \mathbf{A}(\mathbf{k}', t)$ significantly differs from the particle-field and field-field contribution discussed above. It may be understood as a form of field-field contribution since the single wave vector \mathbf{k} is generally associated with another additional plane wave mode. Nevertheless, the essential difference lies in the wave vector \mathbf{k} and its geometric relation to the plane wave mode $\mathbf{A}(\mathbf{k}', t)$. Where the particle-field and field-field contribution both lead to dipole and nondipole contributions, the *geometric contribution* $-\mathbf{k} \cdot \mathbf{A}(\mathbf{k}', t)$ is a purely nondipole contribution with $\mathbf{k} \propto 1/c$. Furthermore, the plane wave mode $\mathbf{A}(\mathbf{k}', t)$ is restricted to the transverse plane $\{\mathbf{e}_1, \mathbf{e}_2\}$; see Def. 2.3. Each wave vector is, by definition, perpendicular to its respective transverse plane, so that the geometric contribution vanishes for $\mathbf{e}_{\mathbf{k}} \equiv \mathbf{e}_{\mathbf{k}'}$. In other words, the geometric contribution vanishes identically for each collinear superposition of plane wave modes, while it induces finite contributions for more elaborate light fields like Gaussian, Laguerre-Gaussian, or Bessel beams.

Overall, the geometric contribution represents a weakly relativistic contribution of the nondipole Volkov state and is nonvanishing for geometrically complex vector potentials beyond the superposition of collinear plane waves.

- (e): The parameter $\eta_{\mathbf{k}}$ considers the respective nondipole contributions for arbitrary configurations of plane wave modes. Therefore, $\eta_{\mathbf{k}}$ induces nondipole effects even in trivial beam arrangements, like for plane waves. For plane-wave lasers, $\eta_{\mathbf{k}} = (\mathbf{p} \cdot \mathbf{e}_{\mathbf{k}}/c - m_e)\omega_{\mathbf{k}}$ ² can be understood as an effective momentum-dependent mass with $\eta_{\mathbf{k}} \rightarrow -\omega_{\mathbf{k}}m_e \stackrel{a.u.}{=} -\omega_{\mathbf{k}}$ in the nonrelativistic regime and $m_{eff} = m_e - \mathbf{p} \cdot \mathbf{e}_{\mathbf{k}}/c$ with $\eta_{\mathbf{k}} = -\omega_{\mathbf{k}}m_{eff}$ in the relativistic regime. More details are presented in Ref [113]. With this in mind, $\eta_{\mathbf{k}}$ is referred to as the *effective mass term* of the electron.

¹The superscripts \pm similarly hold for the complex conjugations $\mathbf{a}_{\mathbf{k}}^* \cdot \mathbf{a}_{\mathbf{k}'}$ and $\mathbf{a}_{\mathbf{k}}^* \cdot \mathbf{a}_{\mathbf{k}'}^*$, while the respective signs need to be adapted in Eqs. (4.5b) and (4.5c)

²The electron mass in atomic units reads $m_e = 1$ and is therefore usually omitted.

Taylor expanding $\eta_{\mathbf{k}}$ within the nondipole Volkov phase yields the typical dipole and nondipole contributions, known from other HHG models [93, 98].

(f,g): The factors $\rho_{\mathbf{k}}$ and $\alpha_{\mathbf{k}\mathbf{k}'}^{\pm}$ denote the effective mass corrected terms of the particle-field and field-field contribution, respectively. Mathematically, they are a direct consequence of the approximate solution of the TDSE to the first relativistic order [110]. The superscript \pm indicates the composition of the complex amplitudes $\mathbf{a}_{\mathbf{k}}$ and $\mathbf{a}_{\mathbf{k}'}^*$, as mentioned in (b,c).

In conclusion, the nondipole Volkov state consists of a set of fundamental terms that are discussed in a physical context. These terms build up the nondipole Volkov phase (B.1) and provide a physical interpretation of the individual contributions.

4.2. Strong-field transition amplitudes beyond the dipole approximation

The dipole SFA is a widely utilized approximation in strong-field physics that incorporates a few basic assumptions, listed in Def. 3.1. These assumptions extensively simplify the model and allow for analytical treatment. On the other hand, they may directly affect gauge freedom such that physical observables, for example, the atomic dipole moment, no longer necessarily fulfill gauge invariance [68]. Especially the ionization- and recombination amplitudes concerning the bound and dressed continuum state could be gauge-dependent, and thereby break gauge invariance. Fortunately, a careful treatment of the Hamiltonian and its associated time evolution operators guarantees the gauge invariance of the dipole SFA [70]. The gauge fixing procedure for transition amplitudes beyond the dipole approximation is similar to the respective dipole scenario ³. The following derivation is therefore based on the previous discussion in Sec. 3.4.2.

The standard form of the dipole SFA is formulated in length gauge where the gauge freedom allows for a vanishing vector-potential $\mathbf{A}(t) \equiv 0$. In accordance with the dipole SFA, many of the standard nondipole SFA theories [30, 93, 98] are formulated in length gauge. This choice of gauge seems to be reasonable since the scalar potential $\Phi(\mathbf{r}, t)$ in the Hamiltonian may be expanded to its first relativistic order, proportional to $\frac{|\mathbf{k}|}{\omega_{\mathbf{k}}} = \frac{1}{c}$. Here, $\mathbf{k} = |\mathbf{k}|\mathbf{e}_{\mathbf{k}}$ is the momentum vector of the respective electromagnetic potential, $\omega_{\mathbf{k}}$ its frequency, and c the speed of light. The length gauge unfortunately

³Def. 3.1(v) is not necessary anymore

not applicable if the concrete spatial structure of the respective laser field is arbitrary, which originates from the spatial dependency of the vector potential. Therefore, it is necessary to develop a corresponding theoretical framework in velocity gauge, which corresponds to the gauge condition $\Phi(\mathbf{r}, t) \equiv 0$. This dissertation follows the ideas of Klaiber et.al. [71] and others [70, 72] to provide gauge-invariant transition amplitudes for spatially structured (nondipole) laser fields. In general, it is impossible to explicitly show the gauge independence within the length and velocity gauge, as done below Eq. (3.38) within the nonrelativistic regime, since the classical length gauge does not exist for spatially structured laser fields. However, the essential argument to achieve gauge invariance links to the perturbative expansion concerning the eigenstates of the *energy operator*. A more elaborated argumentation can be found in Sec. 3.4.2.

The derivation starts from the Hamiltonian in Eq. (3.11) that describes an electron in the combined potential of an atomic core and an intense laser field. The associated TDSE is written as

$$i\hat{\partial}_t |\Psi(\mathbf{r}, t)\rangle = \left[\frac{1}{2} (\hat{\mathbf{p}} + \mathbf{A}(\mathbf{r}, t))^2 + \hat{V}(\mathbf{r}) - \Phi(\mathbf{r}, t) \right] |\Psi(\mathbf{r}, t)\rangle. \quad (4.6)$$

The Hamiltonian (3.11) separates into its respective energy operator $\hat{\mathcal{E}}$ and the scalar potential Φ via

$$\hat{\mathcal{H}} = \hat{\mathcal{E}}(\mathbf{r}, t) - \Phi(\mathbf{r}, t), \quad \hat{\mathcal{E}}(\mathbf{r}, t) = \frac{(\hat{\mathbf{p}} + \mathbf{A}(\mathbf{r}, t))^2}{2} + \hat{V}(\mathbf{r}), \quad (4.7)$$

with the electron charge $q = -1$. Here, the energy operator explicitly considers the spatial structure of the vector potential in contrast to the spatially independent energy operator in Eq. (3.25). However, the energy operator remains gauge invariant for spatially structured light fields [77] such that one can proceed further. The eigenstate of the energy operator, namely the *energy eigenstate*, is defined via

$$|\Psi_n^{\mathcal{E}}(t)\rangle = e^{-i\mathbf{r} \cdot \mathbf{A}(\mathbf{r}, t)} |\Psi_n(t)\rangle \Rightarrow \hat{\mathcal{E}}(\mathbf{r}, t) |\Psi_n^{\mathcal{E}}(t)\rangle = \epsilon_n |\Psi_n^{\mathcal{E}}(t)\rangle, \quad (4.8)$$

where ϵ_n is the eigenvalue of the field-free Hamiltonian and Ψ_n is its respective eigenstate that obeys

$$\hat{\mathcal{H}}_0 |\Psi_n(t)\rangle = \epsilon_n |\Psi_n(t)\rangle, \quad |\Psi_n(t)\rangle = e^{-i\epsilon_n t} |\Psi_n\rangle. \quad (4.9)$$

The eigenvalue equation of the energy operator (4.8) essentially holds for any vector potential that satisfies the Coulomb gauge condition $\hat{\nabla}_{\mathbf{r}} \cdot \mathbf{A}(\mathbf{r}, t) = 0$. The vector potential utilized in this chapter consists of a continuous superposition of plane waves $\mathbf{k}_i \cdot \mathbf{a}_{\mathbf{k}_i} = 0 \Leftrightarrow \mathbf{k}_i \perp \mathbf{a}_{\mathbf{k}_i}$ that individually obey the Coulomb gauge. The restriction to potentials that obey the Coulomb gauge is mandatory since the commutator $[\cdot, \cdot]$ of the momentum operator $\hat{\mathbf{p}} = -i\hat{\nabla}_{\mathbf{r}}$ and the vector potential would not vanish otherwise

$$\begin{aligned} \hat{\mathbf{p}} \cdot (\mathbf{A}(\mathbf{r}, t)\Psi) &= (\hat{\mathbf{p}} \cdot \mathbf{A}(\mathbf{r}, t))\Psi + \mathbf{A}(\mathbf{r}, t) \cdot \hat{\mathbf{p}}\Psi, \\ \hat{\mathbf{p}} \cdot (\mathbf{A}(\mathbf{r}, t)\Psi) - \mathbf{A}(\mathbf{r}, t) \cdot \hat{\mathbf{p}}\Psi &= (\hat{\mathbf{p}} \cdot \mathbf{A}(\mathbf{r}, t))\Psi, \\ \Rightarrow [\hat{\mathbf{p}}, \mathbf{A}(\mathbf{r}, t)] &= 0 \quad \text{for} \quad \hat{\mathbf{p}} \cdot \mathbf{A}(\mathbf{r}, t) = \underbrace{-i\hat{\nabla}_{\mathbf{r}} \cdot \mathbf{A}(\mathbf{r}, t)}_{=0 \text{ if Eq. (2.4)}}. \end{aligned} \quad (4.10)$$

A detailed proof of Eq. (4.8) is presented in App. A. The temporal evolution of the Coulomb wave function in Eq. (4.6) is given by

$$|\Psi(t)\rangle = \hat{\mathcal{U}}(t, t') |\Psi(t')\rangle, \quad (4.11)$$

with the Coulomb time evolution operator $\hat{\mathcal{U}}$ that is analogously defined in Eq. (3.34) as

$$\begin{aligned} \hat{\mathcal{U}}(t, t') &= \hat{\mathcal{U}}_{\mathcal{E}}(t, t') - i \int_{t'}^t d\tau \hat{\mathcal{U}}(t, \tau) \hat{\mathcal{H}}_{int}(\mathbf{r}, \tau) \hat{\mathcal{U}}_{\mathcal{E}}(\tau, t'), \\ &\approx \hat{\mathcal{U}}_{\mathcal{E}}(t, t') + i \int_{t'}^t d\tau \hat{\mathcal{U}}_{le}(t, \tau) \left(\Phi(\mathbf{r}, \tau) + \mathbf{r} \cdot \hat{\partial}_{\tau} \mathbf{A}(\mathbf{r}, \tau) \right) \hat{\mathcal{U}}_{\mathcal{E}}(\tau, t'). \end{aligned} \quad (4.12)$$

Furthermore, the temporal evolution of the continuum state is assumed to be unaffected by the binding potential $V(\mathbf{r})$, such that the laser-electron time evolution operator $\hat{\mathcal{U}}_{le}$ represents the evolution of the continuum state. These assumptions were previously applied to approximate $\hat{\mathcal{U}} \rightarrow \hat{\mathcal{U}}_{le}$ below Eq. (3.36). With this in mind, the strong-field ionization amplitude can be cast into the form ⁴

$$\begin{aligned} M_{p,0} &= \lim_{t \rightarrow \infty} \langle \Psi_{\mathbf{p}}(t) | \Psi(t) \rangle \\ &= \lim_{t \rightarrow \infty, t_0 \rightarrow -\infty} \langle \Psi_{\mathbf{p}}(t) | \hat{\mathcal{U}}(t, t_0) | \Psi_0(t_0) \rangle, \\ &= \lim_{t \rightarrow \infty, t_0 \rightarrow -\infty} -i \int_{t_0}^t d\tau \langle \Psi_{\mathbf{p}}(t) | \hat{\mathcal{U}}(t, \tau) \hat{\mathcal{H}}_{int}(\mathbf{r}, \tau) \hat{\mathcal{U}}_{\mathcal{E}}(\tau, t_0) | \Psi_0(t_0) \rangle, \\ &\approx -i \int_{-\infty}^{\infty} d\tau \langle \chi_{\mathbf{p}}^{ND}(\tau) | e^{-i\mathbf{r} \cdot \mathbf{A}(\mathbf{r}, \tau)} \hat{\mathcal{H}}_{int}(\mathbf{r}, \tau) | \Psi_0(\tau) \rangle, \\ &\stackrel{\Phi \equiv 0}{\approx} -i \int_{-\infty}^{\infty} d\tau \langle \chi_{\mathbf{p}}^{ND}(\tau) | e^{-i\mathbf{r} \cdot \mathbf{A}(\mathbf{r}, \tau)} \mathbf{r} \cdot \mathbf{E}(\mathbf{r}, \tau) | \Psi_0(\tau) \rangle. \end{aligned} \quad (4.13)$$

⁴The scalar potential vanishes in velocity gauge $\Phi(\mathbf{r}, t) \equiv 0$.

Therefore, the non-dipole ionization amplitude is identical to the dipole ionization amplitude Eq. (3.39) apart from the radial dependency of the laser field and the respective Volkov states. A mandatory restriction to this quite general statement relates to the definition of the vector potential itself. The nondipole ionization amplitude (4.13) is restricted to vector potentials that obey the Coulomb gauge $\hat{\nabla}_r \cdot \mathbf{A}(\mathbf{r}, t)$. Otherwise, the definition of the energy eigenstates would not hold and result in a gauge-dependent Dyson expansion.

4.3. Generalized nondipole strong-field approximation

It is advantageous to interpret the electron motion quasi-classically to understand the effect of spatially structured light fields on HHG. So far, HHG is usually strongly suppressed for a significant magnetic displacement within the microscopic regime. This suppression originates from an exponential decrease in the recombination probability of the electron with the respective parent ion. This probability essentially depends on the relative distance between the parent ion and the ionized electron. In the dipole approximation, the electron $\mathbf{r}(t)$ revisits the parent ion at its fixed position \mathbf{r}_0 after one optical period T_0 with $\mathbf{r}(0) = \mathbf{r}(T_0) = \mathbf{r}_0$ such that the recombination probability remains reasonably high. The Lorentz force, on the other hand, drifts the electron away from its parent ion in theories that account for the spatial structure of the laser field (nondipole theories), such that the position of the electron after one optical period reads $\mathbf{r}(T_0) = \mathbf{r}_0 + \Delta\mathbf{r}$ [93, 114–116]. The nonvanishing distance between the electron and the parent ion $\mathbf{r}(T_0) - \mathbf{r}_0 = \Delta\mathbf{r}$ is induced by the magnetic field of the incident laser and is referred to as magnetic displacement. The respective electron dynamics, including the magnetic displacement, are illustrated in Fig. 4.2b. This displacement yields an exponential decrease in the recombination probability. For an increasing magnetic displacement, the electron is consequently less likely to recombine with its parent ion, so that no HH photon is emitted. Note that this simplified interpretation is limited to a plane wave laser field. More complex beam structures may induce other effects aside from those generic to plane waves [30, 115].

Since these interpretations are limited to a qualitative understanding of the actual process, a formal derivation of the so-called generalized nondipole SFA (GN-SFA) is presented below.

The HH radiation is generally defined in terms of the atomic dipole moment (3.10)

$$\mathbf{D}(t) = q \langle \Psi(t) | \mathbf{r} | \Psi(t) \rangle, \quad (4.14)$$

with the Coulomb wave function $\Psi(t)$, which is approximated by the time evolution operator in Eq. (4.12), as

$$\begin{aligned} |\Psi(t)\rangle &= \hat{\mathcal{U}}(t, t_0) |\Psi(t_0)\rangle, \\ &\approx \hat{\mathcal{U}}_{\mathcal{E}}(t, t_0) |\Psi_0(t_0)\rangle - i \int_{t_0}^t dt' \hat{\mathcal{U}}_{le}(t, t') \hat{\mathcal{H}}_{int}(\mathbf{r}, t') \hat{\mathcal{U}}_{\mathcal{E}}(t', t_0) |\Psi_0(t_0)\rangle. \end{aligned} \quad (4.15)$$

The respective atomic dipole moment, analogously to Eq. (3.42), reads

$$\begin{aligned} \mathbf{D}(t) &\approx i \int_{-\infty}^t dt' \langle \Psi_0(t) | e^{i\mathbf{r} \cdot \mathbf{A}(\mathbf{r}, t)} \mathbf{r} \hat{\mathcal{U}}_{le}(t, t') \hat{\mathcal{H}}_{int}(\mathbf{r}, t') e^{-i\mathbf{r} \cdot \mathbf{A}(\mathbf{r}, t')} | \Psi_0(t') \rangle, \\ &= i \int_{-\infty}^t dt' \int d^3\mathbf{p} \langle \Psi_0(t) | e^{i\mathbf{r} \cdot \mathbf{A}(\mathbf{r}, t)} \mathbf{r} | \chi_{\mathbf{p}}^{ND}(t) \rangle \\ &\quad \times \langle \chi_{\mathbf{p}}^{ND}(t') | \hat{\mathcal{H}}_{int}(t') e^{-i\mathbf{r} \cdot \mathbf{A}(\mathbf{r}, t')} | \Psi_0(t') \rangle, \end{aligned} \quad (4.16)$$

where higher-order processes like continuum-continuum transitions are neglected. Furthermore, the emission time of the incident laser is chosen as $t_0 \rightarrow -\infty$, and the expansion of the laser-electron time evolution operator

$$\hat{\mathcal{U}}_{le}(t, t') = \int d^3\mathbf{p} | \chi_{\mathbf{p}}^{ND}(t) \rangle \langle \chi_{\mathbf{p}}^{ND}(t') |, \quad (4.17)$$

is utilized. Inserting the definition of the nondipole Volkov states (4.4) into Eq. (4.16) and using Eq. (4.9) yields the atomic dipole moment as

$$\begin{aligned} \mathbf{D}(t) &= i \int_{-\infty}^t d\tau \int d^3\mathbf{p} \langle \Psi_0 | \mathbf{r} e^{-i\Gamma(\mathbf{r}, t)} | \mathbf{p} + \mathbf{A}(\mathbf{r}, t) \rangle \\ &\quad \times \langle \mathbf{p} + \mathbf{A}(\mathbf{r}, \tau) | e^{i\Gamma(\mathbf{r}, \tau)} \hat{\mathcal{H}}_{int}(\tau) | \Psi_0 \rangle e^{-iI_p(t-\tau)} e^{-iE_p(t-\tau)}. \end{aligned} \quad (4.18)$$

In contrast to the dipole SFA, the nondipole Volkov states possess a nontrivial spatial structure. Therefore, the nondipole Volkov phase $\Gamma(\mathbf{r}, t)$ cannot be removed from the respective expectation value. So far, the derivation was quite similar to the one of the dipole SFA. Proceeding further requires additional effort to separate a purely time-dependent contribution of the respective Volkov phase from the temporal- and spatial-dependent contribution. The purely time-dependent contribution reduces to the quasi-classical action within the non-relativistic limit. However, the general mathematical

structure of the individual terms in the nondipole Volkov phase (B.1) remains similar to the weakly relativistic regime. The following separation technique is only demonstrated for the particle-field contribution (B.1b) of the nondipole Volkov phase, while the extension to the remaining terms is straightforward. A few more details on the extension are discussed afterward.

The particle-field contribution of the nondipole Volkov phase follows as

$$\Gamma_1(\mathbf{r}, t) = \int d^3\mathbf{k} \rho_{\mathbf{k}} \sin(u_{\mathbf{k}} + \theta_{\mathbf{k}}), \quad (4.19)$$

with the amplitude $\rho_{\mathbf{k}}$ and intrinsic phase $\theta_{\mathbf{k}}$ that are given by Eqs. (4.5a) and (4.5f). The expectation value in Eq. (4.18) is represented as a three-dimensional spatial integral. Since the particle-field contribution has an explicit spatial dependency via $u_{\mathbf{k}} = \mathbf{k} \cdot (\mathbf{r}_0 + \mathbf{r}) - \omega_{\mathbf{k}} t$, it cannot be pulled outside of the respective expectation value. The position vector \mathbf{r}_0 and \mathbf{r} denote the position of the parent ion and the relative position of the ionized electron to its parent ion, respectively. The sine function in Eq. (4.19) is reformulated by utilizing the respective trigonometric identity $\sin(x \pm y) = \sin(x) \cos(y) \pm \cos(x) \sin(y)$, such that the particle-field contribution reads

$$\begin{aligned} \Gamma_1(\mathbf{r}, t) &= \int d^3\mathbf{k} \rho_{\mathbf{k}} \left(\sin(\mathbf{k} \cdot \mathbf{r}) \cos(\mathbf{k} \cdot \mathbf{r}_0 - \omega_{\mathbf{k}} t + \theta_{\mathbf{k}}) + \cos(\mathbf{k} \cdot \mathbf{r}) \sin(\mathbf{k} \cdot \mathbf{r}_0 - \omega_{\mathbf{k}} t + \theta_{\mathbf{k}}) \right), \\ &= \int d^3\mathbf{k} \rho_{\mathbf{k}} \left(\sin(\mathbf{k} \cdot \mathbf{r}) \cos(u_{\mathbf{k}}^{(0)} + \theta_{\mathbf{k}}) + \cos(\mathbf{k} \cdot \mathbf{r}) \sin(u_{\mathbf{k}}^{(0)} + \theta_{\mathbf{k}}) \right), \end{aligned} \quad (4.20)$$

$$u_{\mathbf{k}}^{(0)} \equiv \mathbf{k} \cdot \mathbf{r}_0 - \omega_{\mathbf{k}} t. \quad (4.21)$$

Since the wave vector is inversely proportional to the speed of light $\mathbf{k} \propto 1/c$, it denotes a small perturbation, or in other words a weak relativistic perturbation. The factor $\mathbf{k} \cdot \mathbf{r}$ is consequently a weakly relativistic perturbation which allows to Taylor expand the respective trigonometric functions $\sin(\mathbf{k} \cdot \mathbf{r})$ and $\cos(\mathbf{k} \cdot \mathbf{r})$ up to the first relativistic order as

$$\sin(\mathbf{k} \cdot \mathbf{r}) \approx \underbrace{0}_{\propto 1} + \underbrace{\mathbf{k} \cdot \mathbf{r}}_{\propto 1/c} \quad \text{and} \quad \cos(\mathbf{k} \cdot \mathbf{r}) \approx \underbrace{1}_{\propto 1} + \underbrace{0}_{\propto 1/c}. \quad (4.22)$$

Expanding the exact nondipole Volkov phase $\Gamma(\mathbf{r}, t)$ [112] reveals nondipole contributions $\Gamma_i \in i = \{3, 4, 5\}$ which are unique to the exact nondipole Volkov phase [111, 112]. These contributions are not included in similar models that utilize a nondipole Volkov phase which is approximated in the very beginning. However, the particle-field contribution is

then approximated by

$$\begin{aligned}
\Gamma_1(\mathbf{r}, t) &\approx \int d^3\mathbf{k} \rho_{\mathbf{k}} \left(\mathbf{k} \cdot \mathbf{r} \cos(u_{\mathbf{k}}^{(0)} + \theta_{\mathbf{k}}) + \sin(u_{\mathbf{k}}^{(0)} + \theta_{\mathbf{k}}) \right), \\
&= \mathbf{r} \cdot \int d^3\mathbf{k} \mathbf{k} \rho_{\mathbf{k}} \cos(u_{\mathbf{k}}^{(0)} + \theta_{\mathbf{k}}) + \int d^3\mathbf{k} \rho_{\mathbf{k}} \sin(u_{\mathbf{k}}^{(0)} + \theta_{\mathbf{k}}), \\
&= \mathbf{r} \cdot \mathbf{\Gamma}_1^{(r)}(t) + \Gamma_1^{(t)}(t).
\end{aligned} \tag{4.23}$$

Each term in the nondipole Volkov phase Γ_i is proportional to the general form of the integrand $\sin(\tilde{u} + \tilde{\theta})$ with $\tilde{u} = \sum_i g_i u_{\mathbf{k}_i}$ being the sum of separate plane wave phases and $\tilde{\theta}$ is the respective cumulated intrinsic phase. This can be seen in App. B.1 where the arguments x of the respective $\sin(x)$ terms may be rewritten as described. In addition, g_i defines the sign of the i -th plane-wave phase $u_{\mathbf{k}_i}$. The sum of the respective plane-wave phases is summarized to $\tilde{u} = \tilde{\mathbf{k}} \cdot (\mathbf{r}_0 + \mathbf{r}) - \tilde{\omega}t$, where $\tilde{\mathbf{k}}$ and $\tilde{\omega}$ represent the sum of the plane wave momenta and frequencies, respectively. With this definition in mind, the respective general form of the integrand is given via

$$\begin{aligned}
\sin(\tilde{u} + \tilde{\theta}) &= \sin\left((\mathbf{r}_0 + \mathbf{r}) \cdot \tilde{\mathbf{k}} - t\tilde{\omega} + \tilde{\theta}\right), \\
&= \sin(\mathbf{r} \cdot \tilde{\mathbf{k}}) \cos(\tilde{u}^{(0)} + \tilde{\theta}) + \cos(\mathbf{r} \cdot \tilde{\mathbf{k}}) \sin(\tilde{u}^{(0)} + \tilde{\theta}), \\
&\approx \mathbf{r} \cdot \tilde{\mathbf{k}} \cos(\tilde{u}^{(0)} + \tilde{\theta}) - \sin(\tilde{u}^{(0)} + \tilde{\theta}),
\end{aligned} \tag{4.24}$$

which demonstrates that each term in the non-dipole Volkov phase can be decomposed into a radial $\mathbf{\Gamma}_i^{(r)}$ and a temporal contribution $\Gamma_i^{(t)}$ of the nondipole Volkov phase. Therefore, the full nondipole Volkov phase (B.1) is approximated as

$$\begin{aligned}
\Gamma(\mathbf{r}, t) &\approx \mathbf{r} \cdot \sum_{i=1}^5 \mathbf{\Gamma}_i^{(r)}(t) + \sum_{i=1}^5 \Gamma_i^{(t)}(t), \\
&= \mathbf{r} \cdot \mathbf{\Gamma}^{(r)}(t) + \Gamma^{(t)}(t),
\end{aligned} \tag{4.25}$$

with the *spatial nondipole Volkov phase* $\mathbf{\Gamma}^{(r)}(t) \equiv \mathbf{\Gamma}^{(r)}(\mathbf{r}_0, t)$, see Eq. (B.2), and the *temporal nondipole Volkov phase* $\Gamma^{(t)}(t) \equiv \Gamma^{(t)}(\mathbf{r}_0, t)$, see Eq. (B.3). Here, the use of Eq. (4.25) allows us to represent $\exp(i\mathbf{r} \cdot \mathbf{\Gamma}^{(r)}(t))$ as a plane wave, which is essential for further analytical treatment. Inserting Eq. (4.25) into Eq. (4.18) yields

$$\begin{aligned}
\mathbf{D}(t) &= i \int_{-\infty}^t dt' \int d^3\mathbf{p} \langle \Psi_0 | \mathbf{r} | \mathbf{p} + \mathbf{A}(\mathbf{r}, t) - \mathbf{\Gamma}^{(r)}(t) \rangle \langle \mathbf{p} + \mathbf{A}(\mathbf{r}, t') - \mathbf{\Gamma}^{(r)}(t') | \hat{\mathcal{H}}_{int}(t') | \Psi_0 \rangle \\
&\quad \times e^{-i\Gamma^{(t)}(t)} e^{i\Gamma^{(t)}(t')} e^{-iE_{\mathbf{p}}(t-t')} e^{-iI_{\mathbf{p}}(t-t')}, \\
&= i \int_{-\infty}^t dt' \int d^3\mathbf{p} \langle \Psi_0 | \mathbf{r} | \boldsymbol{\pi}(\mathbf{p}, \mathbf{r}, t) \rangle \langle \boldsymbol{\pi}(\mathbf{p}, \mathbf{r}, t') | \hat{\mathcal{H}}_{int}(t') | \Psi_0 \rangle e^{-iS(\mathbf{p}, t, t')},
\end{aligned} \tag{4.26}$$

with the replacement $\tau \rightarrow t'$ and the momentum $\boldsymbol{\pi}(\mathbf{p}, \mathbf{r}, t) = \mathbf{p} + \mathbf{A}(\mathbf{r}, t) - \boldsymbol{\Gamma}^{(r)}(t)$. The state $|\boldsymbol{\pi}(\mathbf{p}, \mathbf{r}, t)\rangle$ is again no pure plane wave state as $\boldsymbol{\pi}$ depends on \mathbf{r} , similar to Eq. 4.4. However, the quasi-classical action finally reads

$$S(\mathbf{p}, t, t') = \int_{t'}^t d\tau \left(E_p + \hat{\partial}_\tau \Gamma^{(t)}(\tau) + I_p \right). \quad (4.27)$$

4.3.1. Nondipole matrix element

The momentum $\boldsymbol{\pi}(\mathbf{p}, \mathbf{r}, t)$ in the matrix elements of Eq. (4.26) possesses a nontrivial radial structure, such that the matrix element does not coincide with the dipole matrix element. However, an analytic solution can be derived while focusing on hydrogen-like atoms. The derivation is demonstrated and discussed in the following.

Let the *nondipole matrix element* for hydrogen-like atoms be defined as

$$\begin{aligned} \Upsilon(\mathbf{p}, t) &= \langle \boldsymbol{\pi}(\mathbf{p}, \mathbf{r}, t) | \mathbf{r} | \Psi_0 \rangle \\ &= \left(\frac{I_p}{2} \right)^{3/4} \frac{1}{\pi^2} \int d^3 \mathbf{r} e^{-i\mathbf{r} \cdot [\mathbf{p} + \mathbf{A}(\mathbf{r}, t) - \boldsymbol{\Gamma}^{(r)}(t)]} \mathbf{r} e^{-|r| \sqrt{2I_p}}, \end{aligned} \quad (4.28)$$

with the ground state wave function $|\Psi_0\rangle$ and the continuum state $\langle \boldsymbol{\pi}(\mathbf{p}, \mathbf{r}, t) | \mathbf{r} \rangle = e^{-i\mathbf{r} \cdot (\mathbf{p} + \mathbf{A}(\mathbf{r}, t) - \boldsymbol{\Gamma}^{(r)}(t))}$ defined in Def. 3.3. In the dipole and nondipole SFA, the respective matrix elements describe the transitions of an electron between a bound and a continuum state in the *microscopic regime*. In the microscopic regime, the dipole vector potential (Def. 2.3) is approximately constant in the vicinity of the target atom and reads

$$\begin{aligned} \mathbf{A}(t) &\equiv \mathbf{A}(\mathbf{r}_0, t) = \int d^3 \mathbf{k} \operatorname{Re} \left[\mathbf{a}_{\mathbf{k}} e^{i(\mathbf{k} \cdot \mathbf{r}_0 - \omega_{\mathbf{k}} t)} \right], \\ &= \sum_j \int d^3 \mathbf{k} \operatorname{Re} \left[\tilde{\mathbf{a}}_{\mathbf{k}_j} \boldsymbol{\delta}(\mathbf{k} - \mathbf{k}_j) e^{i(\mathbf{k} \cdot \mathbf{r}_0 - \omega_{\mathbf{k}} t)} \right], \\ &= \sum_j \mathbf{A}_{\mathbf{k}_j}(t), \end{aligned} \quad (4.29)$$

with *locally fixed wave vectors* \mathbf{k}_j that depend on the *global position* \mathbf{r}_0 of the atom and the number of superimposed laser fields (indicated by the summation). The continuum electron is localized at the position $\mathbf{r} + \mathbf{r}_0$. The vector potential at the respective position of the electron is then given by $\mathbf{A}(\mathbf{r}_0 + \mathbf{r}, t)$. Although the relative position of the electron is neglected in the dipole approximation, with $\mathbf{r} \equiv 0 \Leftrightarrow \mathbf{k}_j \cdot \mathbf{r} = 0$, it is considered in

nondipole theories. In these nondipole theories, the vector potential at the electron's position is represented via

$$\mathbf{A}(\mathbf{r}, t) = \mathbf{A}(\mathbf{r}_0 + \mathbf{r}, t) = \sum_j \mathbf{A}_{\tilde{\mathbf{k}}_j}(\mathbf{r}_0 + \mathbf{r}, t), \quad (4.30)$$

where $\tilde{\mathbf{k}}_j$ denotes the wave vector at the position $\mathbf{r}_0 + \mathbf{r}$. Since the distance between the electron and the parent ion is assumed to be small $|\mathbf{r}| \ll 1$, the respective wave vectors obey $|\tilde{\mathbf{k}}_j - \mathbf{k}_j| = \Delta\mathbf{k}_j \approx 0$. Finite wave vector differences $\Delta\mathbf{k}_j \neq 0$ are associated with higher-order corrections and are consequently omitted. However, since both wave vectors coincide with good agreement, the vector potential in Eq. (4.30) is approximated as

$$\begin{aligned} \mathbf{A}(\mathbf{r}_0 + \mathbf{r}, t) &= \sum_j \int d^3\mathbf{k} \operatorname{Re} \left[\tilde{\mathbf{a}}_{\mathbf{k}_j} \delta(\mathbf{k} - \tilde{\mathbf{k}}_j) e^{i(\mathbf{k} \cdot \mathbf{r}_0 - \omega_{\mathbf{k}} t)} e^{i\mathbf{k} \cdot \mathbf{r}} \right], \\ &\approx \sum_j \int d^3\mathbf{k} \operatorname{Re} \left[\tilde{\mathbf{a}}_{\mathbf{k}_j} \delta(\mathbf{k} - \mathbf{k}_j) e^{i(\mathbf{k} \cdot \mathbf{r}_0 - \omega_{\mathbf{k}} t)} (1 + i\mathbf{k} \cdot \mathbf{r}) \right], \\ \Rightarrow \mathbf{A}(\mathbf{r}, t) &\approx \mathbf{A}(t) - \sum_j (\mathbf{k}_j \cdot \mathbf{r}) \mathbf{A}_{\mathbf{k}_j}^I(t), \end{aligned} \quad (4.31)$$

with the imaginary and real parts of the complex vector potential $\mathbf{A}_{\mathbf{k}_j}^I(t)$ and $\mathbf{A}_{\mathbf{k}_j}^R(t) \equiv \mathbf{A}_{\mathbf{k}_j}(t)$, respectively. Inserting the approximate vector potential (4.31) into Eq. (4.28) results in

$$\begin{aligned} \Upsilon(\mathbf{p}, t) &\approx \left(\frac{I_p}{2}\right)^{3/4} \frac{1}{\pi^2} \int d^3\mathbf{r} e^{-i\mathbf{r} \cdot [\boldsymbol{\pi}(\mathbf{p}, t) - \sum_j (\mathbf{k}_j \cdot \mathbf{r}) \mathbf{A}_{\mathbf{k}_j}^I(t)]} \mathbf{r} e^{-|r| \sqrt{2I_p}}, \\ &\approx \left(\frac{I_p}{2}\right)^{3/4} \frac{1}{\pi^2} \int d^3\mathbf{r} e^{-i\mathbf{r} \cdot \boldsymbol{\pi}(\mathbf{p}, t)} \mathbf{r} e^{-|r| \sqrt{2I_p}} \left[1 + \sum_j (\mathbf{k}_j \cdot \mathbf{r}) (\mathbf{r} \cdot \mathbf{A}_{\mathbf{k}_j}^I(t)) \right], \end{aligned} \quad (4.32)$$

$$\mathbf{d}(\boldsymbol{\pi}(\mathbf{p}, t)) = \left(\frac{I_p}{2}\right)^{3/4} \frac{1}{\pi^2} \int d^3\mathbf{r} e^{-i\mathbf{r} \cdot \boldsymbol{\pi}(\mathbf{p}, t)} \mathbf{r} e^{-|r| \sqrt{2I_p}}, \quad (4.33)$$

$$\boldsymbol{\pi}(\mathbf{p}, t) = \mathbf{p} + \mathbf{A}(t) - \boldsymbol{\Gamma}^{(r)}(t), \quad (4.34)$$

with the dipole matrix element $\mathbf{d}(\boldsymbol{\pi})$, introduced in Def. 3.3. The physical implications of the momentum $\boldsymbol{\pi}$ are mentioned and discussed in Sec. 4.3.2. The second term in Eq. (4.32) is calculated by introducing the dummy variables β and γ , while utilizing the

fundamental theorem of calculus

$$\begin{aligned}
I &= \left(\frac{I_p}{2}\right)^{3/4} \frac{1}{\pi^2} \int d^3\mathbf{r} e^{-ir \cdot \boldsymbol{\pi}(\mathbf{p}, t)} \mathbf{r} e^{-|r| \sqrt{2I_p}} \sum_j (\mathbf{k}_j \cdot \mathbf{r}) \left(\mathbf{r} \cdot \mathbf{A}_{\mathbf{k}_j}^I(t)\right), \\
&= \sum_j \left(\frac{I_p}{2}\right)^{3/4} \frac{\hat{\partial}_\beta \hat{\partial}_\gamma}{\pi^2} \int d^3\mathbf{r} e^{-ir \cdot \boldsymbol{\pi}(\mathbf{p}, t)} \mathbf{r} e^{-|r| \sqrt{2I_p}} e^{-ir \cdot \mathbf{k}_j \beta} e^{-ir \cdot \mathbf{A}_{\mathbf{k}_j}^I(t) \gamma} \Big|_{\beta=\gamma=0}, \\
&= \sum_j \hat{\partial}_\beta \hat{\partial}_\gamma \left(\frac{I_p}{2}\right)^{3/4} \frac{1}{\pi^2} \int d^3\mathbf{r} e^{-ir \cdot \boldsymbol{\pi}_{\beta\gamma}^j(\mathbf{p}, t)} \mathbf{r} e^{-|r| \sqrt{2I_p}} \Big|_{\beta=\gamma=0}, \\
\stackrel{\text{Def. 3.3}}{\Rightarrow} I &= \sum_j \hat{\partial}_\beta \hat{\partial}_\gamma \mathbf{d}(\boldsymbol{\pi}_{\beta\gamma}^j(\mathbf{p}, t)) \Big|_{\beta=\gamma=0}, \tag{4.35}
\end{aligned}$$

with $\boldsymbol{\pi}_{\beta\gamma}^j(\mathbf{p}, t) \equiv \mathbf{p} + \mathbf{A}(t) - \boldsymbol{\Gamma}^{(r)}(t) + \beta \mathbf{k}_j + \gamma \mathbf{A}_{\mathbf{k}_j}^I(t)$. The dummy variables β and γ do not relate to any physical quantity but are utilized to proceed with a compact analytical solution. Finally, the nondipole matrix element for hydrogen-like atoms reads

$$\boldsymbol{\Upsilon}(\mathbf{p}, t) = \mathbf{d}(\boldsymbol{\pi}(\mathbf{p}, t)) + \sum_j \hat{\partial}_\beta \hat{\partial}_\gamma \mathbf{d}(\boldsymbol{\pi}_{\beta\gamma}^j(\mathbf{p}, t)) \Big|_{\beta=\gamma=0} + \mathcal{O}(1/c^2). \tag{4.36}$$

The explicit form is shown in App. C.1. However, the hermitian conjugation of the nondipole matrix element is directly related to the recombination process in Eq. (4.26) with

$$\boldsymbol{\Upsilon}^\dagger(\mathbf{p}, t) \equiv \langle \Psi_0 | \mathbf{r} | \boldsymbol{\pi}(\mathbf{p}, \mathbf{r}, t) \rangle. \tag{4.37}$$

Inserting the interaction Hamiltonian $\hat{\mathcal{H}}_{int} = \mathbf{r} \cdot \mathbf{E}(\mathbf{r}, t)$ into Eq. (4.26) results in the ionization matrix element

$$\langle \boldsymbol{\pi}(\mathbf{p}, \mathbf{r}, t') | \hat{\mathcal{H}}_{int}(t') | \Psi_0 \rangle = \langle \boldsymbol{\pi}(\mathbf{p}, \mathbf{r}, t') | \mathbf{r} \cdot \mathbf{E}(\mathbf{r}, t') | \Psi_0 \rangle, \tag{4.38}$$

in which the radial structure of the electric field induces complications. Due to this radial dependency, the electric field cannot be removed from the expectation value in contrast to the dipole regime. Some additional effort is required to yield a proper analytical result. The electric field, in terms of the vector potential, is defined as $\mathbf{E}(\mathbf{r}, t) = -\hat{\partial}_t \mathbf{A}(\mathbf{r}, t)$ and

can be approximated via Eq. (4.31) by

$$\begin{aligned}\mathbf{E}(\mathbf{r}, t) &\approx -\hat{\partial}_t \left(\mathbf{A}(t) - \sum_j (\mathbf{k}_j \cdot \mathbf{r}) \mathbf{A}_{\mathbf{k}_j}^I(t) \right), \\ &= \mathbf{E}(t) - \sum_j (\mathbf{k}_j \cdot \mathbf{r}) \mathbf{E}_{\mathbf{k}_j}^I(t),\end{aligned}\quad (4.39)$$

with the imaginary part of the complex electric field $\mathbf{E}_{\mathbf{k}_j}^I(t)$ in the dipole regime. Inserting the approximate electric field into Eq. (4.38) yields

$$\begin{aligned}\langle \boldsymbol{\pi}(\mathbf{p}, \mathbf{r}, t') | \hat{\mathcal{H}}_{int}(t') | \Psi_0 \rangle &\approx \langle \boldsymbol{\pi}(\mathbf{p}, \mathbf{r}, t') | \mathbf{r} \cdot \left(\mathbf{E}(t) - \sum_j (\mathbf{k}_j \cdot \mathbf{r}) \mathbf{E}_{\mathbf{k}_j}^I(t) \right) | \Psi_0 \rangle, \\ &= \mathbf{E}(t) \boldsymbol{\Upsilon}(\mathbf{p}, t) - \sum_j \mathbf{E}_{\mathbf{k}_j}^I(t) \cdot \langle \boldsymbol{\pi}(\mathbf{p}, \mathbf{r}, t') | \mathbf{r} \cdot (\mathbf{k}_j \cdot \mathbf{r}) | \Psi_0 \rangle.\end{aligned}\quad (4.40)$$

For now, the focus lies on the second term, which is identified as a relativistic correction of the first order since $\mathbf{k}_j \propto 1/c$. The respective nondipole corrections of the Volkov states are here associated with higher-order corrections and are consequently neglected. The second term of Eq. (4.40) then follows as

$$\begin{aligned}\langle \boldsymbol{\pi}(\mathbf{p}, \mathbf{r}, t') | \mathbf{r} \cdot (\mathbf{k}_j \cdot \mathbf{r}) | \Psi_0 \rangle &\approx \left(\frac{I_p}{2} \right)^{3/4} \frac{1}{\pi^2} \int d^3\mathbf{r} e^{-i\mathbf{r} \cdot \boldsymbol{\pi}(\mathbf{p}, t)} \mathbf{r} e^{-|r| \sqrt{2I_p}} (\mathbf{r} \cdot \mathbf{k}_j), \\ &= i \hat{\partial}_\beta \mathbf{d} \left(\boldsymbol{\pi}(\mathbf{p}, t) + \beta \mathbf{k}_j \right) \Big|_{\beta=0}, \\ &= i \hat{\partial}_\beta \mathbf{d} \left(\boldsymbol{\pi}_{\beta\gamma}^j(\mathbf{p}, t) \right) \Big|_{\beta=\gamma=0}.\end{aligned}\quad (4.41)$$

The ionization matrix element (4.40) is then cast into the form

$$\langle \boldsymbol{\pi}(\mathbf{p}, \mathbf{r}, t') | \hat{\mathcal{H}}_{int}(t') | \Psi_0 \rangle \approx \mathbf{E}(t') \boldsymbol{\Upsilon}(\mathbf{p}, t') - \Lambda(\mathbf{p}, t'), \quad (4.42)$$

$$\Lambda(\mathbf{p}, t') = \sum_j \mathbf{E}_{\mathbf{k}_j}^I(t) \cdot i \hat{\partial}_\beta \mathbf{d} \left(\boldsymbol{\pi}_{\beta\gamma}^j(\mathbf{p}, t') \right) \Big|_{\beta=\gamma=0}. \quad (4.43)$$

With the respective transition matrix elements (4.37) and (4.42), the atomic dipole momentum (4.26) for a hydrogen-like ground state finally reduces to

$$\mathbf{D}(t) = i \int_{-\infty}^t dt' \int d^3\mathbf{p} \boldsymbol{\Upsilon}^\dagger(\mathbf{p}, t) \left(\mathbf{E}(t') \cdot \boldsymbol{\Upsilon}(\mathbf{p}, t') - \Lambda(\mathbf{p}, t') \right) e^{-iS(\mathbf{p}, t, t')}. \quad (4.44)$$

This formulation of the atomic dipole moment is close to Eq. (3.44) and can be interpreted similarly. The additional term Λ may provide deviations from the dipole SFA for particular beam alignments (e.g. noncollinear beam alignments). However, this term

is neglected as a higher-order correction in many scenarios. Overall, Λ is associated with the spatial structure of the electric field in the interaction Hamiltonian and, therefore, constitutes a relativistic correction.

4.3.2. Saddle-point approximation

The momentum integration in Eq. (4.44) is numerically costly and is therefore approximated by the saddle-point approximation (SPA); see Def. 3.4. The SPA is commonly applied to compute integrals with rapidly oscillating integrands. As discussed in Sec. 3.4.3, the SPA approximates the three-dimensional momentum integral reasonably well in the dipole regime. Moreover, its accuracy increases in the nondipole regime, which originates from a larger electron energy compared to the dipole regime. The enhanced electron energy technically results in an even faster oscillation of the phase factor $\exp(i\mathbf{p}^2)$ that overall improves the accuracy of the SPA. The saddle-point condition of Eq. (4.44) reads

$$\hat{\nabla}_{\mathbf{p}} S(\mathbf{p}, t, t') \equiv \mathbf{0} = \hat{\nabla}_{\mathbf{p}} \int_{t'}^t d\tau \left(E_{\mathbf{p}} + \hat{\partial}_{\tau} \Gamma^{(t)}(\tau) + I_{\mathbf{p}} \right). \quad (4.45)$$

It is advantageous to discuss the specific form of $\Gamma^{(t)}(\tau)$ in advance to simplify further investigations. The temporal nondipole Volkov phase consists of five separate terms with a similar mathematical structure. Two of these terms in Eqs. (B.1b) and (B.1d), explicitly depend on $\rho_{\mathbf{k}}$ (4.5f) and are associated with the canonical momentum \mathbf{p} . To simplify Eq. (4.45) it is beneficial to reformulate these terms before proceeding. The first term of the temporal nondipole Volkov phase reads

$$\Gamma_1^{(t)}(t) = \int d^3\mathbf{k} \rho_{\mathbf{k}} \sin(u_{\mathbf{k}}^{(0)} + \theta_{\mathbf{k}}) = \mathbf{p} \cdot \int d^3\mathbf{k} \frac{1}{\eta_{\mathbf{k}}} \mathcal{A}^I(\mathbf{k}, t), \quad (4.46)$$

where the superscripts R and I indicate the real and imaginary parts of the plane wave mode $\mathcal{A}(\mathbf{k}, t)$. In analogy to Eq. (4.5), the following relations hold

$$\mathbf{p} \cdot \mathcal{A}^R(\mathbf{k}, t) = \lambda_{\mathbf{k}} \cos(u_{\mathbf{k}}^{(0)} + \theta_{\mathbf{k}}) \quad \text{with} \quad \mathcal{A}^R(\mathbf{k}, t) \equiv \text{Re} \left[\mathbf{a}_{\mathbf{k}} e^{iu_{\mathbf{k}}^{(0)}} \right], \quad (4.47)$$

while the real and imaginary parts of the respective plane wave modes are related via

$$\begin{aligned} \mathcal{A}^I(\mathbf{k}, t) &= \frac{1}{\omega_{\mathbf{k}}} \hat{\partial}_t \mathcal{A}^R(\mathbf{k}, t), & \mathcal{A}^R(\mathbf{k}, t) &= -\frac{1}{\omega_{\mathbf{k}}} \hat{\partial}_t \mathcal{A}^I(\mathbf{k}, t), \\ \Rightarrow \mathbf{p} \cdot \mathcal{A}^I(\mathbf{k}, t) &= \lambda_{\mathbf{k}} \sin(u_{\mathbf{k}}^{(0)} + \theta_{\mathbf{k}}), & \mathbf{k} \cdot \mathcal{A}^I(\mathbf{k}', t) &= \sigma_{\mathbf{k}\mathbf{k}'} \sin(u_{\mathbf{k}'}^{(0)} + \zeta_{\mathbf{k}\mathbf{k}'}). \end{aligned} \quad (4.48)$$

The second term of the temporal nondipole Volkov phase follows as

$$\Gamma_3^{(t)}(t) = \sum_{\pm} \frac{1}{2} \int d^3\mathbf{k} d^3\mathbf{k}' \frac{\sigma_{\mathbf{k}\mathbf{k}'\rho\mathbf{k}}}{\eta_{\mathbf{k}} \pm \eta_{\mathbf{k}'}} \sin(u_{\mathbf{k}}^{(0)} \pm u_{\mathbf{k}'}^{(0)} + \theta_{\mathbf{k}} \pm \zeta_{\mathbf{k}\mathbf{k}'}), \quad (4.49)$$

and can be recasted by Eqs. (4.5) and (4.48) to

$$\begin{aligned} \Gamma_3^{(t)}(t) &= \mathbf{p} \cdot \mathbf{\Gamma}_3^{(p)}(t), \\ &= \mathbf{p} \cdot \int d^3\mathbf{k} d^3\mathbf{k}' \frac{\mathcal{A}^R(\mathbf{k}, t) (\mathbf{k} \cdot \mathcal{A}^I(\mathbf{k}', t)) \eta_{\mathbf{k}'} - \mathcal{A}^I(\mathbf{k}, t) (\mathbf{k} \cdot \mathcal{A}^R(\mathbf{k}', t)) \eta_{\mathbf{k}}}{\eta_{\mathbf{k}} (\eta_{\mathbf{k}}^2 - \eta_{\mathbf{k}'}^2)}, \end{aligned} \quad (4.50)$$

such that one defines

$$\begin{aligned} \mathbf{\Gamma}^{(p)}(t) &= \mathbf{\Gamma}_1^{(p)}(t) + \mathbf{\Gamma}_3^{(p)}(t), \quad (4.51) \\ &= \int d^3\mathbf{k} \frac{\mathcal{A}^I(\mathbf{k}, t)}{\eta_{\mathbf{k}}} + \int d^3\mathbf{k} d^3\mathbf{k}' \frac{\mathcal{A}^R(\mathbf{k}, t) (\mathbf{k} \cdot \mathcal{A}^I(\mathbf{k}', t)) \eta_{\mathbf{k}'} - \mathcal{A}^I(\mathbf{k}, t) (\mathbf{k} \cdot \mathcal{A}^R(\mathbf{k}', t)) \eta_{\mathbf{k}}}{\eta_{\mathbf{k}} (\eta_{\mathbf{k}}^2 - \eta_{\mathbf{k}'}^2)}. \end{aligned}$$

The temporal contribution of the Volkov phase is reformulated by the restructured terms via

$$\Gamma^{(t)}(t) = \sum_{i=1}^5 \Gamma_i^{(t)}(t) = \mathbf{p} \cdot \mathbf{\Gamma}^{(p)}(t) + \Gamma^{(A)}(t), \quad (4.52)$$

where the particle-field contributions $\Gamma_1^{(t)}(t)$ and $\Gamma_3^{(t)}(t)$ are represented by $\mathbf{p} \cdot \mathbf{\Gamma}^{(p)}(t)$ while the remaining field-field contributions sum up as $\Gamma^{(A)}(t) \equiv \Gamma_2^{(t)}(t) + \Gamma_4^{(t)}(t) + \Gamma_5^{(t)}(t)$. With Eq. (4.52) the SPA condition (4.45) consequently becomes

$$\begin{aligned} 0 &= \hat{\partial}_{p_i} \int_{t'}^t d\tau \left[E_{\mathbf{p}} + \hat{\partial}_{\tau} (\mathbf{p} \cdot \mathbf{\Gamma}^{(p)}(\tau) + \Gamma^{(A)}(\tau)) + I_{\mathbf{p}} \right], \\ 0 &= \int_{t'}^t d\tau p_i + \hat{\partial}_{\tau} \left[\mathbf{e}_i \cdot \mathbf{\Gamma}^{(p)}(\tau) + \mathbf{p} \cdot (\hat{\partial}_{p_i} \mathbf{\Gamma}^{(p)}(\tau)) + \hat{\partial}_{p_i} \Gamma^{(A)}(\tau) \right], \\ \Rightarrow \mathbf{0} &= \int_{t'}^t d\tau \left(\mathbf{1} + \hat{\partial}_{\tau} \hat{\nabla}_{\mathbf{p}} \mathbf{\Gamma}^{(p)}(\tau) \right) \cdot \mathbf{p} + \hat{\partial}_{\tau} \mathbf{\Gamma}^{(p)}(\tau) + \hat{\partial}_{\tau} \hat{\nabla}_{\mathbf{p}} \Gamma^{(A)}(\tau), \end{aligned} \quad (4.53)$$

where $\hat{\nabla}_{\mathbf{p}} \mathbf{\Gamma}^{(p)}(\tau)$ represents a matrix with the ji -th entry defined by $\hat{\partial}_{p_i} \mathbf{\Gamma}_j^{(p)}(\tau)$. Although the remaining terms $\hat{\nabla}_{\mathbf{p}} \mathbf{\Gamma}^{(p)}(\tau)$ and $\hat{\nabla}_{\mathbf{p}} \Gamma^{(A)}(\tau)$ are derived quite easily, the explicit computation is tedious and extensive. However, many terms are associated with higher-order corrections and are later neglected anyway. The general procedure is therefore only demonstrated for Eq. (4.46), whereas the residual terms can be calculated similarly. The momentum dependence of the contributions $\hat{\nabla}_{\mathbf{p}} \mathbf{\Gamma}^{(p)}(\tau)$ and $\hat{\nabla}_{\mathbf{p}} \Gamma^{(A)}(\tau)$ is associated with

the prefactors of their individual terms, which essentially depend on the effective mass term $\eta_{\mathbf{k}} = \mathbf{k} \cdot \mathbf{p} - \omega_{\mathbf{k}}$.

The derivative of the respective particle-field contribution in Eq. (4.46) reads

$$\begin{aligned} \hat{\partial}_{p_i} \Gamma_1^{(p)}(t) &= \int d^3 \mathbf{k} \hat{\partial}_{p_i} \frac{\mathcal{A}^I(\mathbf{k}, t)}{\eta_{\mathbf{k}}}, & \hat{\partial}_{p_i} \eta_{\mathbf{k}}^{-1} &= -\frac{k_i}{\eta_{\mathbf{k}}^2}, \\ \Rightarrow \hat{\partial}_{p_i} \Gamma_1^{(p)}(t) &= - \int d^3 \mathbf{k} \frac{k_i}{\eta_{\mathbf{k}}^2} \mathcal{A}^I(\mathbf{k}, t). \end{aligned} \quad (4.54)$$

Generally, the momentum dependency of the effective mass term $\eta_{\mathbf{k}}$ identifies the whole term as a relativistic correction with $k_i = k \mathbf{e}_i \propto 1/c$. In fact, each nonvanishing contribution of $\hat{\nabla}_{\mathbf{p}} \Gamma^{(p)}(\tau)$ and $\hat{\nabla}_{\mathbf{p}} \Gamma^{(A)}(t)$ represents a finite relativistic perturbation of the continuum electron.

Unfortunately, Eq. (4.53) cannot be solved exactly but approximately within an iterative approach since the effective mass term $\eta_{\mathbf{k}}$ linearly depends on the canonical momentum \mathbf{p} . The partial derivative of Eq. (4.45) is consequently non-trivial. However, to solve Eq. (4.53) the canonical momentum is represented as a sum of the relativistic corrections $\mathbf{p} = \sum_{i=0}^{\infty} \mathbf{p}_i$, where the i -th correction obeys $\mathbf{p}_i \propto c^{-i}$. At first, the nonrelativistic solution is obtained by approximating the effective mass term by $\eta_{\mathbf{k}} \approx -\omega_{\mathbf{k}}$. Inserting Eq. (4.51) into (4.53), and making use of Eq. (4.48) yields the nonrelativistic saddle-point condition

$$\begin{aligned} \mathbf{0} &= \int_{t'}^t d\tau \underbrace{\mathbf{p}_0 + \hat{\partial}_{\tau} \Gamma_1^{(p)}(\tau)}_{\propto 1} + \underbrace{\mathbf{p}_1 + \mathbf{p} \cdot \hat{\partial}_{\tau} \hat{\nabla}_{\mathbf{p}} \Gamma^{(p)}(\tau) + \hat{\partial}_{\tau} \hat{\nabla}_{\mathbf{p}} \Gamma^{(A)}(\tau) + \hat{\partial}_{\tau} \Gamma_3^{(p)}(\tau)}_{\ll 1}, \\ &\approx \int_{t'}^t d\tau \left(\mathbf{p}_0 + \int d^3 \mathbf{k} \frac{\hat{\partial}_{\tau} \mathcal{A}^I(\mathbf{k}, \tau)}{\eta_{\mathbf{k}}} \right) \approx \int_{t'}^t d\tau \left(\mathbf{p}_0 + \underbrace{\int d^3 \mathbf{k} \mathcal{A}^R(\mathbf{k}, \tau)}_{\mathbf{A}(\tau)} \right), \\ \Rightarrow \mathbf{p}_0 &= -\frac{1}{t-t'} \int_{t'}^t d\tau \mathbf{A}(\tau), \end{aligned} \quad (4.55)$$

and the associated nonrelativistic saddle-point momentum \mathbf{p}_0 . The first relativistic correction \mathbf{p}_1 is obtained by repeated application of this procedure, while relativistic corrections of order two and higher are neglected. The effective mass term is therefore approximated by $\eta_{\mathbf{k}} = \mathbf{k} \cdot (\sum_i \mathbf{p}_i) - \omega_{\mathbf{k}} \approx \mathbf{k} \cdot \mathbf{p}_0 - \omega_{\mathbf{k}}$ to the first relativistic order. The

saddle-point condition then follows by

$$\begin{aligned} \mathbf{0} &= \int_{t'}^t d\tau \left(\underbrace{\mathbf{p}_0 + \hat{\partial}_\tau [\mathbf{\Gamma}_1^{(p)}(\tau)]_{\mathbf{p}=\mathbf{0}}}_{=0} \right. \\ &\quad \left. + \underbrace{\mathbf{p}_1 + \hat{\partial}_\tau [\mathbf{p}_0 \cdot \hat{\nabla}_{\mathbf{p}} \mathbf{\Gamma}_1^{(p)}(\tau) + \hat{\nabla}_{\mathbf{p}} \mathbf{\Gamma}_2^{(t)}(\tau) + \mathbf{\Gamma}_3^{(p)}(\tau)]_{\mathbf{p}=\mathbf{p}_0}}_{\propto 1/c} \right) + \mathcal{O}(1/c^2), \\ \Rightarrow \mathbf{p}_1 &= -\frac{1}{t-t'} \left[[\mathbf{p}_0 \cdot \hat{\nabla}_{\mathbf{p}} \mathbf{\Gamma}_1^{(p)}(\tau) + \hat{\nabla}_{\mathbf{p}} \mathbf{\Gamma}_2^{(t)}(\tau) + \mathbf{\Gamma}_3^{(p)}(\tau)]_{\mathbf{p}=\mathbf{p}_0} \right]_{t'}^t, \end{aligned} \quad (4.56)$$

where $\hat{\nabla}_{\mathbf{p}} \mathbf{\Gamma}_{4/5}^{(t)}$ in $\hat{\nabla}_{\mathbf{p}} \mathbf{\Gamma}^{(A)}$ are neglected as higher-order corrections. In principle, this procedure could be extended to higher orders. Since the quasi-classical action $S(\mathbf{p}, t, t')$ induces rapid oscillations, higher-order terms may show some significance in the future. However, this dissertation discusses nondipole effects within a bare model such that these higher-order corrections to the saddle-point momentum are neglected in the first instance. The nondipole saddle-point momentum consequently reads

$$\mathbf{p}_s(t, t') = \mathbf{p}_0 - \frac{1}{t-t'} \left[[\mathbf{p}_0 \cdot \hat{\nabla}_{\mathbf{p}} \mathbf{\Gamma}_1^{(p)}(\tau) + \hat{\nabla}_{\mathbf{p}} \mathbf{\Gamma}_2^{(t)}(\tau) + \mathbf{\Gamma}_3^{(p)}(\tau)]_{\mathbf{p}=\mathbf{p}_0} \right]_{t'}^t. \quad (4.57)$$

While the saddle-point momentum was non-trivial to determine, the analytical computation of the Hessian determinant remains straightforward. This dissertation will therefore not focus on the derivation of the Hessian determinant but assume its existence as well as its closed algebraic form. Furthermore, in this dissertation, explicit computations of the Hessian determinant are performed by the computer-algebra system Mathematica [6].

The atomic dipole moment in the SPA follows from the previous derivation via

$$\mathbf{D}(t) = i(2\pi i)^{3/2} \int_{-\infty}^t dt' \mathbf{\Upsilon}^\dagger(\mathbf{p}_s, t) \frac{\mathbf{E}(t') \cdot \mathbf{\Upsilon}(\mathbf{p}_s, t') - \Lambda(\mathbf{p}_s, t')}{\sqrt{\det(S''(\mathbf{p}_s))}} e^{-iS(\mathbf{p}_s, t, t')}, \quad (4.58)$$

with the Hessian determinant defined as $\det(S''(\mathbf{p}_s)) \equiv H_{\mathbf{p}}(S)|_{\mathbf{p}=\mathbf{p}_s}$.

Quantum orbit approach

The quantum orbit (QO) approach is of particular interest within the nondipole regime since numerical computations are expensive. The discussion of the QO approach in this section is based on the respective discussion concerning the dipole regime in Sec. 3.4.4. The atomic dipole moment in the frequency domain is given by

$$\begin{aligned} \mathbf{D}_q &= \int_{-\infty}^{\infty} dt \mathbf{D}(t) e^{i\omega_q t}, \\ &= i(2\pi i)^{3/2} \int_{-\infty}^{\infty} dt \int_{-\infty}^t dt' \boldsymbol{\Upsilon}^\dagger(\mathbf{p}_s, t) \frac{\mathbf{E}(t') \cdot \boldsymbol{\Upsilon}(\mathbf{p}_s, t') - \Lambda(\mathbf{p}_s, t')}{\sqrt{\det(S''(\mathbf{p}_s))}} e^{-i\Theta(t, t')}, \end{aligned} \quad (4.59)$$

with the intrinsic phase $\Theta(t, t') \equiv S(\mathbf{p}_s, t, t') - \omega_q t$. The temporal integrals can be analytically approximated by the saddle-point approximation, as mentioned previously. The respective saddle-point condition consists of a system of coupled nonlinear equations

$$0 \equiv \hat{\partial}_{t'} \Theta(t, t')|_{(t, t')=(t_s, t'_s)} \Rightarrow \frac{1}{2} \mathbf{p}_s^2(t_s, t'_s) + \hat{\partial}_{t'} \Gamma^{(t)}(t')|_{\mathbf{p}=\mathbf{p}_s} = -I_p, \quad (4.60)$$

$$0 \equiv \hat{\partial}_t \Theta(t, t')|_{(t, t')=(t_s, t'_s)} \Rightarrow \frac{1}{2} \mathbf{p}_s^2(t_s, t'_s) + \hat{\partial}_t \Gamma^{(t)}(t)|_{\mathbf{p}=\mathbf{p}_s} = \omega_q - I_p, \quad (4.61)$$

that need to be solved numerically to obtain the respective temporal saddle points (t_s, t'_s) . Finally, the atomic dipole moment within the QO approach reduces to

$$\mathbf{D}_q = i(2\pi i)^{5/2} \sum_s \boldsymbol{\Upsilon}^\dagger(\mathbf{p}_s, t_s) \frac{\mathbf{E}(t'_s) \cdot \boldsymbol{\Upsilon}(\mathbf{p}_s, t'_s) - \Lambda(\mathbf{p}_s, t'_s)}{\sqrt{\det(S''(\mathbf{p}_s)) \det(S''(t_s, t'_s))}} e^{-i\Theta(t_s, t'_s)}. \quad (4.62)$$

All explicit computations in this chapter are done within the QO approach and refer to Eq. (4.62)

4.3.3. Results

So far, the generalized nondipole SFA (GN-SFA) of HHG has been motivated and introduced. The GN-SFA considers the weakly relativistic contributions ($\propto 1/c$) of spatially structured light fields. The formal differences between the GN-SFA and the standard nondipole SFA of high-order harmonic generation [93, 98] are discussed in the following. Even though many other investigations beyond the dipole approximation are

available, see [30, 100, 103, 116], no work considers the analytically correct nondipole Volkov state Eq. 4.4. Here, the specific mathematical structure of the model is compared to the standard nondipole SFA. Essential differences are highlighted in terms of their physical context and their resulting implications in the following:

- **Nondipole matrix element:** The nondipole matrix element represents the extension of the dipole matrix element into the weakly relativistic regime. Although the nondipole matrix element in Eqs. (4.36) and (C.1) seems to be quite complicated, many terms may be neglected as higher-order corrections or due to the Coulomb gauge condition. The remaining terms in Eq. (C.3), emerge as direct consequences of the derivation shown in this chapter. These terms are not considered in the standard nondipole SFA and may lead to some interesting new phenomena, e.g. noncollinear multi-beam arrangements where $\boldsymbol{\pi} \cdot \mathbf{k}_j$ does not vanish. Furthermore, a significant effect of the nondipole matrix elements is associated with the radial nondipole Volkov phase $\Gamma^{(r)}(t)$. In particular, complex beams such as Laguerre-Gaussian and Bessel beams could lead to significant deviations with respect to the plane-wave-like contributions of the standard nondipole SFA. These beams are particularly interesting as they have a non-vanishing opening angle, see Sec. 2.4, which yields a finite contribution $\Gamma_3(\mathbf{r}, t)$ in the nondipole Volkov phase. So far, other high-order harmonic nondipole SFA's have not considered this contribution.
- **Quasi-classical action:** A notable difference to the standard non-dipole SFA is found in the action $S(\mathbf{p}, t, t')$. So far, there exists no method to rewrite the integrand of the action (4.27) as the square of the respective kinetic momentum $\boldsymbol{\pi}$, as done in the standard nondipole SFA. This originates from an absent relativistic correction of the nondipole Volkov phase, proportional to $1/c^2$. The action in the standard nondipole SFA reads

$$\begin{aligned} S(\mathbf{p}, t, t') &= \int_{t'}^t d\tau \left(\boldsymbol{\pi}^2(\mathbf{p}, \tau) + I_p \right) \\ &= \int_{t'}^t d\tau \left[\left(\boldsymbol{\pi}_0(\mathbf{p}, \tau) + \frac{1}{c} \boldsymbol{\pi}_1(\mathbf{p}, \tau) \right)^2 + I_p \right]. \end{aligned} \quad (4.63)$$

Here, the second-order correction $\propto 1/c^2$ is associated with the square of the kinetic moments relativistic correction $\boldsymbol{\pi}_1(\mathbf{p}, \tau)/c$. So far, the absent contribution within the GN-SFA is assumed to be an artifact induced by the particular computation technique of the nondipole Volkov states. Here, already the Hamiltonian (4.7) is restricted to corrections up to the first relativistic order whereas the standard nondipole SFA contains corrections up to the second order. The second-order correc-

tion seems to yield an essential contribution to describing laser field configurations of very high wavelengths and field intensities. In other words, the GN-SFA approximates the *Hamiltonian* up to the first relativistic order. In contrast, the standard nondipole SFA approximates a specific contribution of the Hamiltonian, namely the *kinetic momentum*. Overall, the approximation of the kinetic momentum, as an observable, seems to be more natural than the approximation of the Hamiltonian. Deriving and utilizing the nondipole Volkov states including second-order corrections is an approach to resolve the disagreement between both models. Nevertheless, more elaborated considerations are beyond the scope of this dissertation. Nevertheless, this offers interesting tasks and questions for further investigation.

- **Spatial structure:** Perhaps the most important difference between the GN-SFA and the standard nondipole SFA is the generic spatial structure of the incident laser field in the nondipole Volkov state (4.4) and does not account for contributions associated with Γ_i with $i = 3, 4, 5$, see App. (B). The standard nondipole SFA restricts the laser field geometry to a specific setup whereas the GN-SFA does not. The theoretical framework of the GN-SFA is valid for a large set of laser field configurations such as pulses, noncollinear multi-beam alignments, or twisted light beams. This type of generality is not incorporated, and thus beyond the standard nondipole SFA. A recent study on HHG by twisted light beams has shown interesting nondipole features associated with high orbital angular momenta [117]. Investigations on similar systems with more sophisticated methods like the GN-SFA could give insight into the underlying dynamics.
- **Photon momentum:** The connection to relativistic strong-field physics offers some important insight about the dynamics of the continuum electron: the relativistic factor, or effective mass term, $\eta_{\mathbf{k}} = \mathbf{p} \cdot \mathbf{k} - \omega_{\mathbf{k}}$ (which reduces to $\eta_{\mathbf{k}} = -\omega_{\mathbf{k}}$ in the dipole theory) can be interpreted as giving the continuum electron an effective momentum-dependent mass $m_{\text{eff}} = m_e - p_z/c$ (plane wave beam) [113]: This effect is also referred to as a recoil effect from the momentum of the absorbed photons and can be classically associated with the magnetic displacement. The effective mass term occurs in the exact (nondipole) solution of the Schrödinger equation [105] (Eq. (2), $G(\eta) \rightarrow 1$) and the first order nonrelativistic expansion of the Dirac-Volkov states [113] for a single plane wave mode. This provides a hint that the effective mass term is part of a more accurate relativistic description of strong-field processes, which is not incorporated in the standard nondipole SFA.

4.4. Elliptically polarized plane wave beam

4.4.1. Parameters of the generalized nondipole strong-field approximation

This section utilizes the GN-SFA to investigate HHG from elliptically polarized plane wave beams. These beams provide the opportunity to compare the results of the GN-SFA to the standard nondipole SFA since plane wave beams were extensively discussed in the past [93, 98]. The respective beam-dependent parameters of the GN-SFA are determined in the following. The complex amplitude and the associated vector potential of an elliptically polarized plane wave beam (2.20) are expressed as

$$\begin{aligned} \mathbf{a}_{\mathbf{k}} &= \frac{A_0}{\sqrt{1+\epsilon^2}} (\mathbf{e}_x + i\epsilon\Lambda\mathbf{e}_y) \delta(\mathbf{k} - \mathbf{k}_0), \\ \Rightarrow \mathbf{A}_{\mathbf{k}_0}(t) &\equiv \int d^3\mathbf{k} \operatorname{Re} \left[\mathbf{a}_{\mathbf{k}} e^{i u_{\mathbf{k}}^{(0)}} \right] = \frac{A_0}{\sqrt{1+\epsilon^2}} \operatorname{Re} \left[(\mathbf{e}_x + i\epsilon\Lambda\mathbf{e}_y) e^{i u_{\mathbf{k}_0}^{(0)}} \right]. \end{aligned} \quad (4.64)$$

The momentum vector \mathbf{k}_0 of the resulting laser field is orthogonal to the polarization plane, such that contributions proportional to $\mathbf{k}_0 \cdot \mathbf{a}_{\mathbf{k}_0} \Leftrightarrow \sigma_{\mathbf{k}_0 \mathbf{k}_0}$ vanish identically in the nondipole Volkov phase. Explicitly, the full non-dipole Volkov phase (B.1) reduces to

$$\begin{aligned} \Gamma(\mathbf{r}, t) &= \Gamma_1(\mathbf{r}, t) + \Gamma_2(\mathbf{r}, t), \\ &\approx \mathbf{r} \cdot (\mathbf{\Gamma}_1^{(r)}(t) + \mathbf{\Gamma}_2^{(r)}(t)) + \mathbf{p} \cdot \mathbf{\Gamma}^{(p)}(t) + \Gamma^{(A)}(t), \end{aligned} \quad (4.65)$$

with $\mathbf{p} \cdot \mathbf{\Gamma}^{(p)} = \Gamma_1^{(t)}$ and $\Gamma^{(A)} = \Gamma_2^{(t)}$. The respective terms of the nondipole Volkov phase follow with

$$\Gamma_1^{(t)}(t) = \mathbf{p} \cdot \mathbf{\Gamma}^{(p)} = -\mathbf{p} \cdot \int^t d\tau \frac{\omega_{\mathbf{k}_0}}{\eta_{\mathbf{k}_0}} \mathbf{A}_{\mathbf{k}_0}(\tau), \quad (4.66a)$$

$$\Gamma_2^{(t)}(t) = - \int^t d\tau \frac{\omega_{\mathbf{k}_0}}{\eta_{\mathbf{k}_0}} \frac{\mathbf{A}_{\mathbf{k}_0}^2(\tau)}{2}, \quad (4.66b)$$

$$\mathbf{\Gamma}_1^{(r)}(t) = \frac{\mathbf{k}_0}{\eta_{\mathbf{k}_0}} (\mathbf{p} \cdot \mathbf{A}_{\mathbf{k}_0}(t)), \quad (4.66c)$$

$$\mathbf{\Gamma}_2^{(r)}(t) = \frac{\mathbf{k}_0}{\eta_{\mathbf{k}_0}} \frac{\mathbf{A}_{\mathbf{k}_0}^2(t)}{2}. \quad (4.66d)$$

The saddle-point momentum (4.57) reduces to

$$\mathbf{p}_s = \mathbf{p}_0 - \frac{1}{t-t'} \frac{\mathbf{k}_0}{\omega_{\mathbf{k}_0}} \int_{t'}^t d\tau \left(\mathbf{p}_0 \cdot \mathbf{A}_{\mathbf{k}_0}(\tau) + \frac{1}{2} \mathbf{A}_{\mathbf{k}_0}^2(\tau) \right), \quad (4.67)$$

with the derivation presented in Eq. (B.4), and the nondipole matrix element shown in App. C. Finally, the exponential phase in Eq. (4.62) is cast into the following form

$$\begin{aligned} \Theta(t, t') &= S(t, t') - \omega_q t = \int_{t'}^t d\tau \left(E_{\mathbf{p}_s} + \hat{\partial}_\tau \Gamma_1^{(t)}(\tau) + \hat{\partial}_\tau \Gamma_2^{(t)}(\tau) + I_p \right) - \omega_q t, \\ &= \int_{t'}^t d\tau \left[\frac{\mathbf{p}_s^2}{2} - \frac{\omega_{\mathbf{k}_0}}{\eta_{\mathbf{k}_0}} \left(\mathbf{p}_s \cdot \mathbf{A}_{\mathbf{k}_0}(\tau) + \frac{1}{2} \mathbf{A}_{\mathbf{k}_0}^2(\tau) \right) + I_p \right] - \omega_q t. \end{aligned} \quad (4.68)$$

Comparing the quasi-classical action S in Eq. (4.68), with the one of the standard nondipole SFA [98] (Eq. (9)) highlights two main differences. First, the standard nondipole SFA does not incorporate the effective mass term $\eta_{\mathbf{k}}$, and second, the action in Eq. (4.68) only considers relativistic corrections up to $1/c$. The missing relativistic correction $\propto 1/c^2$ was already mentioned in Sec. 4.3.3. Both actions are equivalent after a Taylor expansion of the effective mass term $\eta_{\mathbf{k}_0}^{-1} \approx -\omega_{\mathbf{k}_0}^{-1}(1 + \mathbf{p} \cdot \mathbf{k}_0/\omega_{\mathbf{k}_0})$, apart from the missing higher-order relativistic correction.

The GN-SFA does not yield the exactly same results as the standard nondipole SFA for a plane wave laser field. Potential reasons for this are discussed in Sec. 4.3.3. However, the GN-SFA provides a formal extension of HHG for spatially structured light fields which has been absent so far. Minor differences can be investigated in the future.

4.4.2. Discussion

The weakly relativistic correction to the dipole Volkov states represents the inclusion of a finite photon momentum [112, 113]. Similarly, it is understood as the occurrence of a nonvanishing magnetic field that induces a Lorentz force parallel to the propagation direction [118]. Overall, these nondipole features decrease the recombination rate for high-order harmonic generation and consequently suppress the harmonic yield. This suppression is illustrated in the high-harmonic spectrum of Fig. 4.3, where the x component of the atomic dipole moment D_x^{ND} (green, GN-SFA) is suppressed compared to the dipole moment D_x^D (blue, SFA). The z component D_z^{ND} (red, GN-SFA) refers to the contribution of the atomic dipole moment in the propagation direction and emerges as a consequence of the finite spatial structure of the laser field. The two downward peaks in the spectra

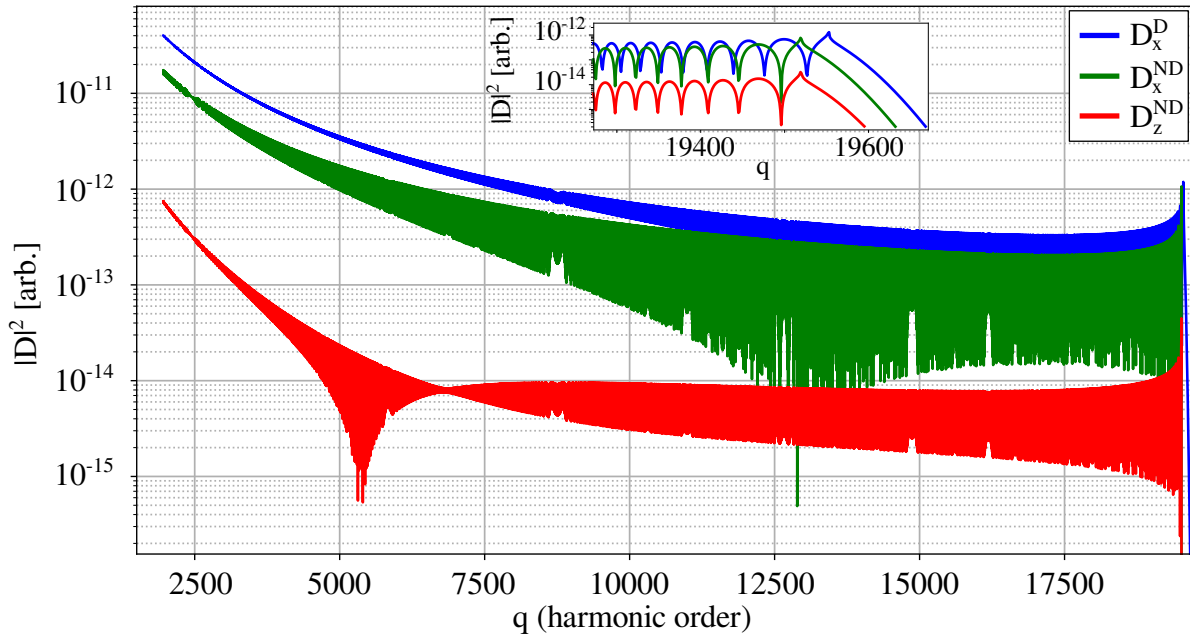


Figure 4.3.: High-order harmonic spectrum of a linearly polarized laser field with a rectangular pulse envelope. The peak intensity is chosen as $I_0 = 2 \cdot 10^{14} \text{ W/cm}^2$ with a pulse duration of one optical period T_0 and a wavelength of $\lambda = 7400 \text{ nm}$. The incident laser field irradiates a gaseous neon target with an ionization potential of $I_p = 21.56 \text{ eV}$. The atomic dipole moment for the x and z component is computed within the GN-SFA and denoted by $D_{x/z}^{ND}$ (4.62) where the atomic dipole moment from the dipole SFA is considered as D_x^D (3.53). The inset highlights the HHG spectrum in the cutoff region. A small shift of the HH cutoff can be seen toward lower Harmonic energies.

D_x^{ND} and D_z^{ND} are remarkable as they do not occur in the respective dipole theory. These downward peaks are lower valleys in the quantum path interference oscillations, reflecting the balanced in intensity of the short and long trajectories. Therefore, they are better able to interfere with each other. Furthermore, the inset of Fig. 4.3 illustrates a feature of the GN-SFA in which the HH cutoff marginally shifts towards lower energy. Nevertheless, the standard cutoff law associated with a maximum photon energy of $E_c = 3.2U_p + I_p$ remains valid as the relative shift is reasonably small, compared to the cutoff itself.

The decrease of the atomic dipole momentum concerning the intensity I_0 and wavelength λ of the laser field is demonstrated in Fig. 4.4. Here, the ratio R between the atomic dipole moment within the dipole SFA (3.53) and the GN-SFA (4.62) is computed via,

$$R^{(\lambda/I_0)} = \frac{|\int dq \mathbf{D}_q^{ND}|}{|\int dq \mathbf{D}_q^D|}, \quad (4.69)$$

where $\mathbf{D}^D(q)$ and $\mathbf{D}^{ND}(q)$ represent the atomic dipole moment in the respective dipole and nondipole theory. The ratio $R^{(\lambda)}$ (4.69) is depicted in Fig. 4.4a as a function of the wavelength for a fixed field intensity of $I_0 = 2 \cdot 10^{14} \text{ W/cm}^2$ and an ionization potential $I_p = 21.56 \text{ eV}$ (Ne). On the other hand, Fig. 4.4b shows the ratio $R^{(I_0)}$ as a function of the field intensity for a fixed wavelength of $\lambda = 800 \text{ nm}$ and the ionization potential $I_p = 122.45 \text{ eV}$ (Li^{2+}), of doubly ionized lithium. The insets in Fig. 4.4 highlight the harmonic spectrum close to the cutoff region for the parameters ($I_0 = 4 \cdot 10^{16} \text{ W/cm}^2$, $\lambda = 800 \text{ nm}$ and $I_0 = 2 \cdot 10^{14} \text{ W/cm}^2$, $\lambda = 6800 \text{ nm}$) denoted by the purple star, respectively. The decrease of both ratios R can be seen via the orange curve or the respective inset.

So far, the decrease of the high-order harmonic yield is classically and quasi-classically understood as the influence of a magnetic field on the dynamics of the continuum electron or the absorption of photons alongside their linear momentum, respectively. These effects lead to a magnetic displacement that suppresses the high-order harmonic yield, as discussed at the beginning of Sec. 4.3.

4.5. Outlook: Spatially structured light beams

Actually, the GN-SFA is developed to consider nondipole effects in light fields with nontrivial spatial structures. Due to the limited time, explicit investigations on twisted

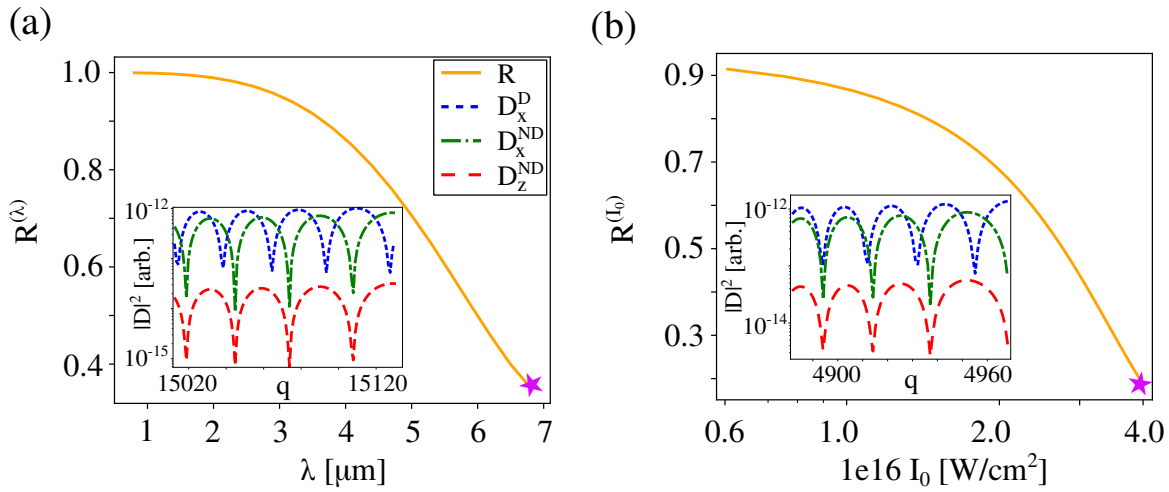


Figure 4.4.: Suppression of the atomic dipole moment about the laser field wavelength λ (a) and the intensity I_0 (b), respectively. A rectangular pulse envelope of the incident beam is considered with a pulse duration of one fundamental period T_0 . The atomic dipole momentum is computed within the dipole SFA (3.53) and the GN-SFA (4.62). D_x^{ND} (green dash-dotted) and D_z^{ND} (red dashed) are associated with the atomic dipole moment computed within the GN-SFA for the x and z components, respectively. The atomic dipole moment within the dipole SFA is denoted by D_x^D (blue dotted): (a) Wavelength dependent ratio (orange solid) of the coherent sum in Eq. (4.69), with ionization potential $I_p = 21.56$ eV (Ne). The inset illustrates the harmonic spectrum close to the respective cutoff region with fixed intensity $I_0 = 2 \cdot 10^{14}$ W/cm² and wavelength $\lambda = 6800$ nm (purple star). (b) Atomic dipole moment as a function of the beam intensity I_0 for a fixed wavelength of $\lambda = 800$ nm and the ionization potential $I_p = 122.45$ eV (Li²⁺). The laser field parameters in the inset are chosen as $I_0 = 4 \cdot 10^{16}$ W/cm² and $\lambda = 800$ nm (purple star).

light beams are unfortunately out of the scope of the dissertation program. However, this section will provide a brief motivation for further investigations.

Let the incident laser field be a superposition of two circularly polarized Bessel (see Sec. 2.4) beams with opposite helicity $\pm\Lambda$, opposite projected total angular momentum $\pm m_\gamma$ and vanishing relative phase difference. In the paraxial regime (see Eq. 2.27), this configuration represents a locally linearly polarized Bessel beam. The complex amplitude of the incident nonparaxial Bessel beam is deduced from Eq. (2.23) and Def. (2.3) via

$$\mathbf{a}_\mathbf{k} = \frac{A_0}{(2\pi)^2} \sqrt{\frac{2\pi}{\kappa}} \delta(k_\perp - \kappa) \delta(k_z - k_0) \sum_{\pm} (-i)^{\pm m_\gamma} e^{\pm i m_\gamma \varphi_\mathbf{k}} \boldsymbol{\epsilon}_{\mathbf{k}\pm\Lambda}, \quad (4.70)$$

$$\mathbf{A}_\mathbf{k} = \text{Re} \left[\mathbf{a}_\mathbf{k} e^{i u_\mathbf{k}^{(0)}} \right]. \quad (4.71)$$

This section shall give a brief impression of why spatially structured light fields are of particular interest in HHG. To do so, the contribution $\Gamma_3^{(t)}(t)$ of the temporal Volkov phase in Eq. (4.50) is discussed. As the contribution consists of two separate terms, the discussion is further limited to the term associated with the + index (see Eq. (B.1d) with $\mathbf{r} \rightarrow \mathbf{r}_0$) of the summation to simplify the equation and circumvent singularities. The remaining term in $\Gamma_3^{(t)}(t)$ reads as

$$I(\vartheta) = \frac{1}{2} \int d^3\mathbf{k} d^3\mathbf{k}' \sigma_{\mathbf{k}\mathbf{k}'} \lambda_\mathbf{k} \frac{\sin(u_\mathbf{k}^{(0)} + u_{\mathbf{k}'}^{(0)} + \theta_\mathbf{k} + \zeta_{\mathbf{k}\mathbf{k}'})}{\eta_\mathbf{k}(\eta_\mathbf{k} + \eta_{\mathbf{k}'})}, \quad (4.72)$$

where the opening angle of both Bessel beams is defined as ϑ . The other parameters were discussed in detail below Eq. (4.5). As Eq. (4.72) vanishes in the case of plane wave beams; see Sec. 4.4; it yields a finite contribution for Bessel beams. The complex amplitude in Eq. (4.70) incorporates four Dirac delta distributions, and therefore four integrations concerning k_z, κ and k'_z, κ' , that can be performed analytically. This reduces Eq. (4.72) to

$$I(\vartheta) = \frac{1}{2} \int_0^{2\pi} d\varphi_\mathbf{k} d\varphi_{\mathbf{k}'} \sigma_{\mathbf{k}\mathbf{k}'} \lambda_\mathbf{k} \frac{\sin(u_\mathbf{k}^{(0)} + u_{\mathbf{k}'}^{(0)} + \theta_\mathbf{k} + \zeta_{\mathbf{k}\mathbf{k}'})}{\eta_\mathbf{k}(\eta_\mathbf{k} + \eta_{\mathbf{k}'})}. \quad (4.73)$$

The residual integrals are nontrivial and are therefore performed numerically. Figure 4.5 illustrates the respective results for an increasing opening angle ϑ of the Bessel beam. The radial position is chosen such that the target atom is located in the focus plane with a radial position (a) $|r| = 10$ nm and (b) $|r| = 100$ nm apart from the propagation

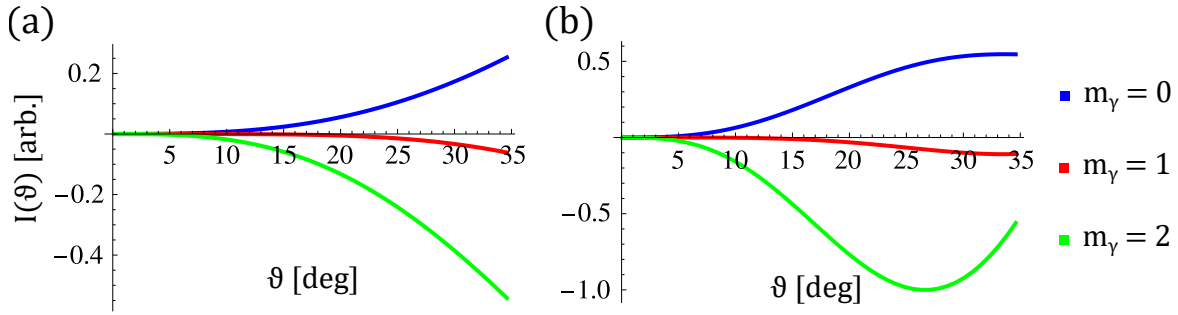


Figure 4.5.: Numerical computation of Eq. (4.73) for a linearly polarized Bessel beam with respect to the opening angle ϑ and radial position (a) $|r| = 10$ nm and (b) $|r| = 100$ nm. The remaining beam parameters are chosen as $I_0 = 2 \cdot 10^{14}$ W/cm² and $\lambda = 3200$ nm.

axis. The beam parameters of the incident laser are chosen as $I_0 = 2 \cdot 10^{14}$ W/cm² and $\lambda = 3200$ nm.

A significant impact on the respective contribution in the temporal nondipole Volkov phase is associated with the radial position of the target atom and the opening angle of the Bessel beam. Furthermore, the total angular momentum projection m_γ shows a significant influence as the sign in Fig. 4.5 changes for $m_\gamma : 0 \rightarrow 2$. This may offer the opportunity to counteract the magnetic displacement towards the propagation direction (see Sec. 4.1) with a tailored configuration of the opening angle and the total angular momentum projection. Previous investigations on nondipole HHG [30] and ATI [119] demonstrated this compensation of the magnetic displacement by two incident noncollinear plane-wave lasers. The restriction to a single Bessel beam could simplify the experimental setup and further highlight an essential step toward the understanding of weak relativistic dynamics in atomic strong-field physics.

CHAPTER 5.

CRITICAL INTENSITY OF HIGH-ORDER HARMONIC GENERATION

“The ‘paradox’ is only a conflict between reality and your feeling of what reality ‘ought to be’”

— Richard Feynman

High-order harmonic generation (HHG) is an essential technique for producing coherent ultra-short light pulses from tabletop-sized devices. Radiation from these devices can be utilized in industry and scientific research, which highlights HHG as a key source for a broad range of applications.

Major parts of the material presented in this chapter were previously published in:

Critical laser intensity of phase-matched high-order harmonic generation in noble gases

Minneker, B.; Klas, R.; Rothhardt, J; Fritzsche, S.

[Photonics 2023, 10\(1\), 24.](#)

The macroscopic HHG conversion efficiency is in the order of 10^{-4} at 30 eV [58] and decreases to 10^{-9} for 300 eV [46]. Especially, the conversion efficiency of HHG from near- to mid-infrared laser pulses decreases fast with increasing wavelengths, which is demonstrated in many theoretical and experimental works [25, 120]. The interest of the strong-field community in optimizing the HH yield has consequently increased drastically within the last decades [61, 121–123]. The highest efficiencies are achieved by simultaneously optimizing macroscopic effects such as absorption [124], laser focusing [125, 126], and phase-matching [127–129].

Phase-matching (PM) is one of the essential requirements for the efficient generation of HH radiation. Therefore, the phase velocity of the incident laser pulse and the generated HH radiation need to match while propagating through the gas medium. The PM of complex laser fields, for example, twisted light [129], is often complicated, so linearly polarized laser pulses are advantageous to simplify the PM conditions. Commonly used media for the generation of HH radiation are isotropic noble gases, which are the focus of this chapter. In particular, the plasma (free electrons + ions) and neutral gas dispersion, the geometric phase, and the intrinsic phase are balanced to achieve a transient PM window [127]. Plasma and neutral gas dispersion contribute significantly to PM, whereas geometric and intrinsic contributions nullify.

This chapter analytically investigates the PM conditions for partially ionized noble gases in the free-focusing regime, see [130]. While the ionization of the gas target is investigated, other PM contributions are nullified in the experimental setup discussed. These assumptions allow one to discuss an experimental setup under realistic conditions and further demonstrate a newly developed calculation technique. Here, a Gaussian laser pulse exhibits an inverse logarithmic dependence of the critical intensity on the pulse duration. Furthermore, analytical expressions of the critical intensity are derived within the ADK and PPT theory, respectively. The developed expressions yield highly accurate results while comparing them to numerical computations. The end of this chapter highlights further applications of the derived formulas with a specific example.

5.1. Model and Method

This chapter focuses on the linear propagation effects of the HH radiation and the incident laser pulse inside the gas medium. Here, the particular focus lies on the PM of both light fields. Figure 5.1a shows a standard HHG setup with the incident laser pulse on the left (orange-red) and the HH radiation emitted on the right (blue), while the dashed circle highlights the respective PM region.

The medium consists of an arbitrary noble gas, characterized by the ionization potential I_p and the orbital angular momentum ℓ of the respective atomic state. The incident laser beam is a paraxial linearly polarized plane-wave with a Gaussian pulse envelope propagating on the optical axis (z-axis) that irradiates a gas target (free-focusing regime). The optical axis is perpendicular to the target surface in the x-y plane, while the target itself is located one Rayleigh length behind the focus of the incident laser

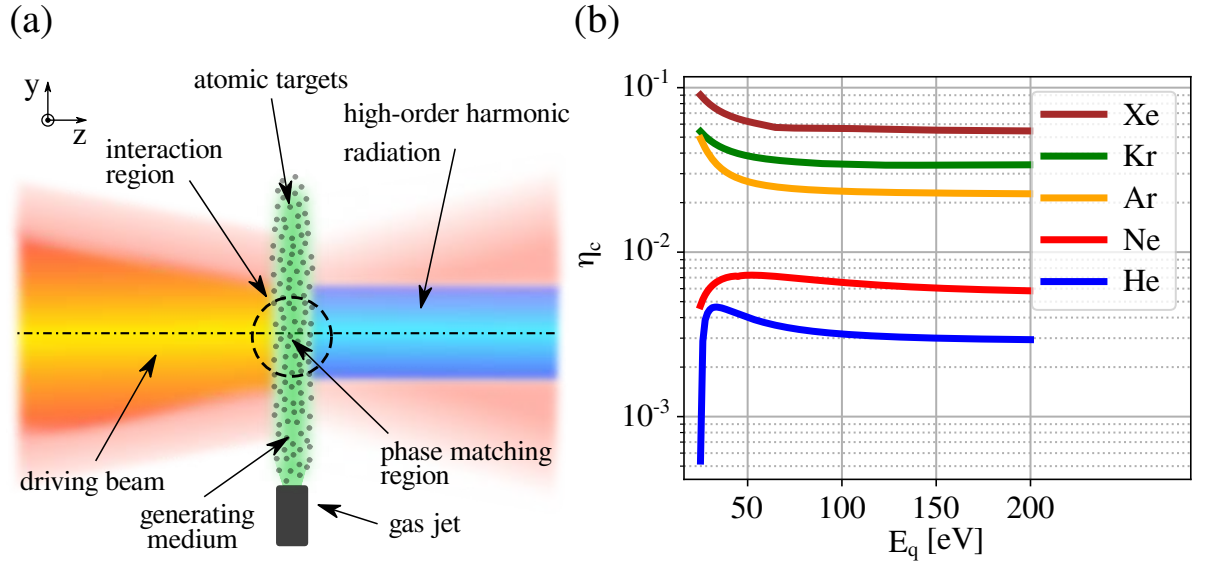


Figure 5.1.: (a) HHG-setup: laser pulse (orange-red), atomic targets (gray), generating medium (green), high-order harmonic radiation (blue), gas-jet emitter (gray-black), and (b) critical ionization probability η_c of commonly used noble gases about the photon energy of the emitted harmonics E_q at the fundamental laser wavelength of $\lambda = 1000$ nm.

pulse $z = z_R$ (not explicitly shown in Figure 5.1a). This position favors the coherent generation of HH photons associated with the short trajectory within the quantum orbit approach [131]. For thin gas targets, the electric field strength on the optical axis is constant in the free-focusing regime. The SI unit system is used in the following section 5.1.1.

5.1.1. Phase-matching of high-order harmonic radiation

Efficient HHG is achieved for a coherent superposition of HH radiation where the z-component of the wave-vector mismatch is minimized, which reads

$$\Delta k = k(q\omega) - qk(\omega). \quad (5.1)$$

The first term is associated with the HH radiation, while the second term belongs to the incident laser pulse. This mismatch Δk can be separated into several contributions. In the free-focusing regime, the wave-vector mismatch consists of four major contributions

$$\Delta k = \Delta k_{\text{atom}} + \Delta k_{\text{plasma}} + \Delta k_{\text{Gouy}} + \Delta k_{\text{intrinsic}} \equiv 0, \quad (5.2)$$

as discussed in Ref. [132]. The contributions Δk_{atom} and Δk_{plasma} consider the mismatch associated with the neutral and ionized atom dispersion, respectively. Moreover, Δk_{Gouy} denotes the geometric contribution of the Gouy phase, while $\Delta k_{\text{intrinsic}}$ represents the wave-vector mismatch related to the intrinsic phase of the emitted photons. The Gouy phase wave-vector mismatch is positive, whereas the intrinsic phase contributes negatively. Both contributions eventually nullify $\Delta k_{\text{Gouy}} + \Delta k_{\text{intrinsic}} \approx 0$, as the target is centered one Rayleigh length behind the focus of the incident laser, [33, 131, 133]. The remaining contributions Δk_{atom} and Δk_{plasma} are related to the atom and plasma dispersion, respectively, which eventually combine to a general *dispersion* mismatch

$$\begin{aligned} \Delta k_{\text{disp}} &= \Delta k_{\text{atom}} + \Delta k_{\text{plasma}}, \\ \Rightarrow -q \frac{\omega}{c} \frac{\rho}{N_{\text{atm}}} \Delta \delta \left(1 - \frac{\eta}{\eta_c} \right) &= 0. \end{aligned} \quad (5.3)$$

Here, ω is the frequency of the laser pulse, c is the speed of light in vacuum, N_{atm} is the number of particles under standard conditions, ρ is the respective particle density and $\Delta \delta = n_0(\omega) - n_0(q\omega)$ denotes the difference between the refractive indices of the laser pulse and the q -th HH under standard conditions. The respective refraction indices n_0 are computed as in Ref. [134–136]. At the macroscopic scale, the ionization probability η represents the relative number of atoms in an ionized state compared to the total number of atoms. Within this context, η_c is the so-called *critical ionization probability*, see Chap. 2.3 in Ref. [132], that is given by

$$\eta_c = \left(1 + \frac{2\pi r_e N_{\text{atm}} c^2}{\omega^2 \Delta \delta} \right)^{-1}. \quad (5.4)$$

Here, $r_e = e^2 / (4\pi\epsilon_0 m_e c^2)$ is the classical electron radius. The ionization probability η fulfills the PM condition if it matches the critical ionization probability $\eta = \eta_c$, such that Eq. (5.3) vanishes. The critical ionization probability (5.4) of commonly used noble gases is shown in Figure 5.1b for an incident laser wavelength of $\lambda = 1000$ nm.

5.1.2. Critical intensity in the ADK theory

This section discusses strong-field ionization in the context of phase-matched high-order harmonic generation. The YI theory [53] provides a sufficient description of strong-field ionization. Since HHG is known to predominantly operate in the tunnel and multiphoton

ionization regime (see Tab. 3.1), further investigations are restricted to the ADK and PPT theory. Both theories are simplifications of the more general YI theory and are valid within their respective Keldysh parameter regime.

This section is divided into two parts. The first part highlights the scheme of achieving PM (5.3) by utilizing the respective critical intensity, whereas the second part incorporates a detailed derivation of the critical intensity, as well as a discussion of the applied approximations.

Critical intensity as phase-matching condition

For the complete laser pulse, it is generally impossible to satisfy the PM condition (5.3), since the ionization probability increases monotonically over time. However, the PM condition can be achieved at specific times, like the peak of the laser pulse, which is associated with the highest HH yield [61]. The ADK ionization rate is defined in Eq. (3.9) and reads

$$\begin{aligned}
 w^{\text{ADK}}(t) &= \frac{1}{(2\ell + 1)} \sum_{m=-\ell}^{\ell} w_m^{\text{ADK}}(t), \\
 &= \sum_{m=-\ell}^{\ell} \frac{|C_{n^*l^*}|^2 G_{lm} I_p}{(2\ell + 1)} \left(\frac{2(2I_p)^{3/2}}{E(t)} \right)^{2n^* - |m| - 1} e^{-\frac{2(2I_p)^{3/2}}{3E(t)}}, \\
 &\equiv \sum_{m=-\ell}^{\ell} \kappa_m \left(\frac{F_0}{E(t)} \right)^{g_m + 1} e^{-\frac{F_0}{E(t)}}, \tag{5.5}
 \end{aligned}$$

with the factors κ_m , F_0 and g_m that depend on the atomic species and were previously defined in Eq. (3.8), as well as the parameters $|C_{n^*l^*}|^2$ and G_{lm} defined in Eq. (3.3). The electric field of the laser pulse follows as

$$E(t) = E_0 f(t) \cos(\omega t), \quad f(t) = e^{-4 \ln(2) \left(\frac{t}{\tau}\right)^2}, \tag{5.6}$$

and is introduced in Eq. (2.17). Note that $f(t)$ denotes a Gaussian envelope with a full width at a half maximum pulse duration (FWHM) of τ . The ADK ionization probability in the peak of the laser pulse then reads [33]

$$\eta = \eta^{\text{ADK}} = 1 - e^{-\int_{-\infty}^0 w^{\text{ADK}}(t) dt}. \tag{5.7}$$

The ionization probability consequently depends on the wavelength of the laser λ , the atomic ionization potential I_p , the duration of the pulse τ , and the intensity of the laser pulse $I = \sqrt{E_0}$. It is experimentally challenging to adapt the atomic species or the wavelength of the laser pulse to fulfill the PM condition, while the intensity and the pulse duration can be controlled quite easily. With this in mind, the *critical intensity* I_c of the laser pulse follows as a function of the laser wavelength, atomic species, and pulse duration. The critical intensity is defined so that it satisfies the PM condition (5.3)

$$\eta(I, \tau, I_p, \lambda) = \eta_c \quad \Rightarrow \quad \eta(I_c(\tau, I_p, \lambda)) = \eta_c. \quad (5.8)$$

Numerical algorithms are often used to find the respective critical intensity I_c from Eq. (5.7), or more generally, the required intensity to achieve a certain ionization probability [65, 127, 132, 137]. These algorithms integrate the ADK ionization rate (5.5), or the PPT rate (5.23), numerically for a given intensity and iteratively optimize it until the intensity converges to the critical intensity $I \rightarrow I_c$. In other words, these algorithms couple the fast oscillating (temporal) integration in Eq. (5.7) to a root-finding algorithm. The full algorithm is computationally heavy, as the numerical integration must be executed separately for each iteration of the root-finding algorithm.

The approximation of the critical intensity, within ADK theory $I_c \rightarrow I_c^{(0)}$ (derivation in Sec. 5.1.2 (**Derivation of the critical intensity**)), results as

$$I_c^{(0)}(\tau, I_p, \lambda) = \left[\frac{g_0}{F_0} W_0 \left(-\frac{1}{g_0} \left(\frac{D_0}{\tau} \right)^{1/g_0} \right) \right]^{-2}, \quad \text{for } g_0 < 0, \quad (5.9a)$$

$$I_c^{(0)}(\tau, I_p, \lambda) = \left[\frac{g_0}{F_0} W_{-1} \left(-\frac{1}{g_0} \left(\frac{D_0}{\tau} \right)^{1/g_0} \right) \right]^{-2}, \quad \text{for } g_0 > 0, \quad (5.9b)$$

$$D_0 = 2\sqrt{2 \ln(2)} \frac{|\ln(1 - \eta_c)|}{\kappa_0}. \quad (5.9c)$$

Within the derivation of the critical intensity $I_c^{(0)}$ several approximations have been used, where each approximation reduces to one of the major assumptions mentioned in Def. 5.1. However, κ_m and g_0 are defined in Eq. (3.8) with $g_m \rightarrow g_0$, while the Lambert W function is denoted by W_i for its two real branches with $i \in \{0, -1\}$. The parameter g_0 is negative for all neutral noble gases, except xenon, so that Eq. (5.9a) shall be used for helium, neon, argon, and krypton while Eq. (5.9b) refers to xenon. Note that the variables F_0 and g_0 depend only on the atomic species, whereas $D_0 \propto \ln(1 - \eta_c(\lambda))$

DEFINITION 5.1: ASSUMPTIONS ON THE SYSTEM

- (i) $F_0/E_0 \gg 1$: The characteristic electric field of the atom $F_0 \propto I_p^{3/2}$ is much larger than the peak amplitude of the incident laser pulse E_0 .
- (ii) $n \gtrsim 8$: The number of optical cycles n of the laser pulse is sufficiently large.
- (iii) $m \neq \pm 1$: The contributions to the ionization rate of atomic states with magnetic quantum number $m = \pm 1$ are small.

depends on the wavelength of the incident laser pulse. The dependency of the critical intensity on the laser pulse is therefore imprinted in the critical ionization probability $\eta_c \rightarrow \eta_c(\lambda)$ and the pulse duration τ . Explicit values of g_0 , F_0 , and κ_0 are listed in Tab. 5.1 for several noble gases.

The critical intensity (5.9c) provides a reasonably simple dependence on the laser pulse parameters via

$$\begin{aligned} \frac{|\ln(1 - \eta_c(\lambda_0))|}{\tau_0} &= \frac{|\ln(1 - \eta_c(\lambda_1))|}{\tau_1}, \\ \Rightarrow \tau_1 &= \tau_0 \frac{|\ln(1 - \eta_c(\lambda_1))|}{|\ln(1 - \eta_c(\lambda_0))|} \approx \tau_0 \frac{\eta_c^1}{\eta_c^0} \quad \text{for } \eta_c(\lambda_0), \eta_c(\lambda_1) \ll 1. \end{aligned} \quad (5.10)$$

This provides a condition for a pulse duration τ_1 , for which the critical intensity of the incident laser pulse remains invariant while the laser parameters change from $\lambda_0, \tau_0 \rightarrow \lambda_1, \tau_1$. The factor $|\ln(1 - \eta_c)|$ is physically equivalent to the time-integrated ionization rate at the peak of the laser pulse

$$|\ln(1 - \eta_c)| = \int_{-\infty}^0 dt w^{\text{ADK}}(t). \quad (5.11)$$

Reformulating Eq. (5.10) leads to the following invariance relation:

The critical field intensity is invariant under a parameter change from (τ_0, λ_0) to (τ_1, λ_1) , if the relative time integrated ionization rate matches the relative pulse duration,

$$\frac{\tau_1}{\tau_0} = \frac{n_1 \lambda_1}{n_0 \lambda_0} = \frac{\ln(1 - \eta_c(\lambda_1))}{\ln(1 - \eta_c(\lambda_0))} = \frac{\ln(1 - \eta_c^1)}{\ln(1 - \eta_c^0)} \quad \text{and if } \eta_c^1, \eta_c^0 \ll 1 \Rightarrow \frac{\tau_1}{\tau_0} \approx \frac{\eta_c^1}{\eta_c^0}. \quad (5.12)$$

Table 5.1.: Parameters (3.8) to compute the critical intensity of hydrogen-like noble gases

	He	Ne	Ar	Kr	Xe
g_0	-0.5122	-0.4114	-0.1417	-0.0283	0.1182
F_0	1.6196	1.3303	0.8311	0.6958	0.5612
κ_0	6.5714	6.4204	6.1200	6.0226	5.9116

Simplifying Eq. (5.9) even further reveals a simple scaling law regarding the critical intensity for both, positive and negative, g_0 [138]

$$\begin{aligned}
 I_c^{(0)}(\tau, I_p, \lambda) &\approx \left[\frac{g_0}{F_0} \ln \left(\frac{1}{|g_0|} \left(\frac{D_0}{\tau} \right)^{1/|g_0|} \right) \right]^{-2} \propto F_0^2 \ln^{-2} \left(\frac{D_0}{\tau} \right), \\
 \Rightarrow I_c^{(0)}(\tau) &\propto \ln^{-2} \left(\frac{|\ln(1 - \eta_c)|}{\tau} \right). \tag{5.13}
 \end{aligned}$$

This rather simple scaling law describes the general proportionality of the critical intensity for all noble gases with respect to the pulse duration and the critical ionization probability of a quasi-monochromatic Gaussian laser pulse.

To summarize, the derived critical intensity in Eq. (5.9) depends on the incident laser pulse via the pulse duration τ and, indirectly, the wavelength of the laser pulse by $\eta_c(\lambda)$, where it obeys the proportionality $I_c^{(0)} \propto \ln^{-2} \left(\frac{|\ln(1 - \eta_c)|}{\tau} \right)$. The wavelength dependency is directly related to the critical ionization probability in which the refractive index is sensitive to the wavelength of the incident laser. The critical intensity does not significantly depend on ionized electrons from states with a magnetic quantum number of $m = \pm 1$. At the same time, the dependency on the ionization potential I_p cannot be derived so easily.

Derivation of the critical intensity

The following derivation utilizes a number of approximations that are directly associated with one of the assumptions in Def. 5.1.

The initial focus lies on the temporal integration in Eq. (5.5) to achieve an explicit expression for the critical intensity $I_c \rightarrow I_c(\tau, I_p, \lambda)$. The summation with respect to the

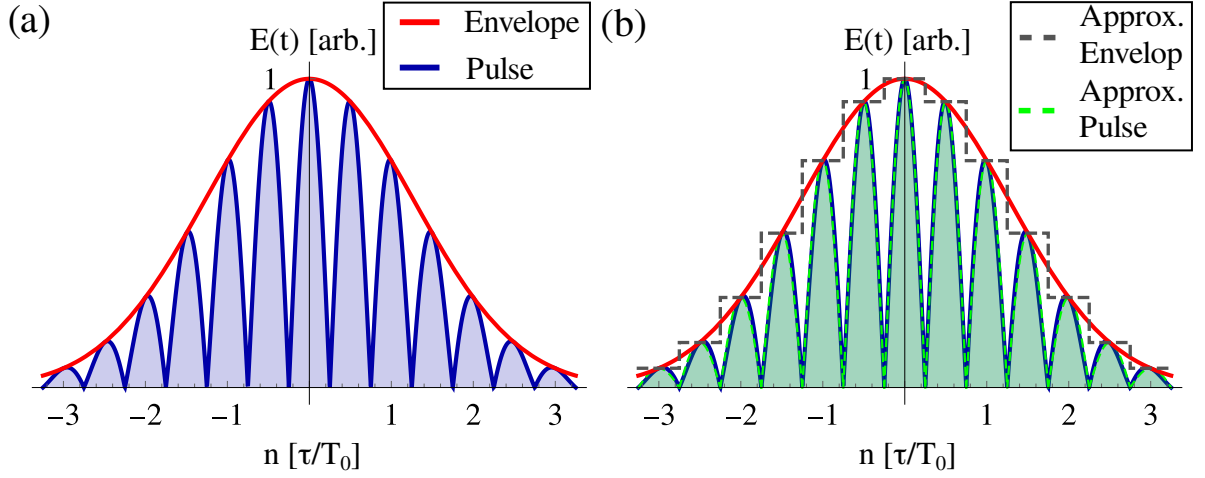


Figure 5.2.: Electric field of the approximate Gaussian pulse in Eq. (5.15) with $\tau = 3T_0$. (a) exact pulse (blue) with its envelope (red) (b) while the approximated pulse (green) and its envelope (gray) are shown on top of the exact pulse.

magnetic quantum number m is removed from the integral and omitted for the moment

$$\begin{aligned} \frac{1}{2\ell + 1} \int_{-\infty}^0 dt w_m^{\text{ADK}}(t) &= \frac{1}{2(2\ell + 1)} \int_{-\infty}^{\infty} w_m^{\text{ADK}}, \\ &= \frac{\kappa_m}{2} \int_{-\infty}^{\infty} dt \left(\frac{F_0}{E(t)} \right)^{g_m+1} e^{-\frac{F_0}{E(t)}}. \end{aligned} \quad (5.14)$$

In the next step, the Gaussian envelope is approximated by assuming a parametric time dependence, so that the envelope is constant within each half-cycle $t \in \left[-\frac{T_0}{4}, \frac{T_0}{4}\right]$. This approximation is valid for a slowly varying envelope, which is associated with a sufficiently large number of optical cycles Def. 5.1(ii). Fig. 5.2 illustrates the approximation of the Gaussian pulse for a pulse length of three optical cycles. Although the number of optical cycles is low, the approximation scheme is still accurate as the pulse and its respective approximation coincide reasonably well. However, in reality, the intrinsic phase of the envelope needs to be considered for short pulses. Finally, this limits the application of the approximation to pulse durations of more than seven to ten optical periods. Formally, the approximation is represented via

$$\frac{1}{2\ell + 1} \int_{-\infty}^0 dt w_m^{\text{ADK}}(t) \approx \frac{\kappa_m}{2} \sum_{k=-\infty}^{\infty} \int_{-T_0/4}^{T_0/4} dt \left(\frac{F_0}{E_0 f_k \cos(\omega t)} \right)^{g_m+1} e^{-\frac{F_0}{E_0 f_k \cos(\omega t)}}, \quad (5.15)$$

$$\approx \kappa_m \left(\frac{F_0}{E_0} \right)^{g_m+1} \sum_{k=-\infty}^{\infty} \int_0^{T_0/4} dt e^{-\frac{F_0}{E_0 f_k \cos(\omega t)}}. \quad (5.16)$$

The approximation in the last line neglects the factor $f_k \cos(\omega t)$ in the denominator, since the dominant contribution is associated with the argument of the exponential function [33]. Furthermore, the remaining integral approximates as

$$\begin{aligned} \int_0^{T_0/4} dt e^{-\frac{F_0}{E_0 f_k \cos(\omega t)}} &= \frac{T_0}{2\pi} \int_0^{\pi/2} dx e^{-\frac{F_0}{E_0 f_k \cos(x)}} \approx \frac{T_0}{2\pi} \int_0^\infty dx e^{-\frac{F_0}{E_0 f_k} \cosh(x)}, \\ \Rightarrow \int_0^{T_0/4} dt e^{-\frac{F_0}{E_0 f_k \cos(\omega t)}} &\approx \frac{T_0}{2\pi} K_0 \left(\frac{F_0}{E_0 f_k} \right), \end{aligned} \quad (5.17)$$

with the modified Bessel function of zeroth order $K_0 \left(\frac{F_0}{E_0 f_k} \right)$. Using the asymptotic expansion of the modified Bessel function for large $x = \frac{F_0}{E_0 f_k}$ ($K_0(x) \approx \sqrt{\frac{\pi}{2x}} e^{-x}$) yields [62]

$$\frac{1}{2\ell + 1} \int_{-\infty}^0 dt w_m^{\text{ADK}}(t) \approx \frac{T_0 \kappa_m}{2\pi} \left(\frac{F_0}{E_0} \right)^{g_m+1} \sqrt{\frac{\pi}{2}} \left(\frac{F_0}{E_0} \right)^{-1/2} \sum_{k=-\infty}^{\infty} e^{-\frac{F_0}{E_0 f_k}}. \quad (5.18)$$

Note that the contributions of the envelope to the denominator are neglected. The remaining summation reduces to

$$\begin{aligned} \sum_{k=-\infty}^{\infty} e^{-\frac{F_0}{E_0 f_k}} &= \sum_{k=-\infty}^{\infty} e^{-\frac{F_0}{E_0} e^{\ln(2)(k/n)^2}} \approx \sum_{k=-\infty}^{\infty} e^{-\frac{F_0}{E_0} (1+\ln(2))(k/n)^2}, \\ &\approx e^{-\frac{F_0}{E_0}} \int_{-\infty}^{\infty} dk e^{-\frac{F_0}{E_0} \ln(2)(k/n)^2} = n \sqrt{\frac{\pi}{\ln(2)}} \left(\frac{F_0}{E_0} \right)^{-1/2} e^{-\frac{F_0}{E_0}}, \\ \Rightarrow \sum_{k=-\infty}^{\infty} e^{-\frac{F_0}{E_0 f_k}} &\approx n \sqrt{\frac{\pi}{\ln(2)}} \left(\frac{F_0}{E_0} \right)^{-1/2} e^{-\frac{F_0}{E_0}}, \end{aligned} \quad (5.19)$$

with the definition $\tau = nT_0$ of the pulse duration for an integer number n of optical cycles. Inserting Eq. (5.19) into Eq. (5.18) yields an analytic formula of the ionization rate with

$$\frac{1}{2\ell + 1} \int_{-\infty}^0 dt w_m^{\text{ADK}}(t) \approx \frac{\tau \kappa_m}{2\sqrt{2 \ln(2)}} \left(\frac{F_0}{E_0} \right)^{g_m} e^{-\frac{F_0}{E_0}}. \quad (5.20)$$

Contributions of the terms $w_{\pm 1}^{\text{ADK}}$ are low compared to w_0^{ADK} and are consequently omitted. After the replacement $\eta \rightarrow \eta_c$ and minor rearrangement, Eq. (5.7) follows as

$$\begin{aligned} -\ln(1 - \eta_c) &\approx \frac{1}{(2\ell + 1)} \int_{-\infty}^0 w_0^{\text{ADK}}(t) dt, \\ \left(\frac{F_0}{\sqrt{I_c}} \right)^{g_0} e^{-\frac{F_0}{\sqrt{I_c}}} &= 2\sqrt{2 \ln(2)} \frac{|\ln(1 - \eta_c)|}{\tau \kappa_0} \equiv \frac{D_0}{\tau}. \end{aligned} \quad (5.21)$$

Note that the computation technique is independent of the replacement of $\eta \rightarrow \eta_c$ and may be used in other scenarios. By utilizing the definition of the Lambert function W_i ¹ which solves $xe^x = y \Rightarrow x = W_i(y)$ the critical intensity in Eq. (5.8) finally reads

$$I_c^{(0)}(\tau, I_p, \lambda) = \left[\frac{g_0}{F_0} W_0 \left(-\frac{1}{g_0} \left(\frac{D_0}{\tau} \right)^{1/g_0} \right) \right]^{-2}, \quad \text{for } g_0 < 0, \quad (5.22a)$$

$$I_c^{(0)}(\tau, I_p, \lambda) = \left[\frac{g_0}{F_0} W_{-1} \left(-\frac{1}{g_0} \left(\frac{D_0}{\tau} \right)^{1/g_0} \right) \right]^{-2}, \quad \text{for } g_0 > 0. \quad (5.22b)$$

$$D_0 = 2\sqrt{2 \ln(2)} \frac{|\ln(1 - \eta_c)|}{\kappa_0}, \quad (5.22c)$$

5.1.3. Critical intensity in the PPT theory

The previous section discussed the analytical method to calculate the critical intensity within the ADK theory. In the following, the formalism is extended to the PPT theory [33, 56], which incorporates multiphoton ionization alongside tunnel ionization. The PPT ionization rates have a more complex dependence on the laser intensity compared to the ADK rates. To proceed, a perturbative approach is applied which is similar to the one shown in Sec. 5.1.2.

The PPT ionization rate (3.6) is defined via

$$\begin{aligned} w^{\text{PPT}}(t) &= \frac{1}{(2\ell + 1)} \sum_{m=-\ell}^{\ell} w_m^{\text{PPT}}(t), \\ &= \sum_{m=-\ell}^{\ell} \kappa_m \left(\frac{F_0}{E(t)} \right)^{g_m+1} e^{-\frac{F_0}{E(t)} g(\gamma)} \\ &\quad \times \frac{4}{\sqrt{3\pi}} \frac{1}{|m|!} \frac{\gamma^2}{1 + \gamma^2} (1 + \gamma^2)^{(|m|+1)/2} \sum_{q \geq q_{thr}}^{\infty} A_q(\omega, \gamma), \end{aligned} \quad (5.23)$$

while the respective parameters are given in Eq. (3.5). The critical intensity within the ADK theory is used to approximate the Keldysh parameter as

$$\gamma = \omega \sqrt{\frac{2I_p}{I_c}} \approx \gamma(I_c^{(0)}) \equiv \gamma^{(0)}. \quad (5.24)$$

¹The index i indicates the two real branches of W_i for $i \in \{0, -1\}$

Inserting $\gamma^{(0)}$ into Eq. (5.23) then reads

$$w^{\text{PPT}}(t) \approx \sum_{m=-\ell}^{\ell} \kappa_m^{(0)} \left(\frac{F_0^{(0)}}{E(t)} \right)^{g_m+1} e^{-\frac{F_0^{(0)}}{E(t)}}, \quad (5.25)$$

with the definitions

$$\begin{aligned} \kappa_m^{(i)} &= \frac{\delta_{l,|m|} + \delta_{\ell-1,|m|}}{|m|!} \left(g(\gamma^{(i)}) \right)^{-(g_m+1)} \\ &\times \kappa_m \frac{4}{\sqrt{3\pi}} \frac{(\gamma^{(i)})^2}{1 + (\gamma^{(i)})^2} \left(1 + (\gamma^{(i)})^2 \right)^{(|m|+1)/2} \sum_{q \geq q_{thr}}^{\infty} A_q(\omega, \gamma^{(i)}), \end{aligned} \quad (5.26)$$

$$F_0^{(i)} = F_0 g(\gamma^{(i)}), \quad (5.27)$$

for $i = 0$. The Kronecker deltas ensure a correct summation over the magnetic quantum number m for $\ell \leq 1$ so that the total ionization rate (5.23) results as

$$\begin{aligned} w^{\text{PPT}}(t) &= \left[\kappa_0^{(0)} \left(\frac{F_0^{(0)}}{E(t)} \right)^{g_0+1} + 2\kappa_1^{(0)} \left(\frac{F_0^{(0)}}{E(t)} \right)^{g_1+1} \right] e^{-\frac{F_0^{(0)}}{E(t)}}, \\ &= \left[\kappa_0^{(0)} + 2\kappa_1^{(0)} \left(\frac{F_0^{(0)}}{E(t)} \right)^{-1} \right] \left(\frac{F_0^{(0)}}{E(t)} \right)^{g_0+1} e^{-\frac{F_0^{(0)}}{E(t)}}, \\ &\approx \left[\kappa_0^{(0)} + 2\kappa_1^{(0)} \left(\frac{F_0^{(0)}}{E_0^{(0)}} \right)^{-1} \right] \left(\frac{F_0^{(0)}}{E(t)} \right)^{g_0+1} e^{-\frac{F_0^{(0)}}{E(t)}}, \end{aligned} \quad (5.28)$$

$$\kappa^{(0)} = \kappa_0^{(0)} + 2\kappa_1^{(0)} \left(\frac{F_0^{(0)}}{E_0^{(0)}} \right)^{-1}, \quad (5.29)$$

$$\Rightarrow w^{\text{PPT}}(t) \approx \kappa^{(0)} \left(\frac{F_0^{(0)}}{E(t)} \right)^{g_0+1} e^{-\frac{F_0^{(0)}}{E(t)}}. \quad (5.30)$$

Note that the inversion symmetry applies in the summation over the magnetic quantum number with $w_1^{\text{PPT}}(t) = w_{-1}^{\text{PPT}}(t)$. Furthermore, the temporal contribution of the electric field $E(t)$, within rectangular brackets, is assumed to be small while moving from the second to the third line. The electric field strength is, in addition, approximated by the critical electric field strength $E_0^{(0)} = \sqrt{I_c^{(0)}}$. It can be seen that the mathematical structure of Eq. (5.30) is similar to the integrand in Eq. (5.14). Making use of the presented calculation technique in Sec. (5.1.2) then yields the critical intensity calculated

within the PPT theory as

$$I_c^{(1)}(\tau, I_p, \lambda) = \left[\frac{g_0}{F_0^{(0)}} W_0 \left(-\frac{1}{g_0} \left(\frac{D^{(0)}}{\tau} \right)^{1/g_0} \right) \right]^{-2}, \quad \text{for } g_0 < 0, \quad (5.31a)$$

$$I_c^{(1)}(\tau, I_p, \lambda) = \left[\frac{g_0}{F_0^{(0)}} W_{-1} \left(-\frac{1}{g_0} \left(\frac{D^{(0)}}{\tau} \right)^{1/g_0} \right) \right]^{-2}, \quad \text{for } g_0 > 0. \quad (5.31b)$$

$$D^{(0)} = 2\sqrt{2\ln(2)} \frac{|\ln(1 - \eta_c)|}{\kappa^{(0)}}. \quad (5.31c)$$

Note that Eq. (5.31) incorporates contributions associated with magnetic quantum numbers $m = \pm 1$ as it can not be neglected here.² The scaling behavior of the critical intensity $I_c^{(1)}$ is more complex than that of $I_c^{(0)}$ (5.9) since the parameters $F_0^{(0)}$ and $\kappa^{(0)}$ both depend on the critical intensity within ADK theory $I_c^{(0)}$. Therefore, one may hardly see any general scaling behavior. However, the general behavior of $I_c^{(1)}$ (or η^{PPT}) should not differ substantially from $I_c^{(0)}$ (or η^{ADK}) since the computation technique is based on a perturbative approach. The similarity can be recognized by comparing ADK and PPT ionization rates for small Keldysh parameters, see [139]. This implies that the dependence of the parameters $\kappa^{(0)}$ and $F_0^{(0)}$ on the respective intensity should be sufficiently small for Keldysh parameters close to one. A further application of the demonstrated method increases the accuracy of the critical intensity and, in addition, yields valid results for Keldysh parameters of $\gamma \gtrsim 1$.

$$\begin{aligned} \gamma(I_c^{(0)}) &\equiv \gamma^{(0)} \rightarrow \gamma(I_c^{(1)}) \equiv \gamma^{(1)}, \\ \Rightarrow F_0^{(0)} &\rightarrow F_0^{(1)}; D^{(0)} \rightarrow D^{(1)}; I_c^{(1)} \rightarrow I_c^{(2)}. \end{aligned} \quad (5.32)$$

In fact, an iterative application of this procedure provides the $(i + 1)$ -th critical intensity in the i -th iteration step via

$$I_c^{(i+1)}(\tau, I_p, \lambda) = \left[\frac{g_0}{F_0^{(i)}} W_0 \left(-\frac{1}{g_0} \left(\frac{D^{(i)}}{\tau} \right)^{1/g_0} \right) \right]^{-2}, \quad \text{for } g_0 < 0, \quad (5.33a)$$

$$I_c^{(i+1)}(\tau, I_p, \lambda) = \left[\frac{g_0}{F_0^{(i)}} W_{-1} \left(-\frac{1}{g_0} \left(\frac{D^{(i)}}{\tau} \right)^{1/g_0} \right) \right]^{-2}, \quad \text{for } g_0 > 0. \quad (5.33b)$$

$$D^{(i)} = 2\sqrt{2\ln(2)} \frac{|\ln(1 - \eta_c)|}{\kappa^{(i)}}, \quad \kappa^{(i)} = \kappa_0^{(i)} + 2\kappa_1^{(i)} \frac{E_0^{(i)}}{F_0^{(i)}}. \quad (5.33c)$$

²The derivation only assumes Def. 5.1(i)-(ii) to compute the critical intensity within the PPT theory.

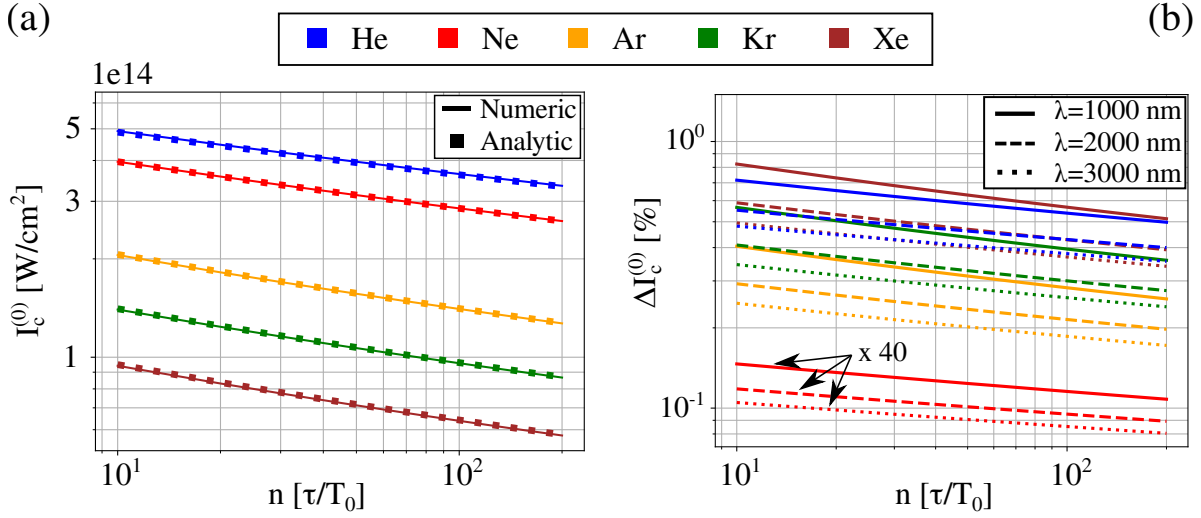


Figure 5.3.: (a) The critical intensity, computed as a function of the pulse duration which is measured in multiples of the optical period. The ionization rates are computed within the ADK model for a wavelength of $\lambda = 1000$ nm in neutrally charged noble gases (color). (b) The error of the analytic solution compared to the numerical computations for wavelengths of $\lambda = 1000, 2000, 3000$ nm (line type) in neutrally charged noble gases (line color).

This procedure is applied until the critical intensity has converged. Typically, convergence is achieved for $i \in [2, 8]$, which depends on the parameters (τ, I_p, λ) .

5.2. Results and Discussion

The following section discusses the accuracy of the derived analytical formulas concerning the critical intensity and the closely related Keldysh parameter. Moreover, it presents the parameter space for which the derived formulas of the critical intensity are valid. To do so, three quantities are defined to measure the respective errors

$$\Delta I_c^{(0)} = \frac{|I_c^{(0)} - I_c^{\text{ADK}}|}{I_c^{\text{ADK}}}, \quad (5.34)$$

$$\Delta I_c^{(i)} = \frac{|I_c^{(i)} - I_c^{\text{PPT}}|}{I_c^{\text{PPT}}}, \quad \text{for } i > 0, \quad (5.35)$$

$$\Delta \gamma^{(i)} = \frac{|\gamma^{(i)} - \gamma^{\text{PPT}}|}{\gamma^{\text{PPT}}}, \quad \text{for } i > 0, \quad (5.36)$$

where the first two errors indicate the modulus of the difference between the exact numerical solution of the critical intensity (I_c^{ADK} and I_c^{PPT}) and their analytic approximations

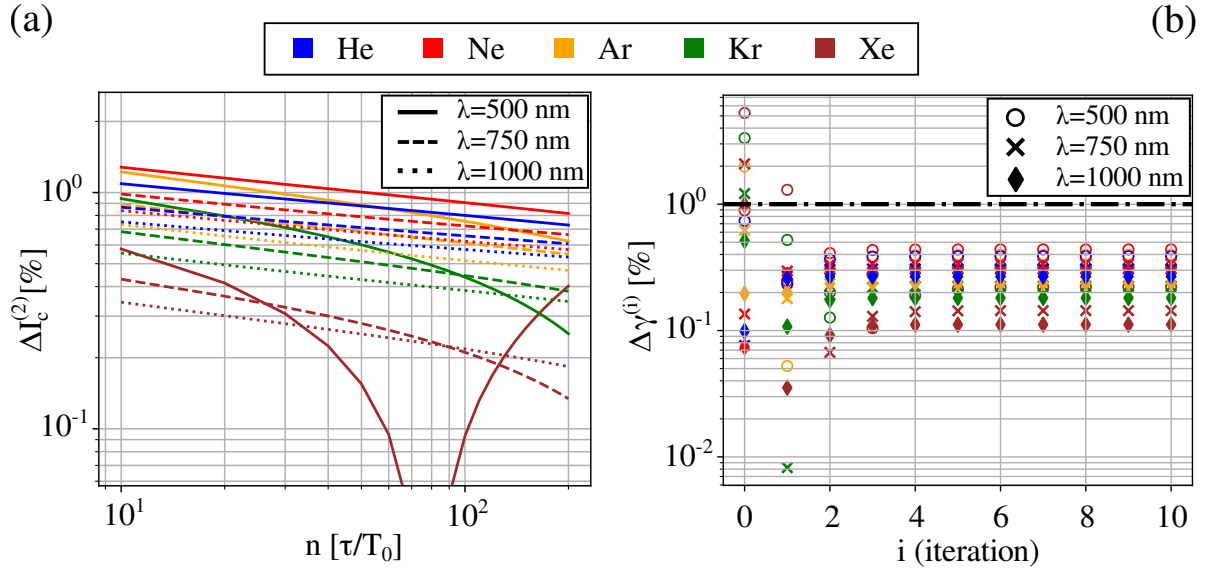


Figure 5.4.: (a) The error of the critical intensity as a function of the pulse duration was calculated within the PPT model. The error is shown for wavelengths of $\lambda = 500, 750, 1000$ nm (line type) in neutrally charged noble gases (line color). (b) The error of the Keldysh parameter for a pulse of $n = 200$ optical periods about the number of iterations i . The set of wavelengths (marker style) and noble gases (line color) is the same as in (a).

$I_c^{(0)}$ and $I_c^{(i)}$, respectively. The last error in Eq. (5.33) verifies the convergence of the Keldysh parameter, by the respective error of the numerical and analytical computation. All computations are performed for an HH photon energy of 25 eV unless stated otherwise. Different atomic species are visually distinguished by different line colors, whereas the respective marker or line type distinguishes different incident wavelengths.

5.2.1. Accuracy of the critical intensity: ADK theory

The accuracy of Eq. (5.9) is initially verified by visual comparison with the numerically calculated critical intensity. Figure 5.3a shows the critical intensity as a function of the number of optical periods $n = \tau/T_0$, while the wavelength of the incident laser pulse is fixed to $\lambda = 1000$ nm. Moreover, the line color denotes the atomic species, where the colored squares represent the analytical results of Eq. (5.9), and the solid line the numerical results. The error of the critical intensity (5.34) for a set of wavelengths $\lambda = 1000, 2000, 3000$ nm (line type) and noble gases (line color) is shown in Figure 5.3b since the difference between the numerical and analytical results is hardly visible. The error lies below 1% for all parameter configurations, while it is not significantly sensitive

to the HH energy. The latter validates this error estimate for HH photon energies from 25 eV to 200 eV. Note that the upper limit is arbitrarily set to 200 eV; see Fig. 5.1b; where the critical ionization probability remains approximately constant for the mentioned laser pulse parameters. With this in mind, the upper limit easily extends to photon energies of 2 keV. Note that the error of the critical intensity decreases with an increasing wavelength of the incident laser pulse and further decreases exponentially with increasing pulse duration. In addition, the error decreases with an increasing ionization potential for all noble gases except helium. Helium does not have electrons within its p-orbital, in contrast to the other noble gases. This may lead to deviations in the accuracy since these electrons (with $m = \pm 1$) are omitted in the analytical computation for all noble gases.

However, the accuracy of Eq. (5.9) compared to a numerical computation is listed in Tab. D.1 for various configurations. Here, the shortest wavelength λ_{\min} and the smallest number of optical periods n_{\min} is shown for which the error is smaller than $\Delta I_c^{(0)}$. This holds for $n > n_{\min}$ and $\lambda > \lambda_{\min}$ since the error decreases for increasing n and λ . As a brief conclusion, the error of Eq. (5.9) obeys³

$$\tau \geq 20 \text{ fs} , \lambda \geq 800 \text{ nm} , n \geq 8 \Rightarrow \Delta I_c^{(0)} \leq 1.0\%. \quad (5.37)$$

The ADK theory is generally not valid for wavelengths below 800 nm such that the results within the respective PPT theory are discussed in the following.

5.2.2. Accuracy of the critical intensity: PPT theory

Going on to shorter wavelengths of the laser pulse leads to the intermediate regime in which tunnel and multiphoton ionization simultaneously occur. In this regime, the critical intensity within the PPT theory is valid, as the Keldysh parameter is on the order of unity. If not mentioned otherwise, Eq. (5.33) is used to compute the critical intensity where i is chosen so that the Keldysh parameter converges.

Figure 5.4a shows the error of the critical intensity (5.33) for $i = 2$, similar to Figure 5.3b. In contrast to 5.3b, the error of heavy noble gases like krypton and xenon deviates from the exponential decrease with increasing pulse duration. In addition, the error gets fairly large for long pulse durations. This deviation is associated with the number of iteration steps i in (5.33). Since the approximate critical Keldysh parameter $\gamma_c^{(i)}$ gets

³Holds for all noble gases.

larger for small ionization potentials, as in the case of krypton and xenon, the number of iterations needs to increase. Figure 5.4b shows the convergence of the Keldysh parameter with iteration steps i on the x-axis and the error of the Keldysh parameter on the y-axis for a fixed pulse duration $\tau = 200T_0$. The iteration step $i = 0$ computes the Keldysh parameter within the ADK theory; see Eq. (5.24). The Keldysh parameter converges rapidly as iteration steps i and the wavelengths of $\lambda = 500, 750, 1000$ nm (marker type) increase, to an error of less than 1%.

The error is not significantly sensitive to the energy of the HH photon, so it is neglected here, while Tab. D.2 lists the accuracy of the critical intensity in the PPT model for various configurations. Overall the accuracy of Eq. (5.33) obeys ⁴

$$\tau \geq 8.3 \text{ fs} , \lambda \geq 250 \text{ nm} , n \geq 10 \Rightarrow \Delta I_c^{(i)} \leq 2.5\%, \quad (5.38)$$

$$\tau \geq 8.6 \text{ fs} , \lambda \geq 515 \text{ nm} , n \geq 5 \Rightarrow \Delta I_c^{(i)} \leq 1.5\%, \quad (5.39)$$

$$\tau \geq 26.7 \text{ fs} , \lambda \geq 800 \text{ nm} , n \geq 10 \Rightarrow \Delta I_c^{(i)} \leq 1.0\%. \quad (5.40)$$

5.2.3. Comparison of the critical intensities: ADK - PPT

The interpretation of the respective critical intensities is discussed in the following section. The focus lies on the general scaling of the critical intensity with respect to the pulse duration and incident wavelength. Figures 5.5 shows two density plots of the critical intensity $I_c^{(i)}(\lambda, \tau)$ (color scale) in which the variation of the wavelength corresponds to the horizontal axis and the variation of the pulse duration to the vertical axis. Figures 5.5a and b show the critical intensity of argon within ADK- and PPT theory, respectively. Especially the critical intensity within the ADK theory constantly increases with shrinking wavelengths and pulse durations. This is highlighted by the contour lines (solid) that denote parameter compositions (λ, τ) with constant critical intensity. In fact, these lines represent the solutions of Eq. (5.12) inserted into $I_c^{(i)}(\lambda, \tau)$. The pulse duration scaling matches well with the analytic approximation in Eq. (5.13), while the wavelength scaling is related to the critical ionization probability, which does not have a closed form. As mentioned above, Figure 5.5b shows the critical intensity in the PPT theory. The scaling of the critical intensity in the dashed inset matches well with the ADK theory so that both contour lines are straight. However, outside of the

⁴Holds for all noble gases.

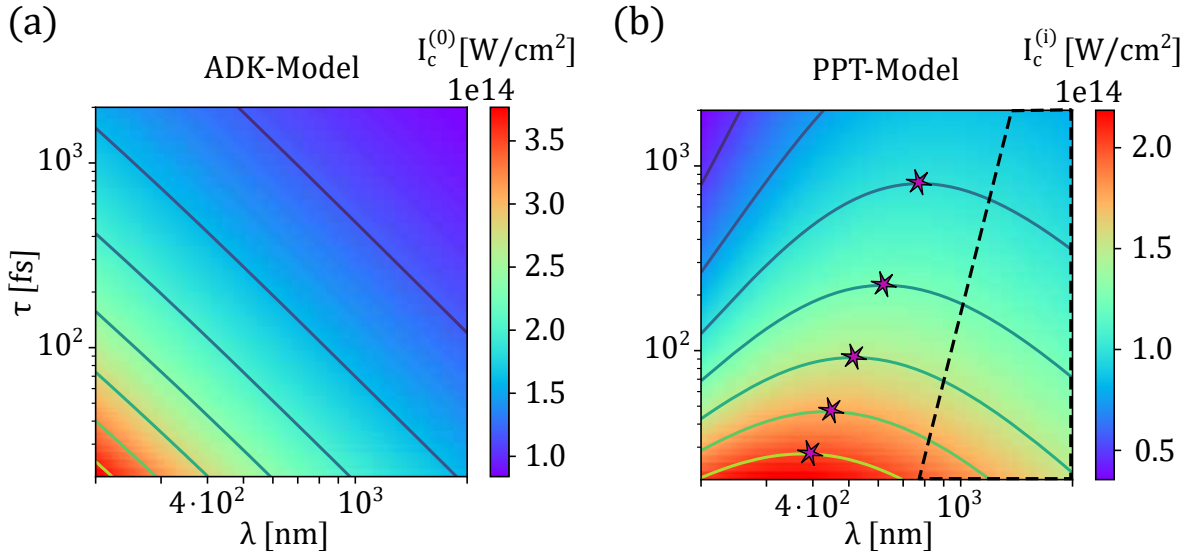


Figure 5.5.: Critical intensity in argon computed within the ADK model a), and the PPT model for iteration step $i = 8$ b). The critical intensity is shown for a incident wavelength from $\lambda = 200 - 2000$ nm and a pulse duration of $\tau = 40 - 2000$ fs. The inset in b) denotes the parameter space for which the critical intensity calculated within the PPT model scales similar (approximately linear contour lines) to the critical intensity calculated by the ADK model a).

inset, the scaling changes drastically. The deviation is remarkable since the global scaling changes rapidly, which is visualized by the purple stars to the left of the dashed inset. The position of these stars is understood as follows.

Let us select an arbitrary pair of parameters (λ_0, τ_0) in the dashed inset. Constantly decreasing the wavelength, while keeping the pulse duration constant, leads to a monotonic increase in the critical intensity. At a specific wavelength, the critical intensity is constant and will decrease afterward. The purple star denotes the wavelength $\tilde{\lambda}$ at which the intensity remains constant such that it describes the transition between two separated regimes. The first regime, in which the critical intensity increases for decreasing wavelengths, and the second, where the critical intensity decreases with decreasing wavelength. Even though the number of purple stars shown in Figure 5.5b is finite, they generally represent a continuous line that separates both regimes. From a pragmatic point of view, this may be stated as follows. Purple stars denote the highest critical intensity that can be applied to generate phase-matched high-order harmonics for a given pulse duration τ .

5.2.4. Comparison of the computation time: Analytical - Numerical

The following section compares the performance of the analytical and numerically computed critical intensity. Explicitly, two pulse durations are considered, namely $n = 20 \tau/T_0$ and $n = 100 \tau/T_0$, while the following parameters are fixed: $\lambda = 1000 \text{ nm}$; $I_p = 15.76 \text{ eV}$ (Ar: $\ell = 1$) and $\eta_c = 0.02$ for $E_q > 100 \text{ eV}$. The following computations are performed for the critical intensity in the ADK theory, while general remarks concerning the PPT theory are presented at the end. Numerical computations were executed in the Julia programming language [8], which utilizes the package QuadGK [140] for numerical integration while the package NLSolve [141] provides the root-finding algorithm. The resulting computation times $t_A(n)$ and $t_N(n)$ denote the analytical and numerical computation, respectively. The *average* computation time for $n = 20 \tau/T_0$ results as $t_A(20) = 736 \text{ ns}$, while the numerical computation yields $t_N(20) = 830 \cdot 10^5 \text{ ns}$. Therefore, the analytical method is roughly 10^5 times faster than the numerical computation. Moreover, the analytical model is roughly 10^6 times faster for pulse durations of $n = 100 \tau/T_0$ with computation times $t_A(100) = 725 \text{ ns}$ and $t_N(100) = 447 \cdot 10^6 \text{ ns}$. This drastically improved computation time highlights the relevance of the developed approach for more advanced investigations. The computation time ratio for the respective critical intensity within the PPT theory is given with 10^4 to 10^5 . The ratio is approximately one order of magnitude lower than the ratio for the critical intensity within the ADK theory, which may originate from the iterative application of the critical intensity in Eq. (5.33). The data shown in Fig. 5.5b were computed with the analytic expressions of the critical intensity in the PPT theory (5.33). The computation time for this 1000×1000 data grid (wavelength and the pulse duration) is on average 97 s while a numerical algorithm, as defined below Eq. (5.8), would need approximately $97 \text{ s} \cdot 10^4 = 270 \text{ h}$, or in other words, 11 days for the same computation.

5.3. Outlook: Negligible ionization in noble gases

This section demonstrates the potential application of the derived approximation of the critical intensity. There exist many examples for which the derived approximation is useful, such as the efficiency scaling of the single-atom response for phase-matched HHG [132] or simulations on HHG with finite ground-state depletion [63]. However, in some cases, it is necessary to determine an upper-parameter limit for which a laser field

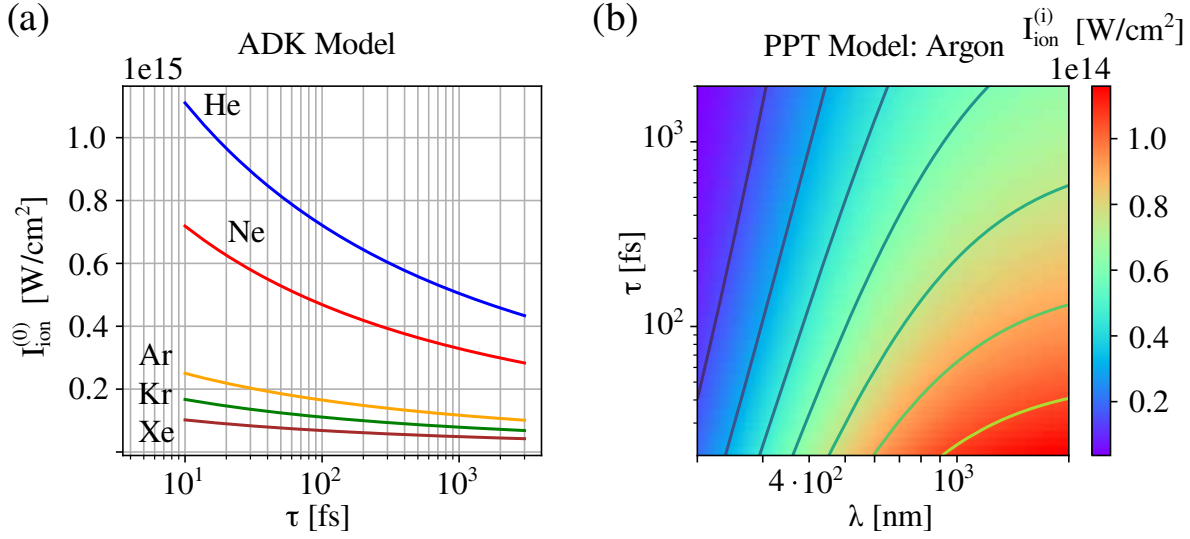


Figure 5.6.: Ionization intensity: (a) ADK theory for a set of noble gases and pulse durations of $\tau = 10 - \tau_{max} = 3000$ fs and, (b) the PPT theory for wavelengths of $\lambda = 200 - 2000$ nm and pulse durations of $\tau = 20 - 2000$ fs.

does not significantly ionize the gas medium. One example is nonlinear pulse compression. In this technique spectral phase modulation is used to broaden the spectrum of an initial pulse, which can be compressed down to the single cycle limit [142], using e.g. chirped mirrors. Hence, leading to a peak power enhancement. This is the state-of-the-art compression technique to generate ultrashort pulses with average powers in the kilowatt regime [143]. An essential parameter of this compression technique is the ionization of the gas medium, which should be small $\eta_0 = 0.001$ [144]. The developed formalism provides an analytic expression of an upper intensity, the ionization threshold intensity or *ionization intensity* $I_{\text{ion}}^{(0)}$, for which no significant ionization in the medium occurs. The ionization intensity is obtained by replacing the critical ionization probability η_c with the upper ionization limit η_0 . The ionization intensity, within ADK theory, is analogously defined to Eq. (5.9), via

$$I_{\text{ion}}^{(0)}(\tau, I_p) = \left[\frac{g_0}{F_0} W_0 \left(-\frac{1}{g_0} \left(\frac{D_0}{\tau} \right)^{1/g_0} \right) \right]^{-2}, \quad \text{for } g_0 < 0, \quad (5.41)$$

$$I_{\text{ion}}^{(0)}(\tau, I_p) = \left[\frac{g_0}{F_0} W_{-1} \left(-\frac{1}{g_0} \left(\frac{D_0}{\tau} \right)^{1/g_0} \right) \right]^{-2}, \quad \text{for } g_0 > 0. \quad (5.42)$$

$$D_0 = 2\sqrt{2 \ln(2)} \frac{|\ln(1 - \eta_0)|}{\kappa_0}. \quad (5.43)$$

The ionization intensity does not depend on the respective wavelength in contrast to the critical intensity in Eq. (5.9). The wavelength dependence of the critical intensity is

explicitly associated with the critical ionization probability $\eta_c(\lambda)$ and vanishes as it is replaced. Therefore, the ionization intensity does not depend on the wavelength of the incident laser pulse. This feature is physically reasonable since multiphoton ionization, in which the wavelength determines the photon energy, is neglected within the ADK theory. The respective ionization intensity is illustrated in Fig. 5.5a for several noble gases. However, the wavelength independence vanishes for the ionization intensity within the PPT theory. The respective formula is deduced similarly from the critical intensity within the PPT theory (5.33) as follows

$$I_{ion}^{(i+1)}(\tau, I_p, \lambda) = \left[\frac{g_0}{F_0^{(i)}} W_0 \left(-\frac{1}{g_0} \left(\frac{D^{(i)}}{\tau} \right)^{1/g_0} \right) \right]^{-2}, \quad \text{for } g_0 < 0, \quad (5.44)$$

$$I_{ion}^{(i+1)}(\tau, I_p, \lambda) = \left[\frac{g_0}{F_0^{(i)}} W_{-1} \left(-\frac{1}{g_0} \left(\frac{D^{(i)}}{\tau} \right)^{1/g_0} \right) \right]^{-2}, \quad \text{for } g_0 > 0. \quad (5.45)$$

$$D^{(i)} = 2\sqrt{2 \ln(2)} \frac{|\ln(1 - \eta_0)|}{\kappa^{(i)}}. \quad (5.46)$$

The ionization intensity within the PPT theory is illustrated in Fig. 5.6b for an argon gas target, where it reveals a significant dependence on the incident lasers wavelength. The ionization intensity already varies substantially for wavelengths, $\lambda > 1000$ nm in contrast to the wavelength independence of the ADK ionization intensity. These deviations indicate the limitation of the ionization intensity within the ADK theory for practically the complete chosen parameter space in Fig. 5.6b. The ionization intensity within the PPT theory (5.33) is valid for the parameter space discussed, which allows further investigation. In particular, this will help to tailor the design of future short-wavelength compression schemes, which promise a high HHG conversion efficiency [58].

Overall, it was demonstrated that the developed formalism can be adapted to similar tasks and is not limited to PM. The analytical computation technique provides an accurate and flexible tool for further investigation in the field of strong-field ionization and high-order harmonic generation.

CHAPTER 6.

SUMMARY AND CONCLUSION

“A physicist is just an atom’s way of looking at itself.”

— Niels Bohr

This dissertation investigates high-order harmonic generation within the weakly relativistic regime. The developed approach (GN-SFA) represents an extension of the widely used dipole SFA and incorporates weakly relativistic contributions of arbitrarily spatially structured light fields. Moreover, this dissertation investigates phase-matched HHG and provides an analytical expression of the critical intensity, which is compared to the respective numerical results. The findings of each chapter are briefly summarized in the following.

Chapter 2 reviews the Maxwell equations, which include the electrodynamics of light, followed by a general definition of spatially structured light fields. The chapter starts with a discussion on plane waves, as a specific solution of the Maxwell equations, where parts of its mathematical expression are associated with the respective physical quantities. Then the focus shifts toward laser beams and pulses within the dipole approximation. Subsequently, a general vector potential is defined, which depicts a wide range of spatially structured light fields. Two examples are explicitly discussed, an elliptically polarized plane wave and a locally linearly polarized Bessel beam. The latter example is of particular interest, as Bessel beams are twisted light beams that carry orbital angular momentum which is directly associated with their spatial structure. Twisted light represents an attractive and innovative tool for probing laser-atom interactions as an alternative to ordinary plane waves.

Chapter 3 introduces the strong-field regime alongside various processes. The chapter begins with a general overview of light-matter interactions and converges rapidly toward strong-field processes. The first half of the chapter particularly considers strong-field

ionization and discusses different ionization mechanisms and their associated conditions. Here, the focus lies on tunnel and multiphoton ionization within the ADK and PPT theory. The second half of Chap. 3 focuses on the Lewenstein model of HHG and reviews the gauge invariance of the strong-field amplitude in many details due to its relevance for Chap. 4. Moreover, Chap. 3 reviews the quantum orbit approach, which significantly simplifies the expression of the atomic dipole moment. Here, the electron trajectories are associated with a finite ionization and recombination time, which yield a quasi-classical interpretation of the high-order harmonic process.

Chapter 4 discusses weakly relativistic effects in the context of high-order harmonic generation. These effects, also-known as nondipole effects, are a direct consequence of the incident laser field's spatial structure. A representative analysis of electrons in an intense laser field provides qualitative insight and an intuitive understanding of the electron dynamics within spatially structured light fields. Here, novel contributions in the electron dynamics appear where the nondipole Volkov phase is not limited to plane wave laser fields, as shown by B.Böning et.al [110]. This nondipole Volkov phase essentially enables the general extension of the dipole SFA toward the weakly relativistic regime. The derivation of this extension follows in three parts, where the first ensures the gauge covariance of the strong-field transition amplitude for spatially structured light fields, while the second introduces the weakly relativistic extension of the dipole matrix element. Finally, the saddle-point approximation within the weakly relativistic regime is described for a spatially structured vector potential in part three. In particular, these parts are associated with research work carried out during the doctoral program and were published in Ref. [1]. The resulting theoretical framework refers to as *generalized nondipole strong-field approximation* (GN-SFA), which is the main outcome of this chapter. Furthermore, this chapter investigates the generation of high-order harmonics by an elliptically polarized plane wave beam within the GN-SFA as an example. Finally, Bessel beams as potential candidates for novel nondipole features are highlighted in the outlook to motivate further investigations. Generally, the GN-SFA provides an opportunity to study complex laser fields and their associated weakly relativistic dynamics, which is impossible with current methods.

Chapter 5 focuses on the phase-matched generation of high-order harmonics, investigated in Ref. [2]. While phase-matching is affected by many parameters like the atomic species, the laser field, or the geometry of the experimental setup, an extensive contribution is associated with the ionization of the gas target. Contributions, apart from the ionization, may experimentally be compensated and nullified. Therefore, the ionization

of the macroscopic target uniquely determines the phase-matching condition. For such systems, a critical ionization probability exists, which defines the optimal ionization of the gas target at the peak of the laser pulse. The generated high-order harmonics are consequently emitted coherently and can constructively be superimposed. By utilizing the critical ionization probability, a corresponding intensity, the critical intensity, is defined that guarantees perfect phase-matching for arbitrary initial parameters. A laser pulse with critical intensity, therefore, achieves the critical ionization probability at the peak of the pulse. So far, this intensity has been computed, involving numerical expensive integration's and root-finding algorithms. Overall, Chap. 5 provides an approach that circumvents the numerical computation and yields a highly accurate analytical expression of the critical intensity. The critical intensity essentially depends on the duration of the laser pulse, its wavelength, and the atomic species. The analytical approach provides accurate results for a wide range of parameters with an error of less than 1%. The high accuracy of the developed expression degrades numerical computations to a redundant method for many practical purposes and, consequently, may replace them in many applications. It further provides the opportunity to theoretically investigate more complex systems since the computation time decreases roughly 4 to 6 orders of magnitude. The outlook of this chapter considers the ionization intensity as an example for further applications, to mention the general character of the developed computation technique.

The following conclusion highlights the results of this dissertation. Progress in physics relies on the interplay of experimental and theoretical investigations. Both approaches aim to gain insight into the fundamental dynamics of nature. Where experiments yield measured data, theoreticians shall provide vivid models to describe these data and explain the associated phenomena. However, this dissertation does not directly investigate specific phenomena but develops models and methods to describe various new features and phenomena in the context of strong-field physics. The first part of this dissertation extends the dipole strong-field approximation of high-order harmonic generation toward the nondipole regime. This generalization essentially incorporates weakly relativistic effects of, for example, twisted light beams. Weakly relativistic contributions are of particular interest, as the nontrivial spatial structure of the laser field eventually affects the dynamics of the high-order harmonic process at the microscopic scale. The second part of this dissertation is associated with method development in the context of phase-matched high-order harmonic generation. The critical ionization probability represents an upper ionization limit in gas targets, above which phase-matching of the high-order harmonics is impossible. So far, suitable beam parameters that ensure phase-matching

are computed numerically, which substantially increases the computational effort in many applications. The derived analytic expression provides the critical intensity from sets of arbitrarily chosen initial parameters, namely the pulse length and wavelength of the incident laser field alongside the atomic species. While the analytical approach bypasses numerical effort and also provides insight into the dependencies of the respective parameters.

The research discussed in this dissertation highlights the latest findings in strong-field physics and further improves the existing models and methods substantially. Therefore, it represents an important step toward a more detailed understanding of strong-field atomic physics.

APPENDIX A.

EIGENSTATES OF THE ENERGY OPERATOR

The action of the energy operator onto its respective energy eigenstate expands as

$$\hat{\mathcal{E}}(\mathbf{r}, t) |\Psi_n^\mathcal{E}\rangle = \left(\hat{\mathcal{H}}_0 + \frac{\hat{\mathbf{p}} \cdot \mathbf{A}(\mathbf{r}, t) + \mathbf{A}(\mathbf{r}, t) \cdot \hat{\mathbf{p}} + \mathbf{A}^2(\mathbf{r}, t)}{2} \right) e^{-i\mathbf{r} \cdot \mathbf{A}(\mathbf{r}, t)} |\Psi_n\rangle. \quad (\text{A.1})$$

For the sake of simplicity, the spatial and temporal dependencies of the quantities will be abandoned in the following derivation. The expansion of the energy operator is simplified by assuming that the vector potential satisfies the Coulomb gauge (2.4)

$$\hat{\mathcal{E}} |\Psi_n^\mathcal{E}\rangle = \left(\hat{\mathcal{H}}_0 + \mathbf{A} \cdot \hat{\mathbf{p}} + \frac{\mathbf{A}^2}{2} \right) e^{-i\mathbf{r} \cdot \mathbf{A}} |\Psi_n\rangle. \quad (\text{A.2})$$

Even though the momentum operator and the exponential do not commute, they can be represented via

$$\hat{\mathbf{p}} e^{-i\mathbf{r} \cdot \mathbf{A}} |\Psi_n\rangle = e^{-i\mathbf{r} \cdot \mathbf{A}} (\hat{\mathbf{p}} - \mathbf{A}) |\Psi_n\rangle. \quad (\text{A.3})$$

With this in mind, the action of the field-free Hamiltonian onto the energy eigenstate is written as

$$\begin{aligned} \hat{\mathcal{H}}_0 |\Psi_n^\mathcal{E}\rangle &= \left(\frac{\hat{\mathbf{p}}^2}{2} + V(\mathbf{r}) \right) e^{-i\mathbf{r} \cdot \mathbf{A}} |\Psi_n\rangle = e^{-i\mathbf{r} \cdot \mathbf{A}} \left(\frac{(\hat{\mathbf{p}} - \mathbf{A})^2}{2} + V(\mathbf{r}) \right) |\Psi_n\rangle, \\ &= e^{-i\mathbf{r} \cdot \mathbf{A}} \left(\hat{\mathcal{H}}_0 - \mathbf{A} \cdot \hat{\mathbf{p}} + \frac{\mathbf{A}^2}{2} \right) |\Psi_n\rangle, \\ &= \left(\epsilon_n + \frac{\mathbf{A}^2}{2} \right) |\Psi_n^\mathcal{E}\rangle - e^{-i\mathbf{r} \cdot \mathbf{A}} \mathbf{A} \cdot \hat{\mathbf{p}} |\Psi_n\rangle, \\ &= \left(\epsilon_n + \frac{\mathbf{A}^2}{2} - \mathbf{A} (\hat{\mathbf{p}} + \mathbf{A}) \right) |\Psi_n^\mathcal{E}\rangle, \\ \Rightarrow \hat{\mathcal{H}}_0 |\Psi_n^\mathcal{E}\rangle &= \left(\epsilon_n - \mathbf{A} \cdot \hat{\mathbf{p}} - \frac{\mathbf{A}^2}{2} \right) |\Psi_n^\mathcal{E}\rangle. \end{aligned} \quad (\text{A.4})$$

Inserting Eq. (A.4) into Eq. (A.1) yields

$$\begin{aligned}\hat{\mathcal{E}}|\Psi_n^\epsilon\rangle &= \left(\epsilon_n + \underbrace{\mathbf{A} \cdot \hat{\mathbf{p}} - \mathbf{A} \cdot \hat{\mathbf{p}}}_{=0} + \underbrace{\frac{\mathbf{A}^2}{2} - \frac{\mathbf{A}^2}{2}}_{=0} \right) |\Psi_n^\epsilon\rangle, \\ \Rightarrow \hat{\mathcal{E}}|\Psi_n^\epsilon\rangle &= \epsilon_n |\Psi_n^\epsilon\rangle,\end{aligned}\tag{A.5}$$

which coincides with Eq. (4.8).

APPENDIX B.

NONDIPOLE VOLKOV STATES

General nondipole Volkov phase

The complete nondipole Volkov phase in terms of Eq. (4.5) is defined as

$$\Gamma(\mathbf{r}, t) = \sum_{i=1}^5 \Gamma_i(\mathbf{r}, t), \quad (\text{B.1a})$$

$$\Gamma_1(\mathbf{r}, t) = \int d^3\mathbf{k} \rho_k \sin(u_k + \theta_k), \quad (\text{B.1b})$$

$$\Gamma_2(\mathbf{r}, t) = \int d^3\mathbf{k} d^3\mathbf{k}' \left(\alpha_{\mathbf{k}\mathbf{k}'}^+ \sin(u_k + u_{\mathbf{k}'} + \theta_{\mathbf{k}\mathbf{k}'}^+) + \alpha_{\mathbf{k}\mathbf{k}'}^- \sin(u_k - u_{\mathbf{k}'} + \theta_{\mathbf{k}\mathbf{k}'}^-) \right), \quad (\text{B.1c})$$

$$\Gamma_3(\mathbf{r}, t) = \sum_{\pm} \frac{1}{2} \int d^3\mathbf{k} d^3\mathbf{k}' \sigma_{\mathbf{k}\mathbf{k}'} \rho_k \frac{\sin(u_k \pm u_{\mathbf{k}'} + \theta_k \pm \zeta_{\mathbf{k}\mathbf{k}'})}{\eta_k \pm \eta_{\mathbf{k}'}} , \quad (\text{B.1d})$$

$$\Gamma_4(\mathbf{r}, t) = \sum_{\pm} \int d^3\mathbf{k} d^3\mathbf{k}' d^3\mathbf{k}'' \sigma_{\mathbf{k}\mathbf{k}'} \alpha_{\mathbf{k}\mathbf{k}''}^+ \left(\frac{\sin(u_k \pm u_{\mathbf{k}'} + u_{\mathbf{k}''} + \theta_{\mathbf{k}\mathbf{k}''}^+ \pm \xi_{\mathbf{k}\mathbf{k}'})}{\eta_k \pm \eta_{\mathbf{k}'} + \eta_{\mathbf{k}''}} \right), \quad (\text{B.1e})$$

$$\Gamma_5(\mathbf{r}, t) = \sum_{\pm} \int d^3\mathbf{k} d^3\mathbf{k}' d^3\mathbf{k}'' \sigma_{\mathbf{k}\mathbf{k}'} \alpha_{\mathbf{k}\mathbf{k}''}^- \left(\frac{\sin(u_k \pm u_{\mathbf{k}'} - u_{\mathbf{k}''} + \theta_{\mathbf{k}\mathbf{k}''}^- \pm \xi_{\mathbf{k}\mathbf{k}'})}{\eta_k \pm \eta_{\mathbf{k}'} - \eta_{\mathbf{k}''}} \right), \quad (\text{B.1f})$$

where Eqs. (B.1b) and (B.1c) are associated with the particle-field and field-field contributions of the nondipole Volkov phase, respectively. Moreover, Eqs. (B.1d)-(B.1f) are interconnections of the geometric contribution with the respective particle-field and field-field contributions discussed below Eq. (4.5).

Spatial and temporal nondipole Volkov phase

The spatial nondipole Volkov phase is written in the following which is deduced from the approximation schema mentioned below Eq. 4.23,

$$\Gamma^{(r)}(t) = \sum_{i=1}^5 \Gamma_i^{(r)}(t), \quad (\text{B.2a})$$

$$\Gamma_1^{(r)}(t) = \int d^3\mathbf{k} \mathbf{k} \rho_{\mathbf{k}} \cos(u_{\mathbf{k}}^{(0)} + \theta_{\mathbf{k}}), \quad (\text{B.2b})$$

$$\Gamma_2^{(r)}(t) = \int d^3\mathbf{k} d^3\mathbf{k}' \left(\alpha_{\mathbf{k}\mathbf{k}'}^+ (\mathbf{k} + \mathbf{k}') \cos(u_{\mathbf{k}}^{(0)} + u_{\mathbf{k}'}^{(0)} + \theta_{\mathbf{k}\mathbf{k}'}^+) \right. \\ \left. + \alpha_{\mathbf{k}\mathbf{k}'}^- (\mathbf{k} - \mathbf{k}') \cos(u_{\mathbf{k}}^{(0)} - u_{\mathbf{k}'}^{(0)} + \theta_{\mathbf{k}\mathbf{k}'}^-) \right), \quad (\text{B.2c})$$

$$\Gamma_3^{(r)}(t) = \sum_{\pm} \frac{1}{2} \int d^3\mathbf{k} d^3\mathbf{k}' \sigma_{\mathbf{k}\mathbf{k}'} \rho_{\mathbf{k}} (\mathbf{k} \pm \mathbf{k}') \frac{\cos(u_{\mathbf{k}}^{(0)} \pm u_{\mathbf{k}'}^{(0)} + \theta_{\mathbf{k}} \pm \zeta_{\mathbf{k}\mathbf{k}'})}{\eta_{\mathbf{k}} \pm \eta_{\mathbf{k}'}} , \quad (\text{B.2d})$$

$$\Gamma_4^{(r)}(t) = \sum_{\pm} \int d^3\mathbf{k} d^3\mathbf{k}' d^3\mathbf{k}'' \sigma_{\mathbf{k}\mathbf{k}'} \alpha_{\mathbf{k}\mathbf{k}''}^+ (\mathbf{k} \pm \mathbf{k}' + \mathbf{k}'') \left(\frac{\cos(u_{\mathbf{k}}^{(0)} \pm u_{\mathbf{k}'}^{(0)} + u_{\mathbf{k}''}^{(0)} + \theta_{\mathbf{k}\mathbf{k}''}^+ \pm \xi_{\mathbf{k}\mathbf{k}'})}{\eta_{\mathbf{k}} \pm \eta_{\mathbf{k}'} + \eta_{\mathbf{k}''}} \right), \quad (\text{B.2e})$$

$$\Gamma_5^{(r)}(t) = \sum_{\pm} \int d^3\mathbf{k} d^3\mathbf{k}' d^3\mathbf{k}'' \sigma_{\mathbf{k}\mathbf{k}'} \alpha_{\mathbf{k}\mathbf{k}''}^- (\mathbf{k} \pm \mathbf{k}' - \mathbf{k}'') \left(\frac{\cos(u_{\mathbf{k}}^{(0)} \pm u_{\mathbf{k}'}^{(0)} - u_{\mathbf{k}''}^{(0)} + \theta_{\mathbf{k}\mathbf{k}''}^- \pm \xi_{\mathbf{k}\mathbf{k}'})}{\eta_{\mathbf{k}} \pm \eta_{\mathbf{k}'} - \eta_{\mathbf{k}''}} \right), \quad (\text{B.2f})$$

while the temporal nondipole Volkov phase reads

$$\Gamma^{(t)}(t) = \sum_{i=1}^5 \Gamma_i^{(t)}(t), \quad (\text{B.3a})$$

$$\Gamma_1^{(t)}(t) = \int d^3\mathbf{k} \rho_{\mathbf{k}} \sin(u_{\mathbf{k}}^{(0)} + \theta_{\mathbf{k}}), \quad (\text{B.3b})$$

$$\Gamma_2^{(t)}(t) = \int d^3\mathbf{k} d^3\mathbf{k}' \left(\alpha_{\mathbf{k}\mathbf{k}'}^+ \sin(u_{\mathbf{k}}^{(0)} + u_{\mathbf{k}'}^{(0)} + \theta_{\mathbf{k}\mathbf{k}'}^+) + \alpha_{\mathbf{k}\mathbf{k}'}^- \sin(u_{\mathbf{k}}^{(0)} - u_{\mathbf{k}'}^{(0)} + \theta_{\mathbf{k}\mathbf{k}'}^-) \right), \quad (\text{B.3c})$$

$$\Gamma_3^{(t)}(t) = \sum_{\pm} \frac{1}{2} \int d^3\mathbf{k} d^3\mathbf{k}' \sigma_{\mathbf{k}\mathbf{k}'} \rho_{\mathbf{k}} \frac{\sin(u_{\mathbf{k}}^{(0)} \pm u_{\mathbf{k}'}^{(0)} + \theta_{\mathbf{k}} \pm \zeta_{\mathbf{k}\mathbf{k}'})}{\eta_{\mathbf{k}} \pm \eta_{\mathbf{k}'}} , \quad (\text{B.3d})$$

$$\Gamma_4^{(t)}(t) = \sum_{\pm} \int d^3\mathbf{k} d^3\mathbf{k}' d^3\mathbf{k}'' \sigma_{\mathbf{k}\mathbf{k}'} \alpha_{\mathbf{k}\mathbf{k}''}^+ \left(\frac{\sin(u_{\mathbf{k}}^{(0)} \pm u_{\mathbf{k}'}^{(0)} + u_{\mathbf{k}''}^{(0)} + \theta_{\mathbf{k}\mathbf{k}''}^+ \pm \xi_{\mathbf{k}\mathbf{k}'})}{\eta_{\mathbf{k}} \pm \eta_{\mathbf{k}'} + \eta_{\mathbf{k}''}} \right), \quad (\text{B.3e})$$

$$\Gamma_5^{(t)}(t) = \sum_{\pm} \int d^3\mathbf{k} d^3\mathbf{k}' d^3\mathbf{k}'' \sigma_{\mathbf{k}\mathbf{k}'} \alpha_{\mathbf{k}\mathbf{k}''}^- \left(\frac{\sin(u_{\mathbf{k}}^{(0)} \pm u_{\mathbf{k}'}^{(0)} - u_{\mathbf{k}''}^{(0)} + \theta_{\mathbf{k}\mathbf{k}''}^- \pm \xi_{\mathbf{k}\mathbf{k}'})}{\eta_{\mathbf{k}} \pm \eta_{\mathbf{k}'} - \eta_{\mathbf{k}''}} \right). \quad (\text{B.3f})$$

Elliptically polarized plane wave beam

Some important definitions concerning the nondipole Volkov phase of an elliptically polarized plane wave beam are defined in the following.

$$\begin{aligned} \mathbf{p}_0 \cdot \hat{\nabla}_{\mathbf{p}} \Gamma_1^{(p)}(t) \Big|_{\mathbf{p}=\mathbf{p}_0} &= -\mathbf{p}_0 \cdot \int^t d\tau \hat{\nabla}_{\mathbf{p}} \frac{\omega_{\mathbf{k}_0}}{\eta_{\mathbf{k}_0}} \mathbf{A}_{\mathbf{k}_0}(\tau) \Big|_{\mathbf{p}=\mathbf{p}_0} = \mathbf{k}_0 \int^t d\tau \frac{\omega_{\mathbf{k}_0}}{\eta_{\mathbf{k}_0}^2} (\mathbf{p}_0 \cdot \mathbf{A}_{\mathbf{k}_0}(\tau)) \Big|_{\mathbf{p}=\mathbf{p}_0} \\ &= \frac{\mathbf{k}_0}{\omega_{\mathbf{k}_0}} \int^t d\tau (\mathbf{p}_0 \cdot \mathbf{A}_{\mathbf{k}_0}(\tau)) \end{aligned} \quad (\text{B.4a})$$

$$\begin{aligned} \hat{\nabla}_{\mathbf{p}} \Gamma_2^{(t)}(t) \Big|_{\mathbf{p}=\mathbf{p}_0} &= -\int^t d\tau \hat{\nabla}_{\mathbf{p}} \frac{\omega_{\mathbf{k}_0}}{\eta_{\mathbf{k}_0}} \frac{\mathbf{A}_{\mathbf{k}_0}^2(\tau)}{2} \Big|_{\mathbf{p}=\mathbf{p}_0} = \int^t d\tau \mathbf{k}_0 \frac{\omega_{\mathbf{k}_0}}{\eta_{\mathbf{k}_0}^2} \frac{\mathbf{A}_{\mathbf{k}_0}^2(\tau)}{2} \Big|_{\mathbf{p}=\mathbf{p}_0} \\ &= \frac{\mathbf{k}_0}{\omega_{\mathbf{k}_0}} \int^t d\tau \frac{\mathbf{A}_{\mathbf{k}_0}^2(\tau)}{2} \end{aligned} \quad (\text{B.4b})$$

$$\Gamma_3^{(p)} = 0 \quad (\text{B.4c})$$

The respective saddle-point momentum reads as

$$\mathbf{p}_s = \mathbf{p}_0 - \frac{1}{t-t'} \frac{\mathbf{k}_0}{\omega_{\mathbf{k}_0}} \int_{t'}^t d\tau \left(\mathbf{p}_0 \cdot \mathbf{A}_{\mathbf{k}_0}(\tau) + \frac{1}{2} \mathbf{A}_{\mathbf{k}_0}^2(\tau) \right). \quad (\text{B.5})$$

APPENDIX C.

NONDIPOLE MATRIX ELEMENT

General nondipole Volkov phase

The nondipole matrix element is given via

$$\Upsilon(\mathbf{p}, t) = \mathbf{d}(\boldsymbol{\pi}(\mathbf{p}, t)) + \sum_j \hat{\partial}_\beta \hat{\partial}_\gamma \mathbf{d}(\boldsymbol{\pi}_{\beta\gamma}^j(\mathbf{p}, t)) \Big|_{\beta=\gamma=0} + \mathcal{O}(1/c^2), \quad (\text{C.1})$$

with momentum, $\boldsymbol{\pi}_{\beta\gamma}^j(\mathbf{p}, t) \equiv \mathbf{p} + \mathbf{A}(t) - \Gamma^{(r)}(t) + \beta \mathbf{k}_j + \gamma \mathbf{A}_{\mathbf{k}_j}^I(t)$. Here, β and γ represent dummy variables. The second term in the dipole momentum results as

$$\hat{\partial}_\beta \mathbf{d}(\boldsymbol{\pi}_{\beta\gamma}^j) \Big|_{\beta=\gamma=0} = \frac{2^{19/4} I_p^{5/4}}{\pi} \left(\frac{\mathbf{k}_j}{(\boldsymbol{\pi}^2 + 2I_p)^3} - 6 \frac{\boldsymbol{\pi}(\boldsymbol{\pi} \cdot \mathbf{k}_j)}{(\boldsymbol{\pi}^2 + 2I_p)^4} \right), \quad (\text{C.2})$$

$$\begin{aligned} \hat{\partial}_\beta \hat{\partial}_\gamma \mathbf{d}(\boldsymbol{\pi}_{\beta\gamma}^j) \Big|_{\beta=\gamma=0} = & - \frac{2^{19/4} I_p^{5/4}}{\pi} \\ & \times \left(\left(6 \frac{\mathbf{A}_{\mathbf{k}_j}^I(\boldsymbol{\pi} \cdot \mathbf{k}_j) + \mathbf{k}_j(\boldsymbol{\pi} \cdot \mathbf{A}_{\mathbf{k}_j}^I)}{(\boldsymbol{\pi}^2 + 2I_p)^4} - 48 \frac{\boldsymbol{\pi}(\boldsymbol{\pi} \cdot \mathbf{A}_{\mathbf{k}_j}^I)(\boldsymbol{\pi} \cdot \mathbf{k}_j)}{(\boldsymbol{\pi}^2 + 2I_p)^5} \right) \right), \end{aligned} \quad (\text{C.3})$$

where the contributions containing $\mathbf{k}_0 \cdot \mathcal{A}^I$ identically vanished in the Coulomb gauge. For simplicity, the dependencies of the variables were omitted and the shorthand notation $\boldsymbol{\pi} \equiv \boldsymbol{\pi}_{00}$ is used.

Elliptically polarized plane wave beam

In the scenario of an elliptically polarized plane wave beam, Eq. (4.34) reduces to

$$\boldsymbol{\pi}(\mathbf{p}, t) = \mathbf{p} + \mathbf{A}(t) - \frac{\mathbf{k}_0}{\eta_{\mathbf{k}_0}} \left(\mathbf{p} \cdot \mathbf{A}_{\mathbf{k}_0}(t) + \frac{1}{2} \mathbf{A}_{\mathbf{k}_0}^2(t) \right). \quad (\text{C.4})$$

Since the factor $\boldsymbol{\pi} \cdot \mathbf{k}_0 \approx 0$ approximately vanishes, the respective nondipole matrix element reads

$$\Upsilon(\mathbf{p}, t) = \mathbf{d}(\boldsymbol{\pi}(\mathbf{p}, t)) + 6i\mathbf{k}_0 \frac{\mathbf{d}(\boldsymbol{\pi}(\mathbf{p}, t)) \cdot \mathbf{A}_{\mathbf{k}_0}^I(t)}{\boldsymbol{\pi}^2(\mathbf{p}, t) + 2I_p}. \quad (\text{C.5})$$

Making use of $\mathbf{A}_{\mathbf{k}_0}^I(t) = \frac{1}{\omega_{\mathbf{k}_0}} \hat{\partial}_t \mathbf{A}_{\mathbf{k}_0}^R(t)$ (similar to Eq. (4.48)) and the definition of the electric field, $\mathbf{E}(t) = -\hat{\partial}_t \mathbf{A}_{\mathbf{k}_0}^R(t)$, yields

$$\Upsilon(\mathbf{p}, t) = \mathbf{d}(\boldsymbol{\pi}(\mathbf{p}, t)) - 6i \frac{\mathbf{k}_0}{\omega_{\mathbf{k}_0}} \frac{\mathbf{d}(\boldsymbol{\pi}(\mathbf{p}, t)) \cdot \mathbf{E}(t)}{\boldsymbol{\pi}^2(\mathbf{p}, t) + 2I_p}, \quad (\text{C.6})$$

while $\Lambda(t)$ vanishes.

APPENDIX D.

ACCURACY CRITICAL INTENSITY

Table D.1.: Accuracy of the critical intensity in the ADK theory (5.34). The table shows parameters $\lambda_{\min}, n_{\min}, \tau_{\min} \propto \lambda_{\min} n_{\min}$ (wavelength, number of optical cycles, pulse duration) for which the error of the critical intensity is smaller than $\Delta I_c^{(0)}$. Increasing these parameters leads to a decrease in the error. The HH photon energy is fixed to 50 eV so that the error of the critical intensity remains approximately constant for higher photon energies, while it changes only slowly for lower ones, see Figure 5.1b.

Element	λ_{\min} [nm]	n_{\min} [t/T_0]	τ_{\min} [fs]	$\Delta I_c^{(0)}$
He	800	7	18.7	$\leq 1.0\%$
	1600	10	53.4	$\leq 0.7\%$
	3200	5	53.4	$\leq 0.6\%$
Ne	800	3	8.0	$< 0.01\%$
	1600	3	16.0	$< 0.01\%$
	3200	3	32.0	$< 0.01\%$
Ar	800	3	8.0	$< 0.5\%$
	1600	3	16.0	$< 0.4\%$
	3200	3	32.0	$< 0.3\%$
Kr	800	4	10.7	$< 0.7\%$
	1600	4	21.4	$< 0.5\%$
	3200	4	42.7	$< 0.4\%$
Xe	800	5	13.3	$\leq 1.0\%$
	1600	5	26.7	$\leq 0.7\%$
	3200	5	53.4	$\leq 0.5\%$

Table D.2.: Accuracy of the critical intensity in the PPT theory (5.35). The table shows parameters $\lambda_{\min}, n_{\min}, \tau_{\min} \propto \lambda_{\min} n_{\min}$ (wavelength, number of optical cycles, pulse duration) for which the error of the critical intensity is smaller than $\Delta I_c^{(i)}$. The iteration parameter i is chosen so that the critical intensity converges. The HH photon energy is fixed to 50 eV so that the error of the critical intensity remains approximately constant for higher photon energies, while it changes only slowly for lower ones, see Figure 5.1b.

Element	λ_{\min} [nm]	n_{\min} [t/T_0]	τ_{\min} [fs]	$\Delta I_c^{(i)}$
He	250	5	4.2	$\leq 2.5\%$
	515	5	8.6	$< 1.5\%$
	800	10	26.7	$\leq 1.0\%$
Ne	250	9	7.5	$\leq 2.5\%$
	515	5	8.6	$\leq 1.5\%$
	800	8	21.4	$\leq 1.0\%$
Ar	250	10	8.3	$\leq 2.5\%$
	515	3	5.2	$\leq 1.5\%$
	800	4	10.7	$\leq 1.0\%$
Kr	250	5	4.2	$< 2.5\%$
	515	3	5.2	$< 1.5\%$
	800	3	8.0	$< 1.0\%$
Xe	250	3	2.5	$< 2.5\%$
	515	3	5.2	$< 1.0\%$
	800	3	8.0	$< 1.0\%$

BIBLIOGRAPHY

- [1] B. Minneker, B. Böning, and S. Fritzsche, *Phys. Rev. A* **106**, 053109 (2022).
- [2] B. Minneker, R. Klas, J. Rothhardt, and S. Fritzsche, *Photonics* **10**, 24 (2022).
- [3] B. Minneker, B. Böning, A. Weber, and S. Fritzsche, *Phys. Rev. A* **104**, 053116 (2021).
- [4] A. Weber, B. Böning, B. Minneker, and S. Fritzsche, *Phys. Rev. A* **104**, 063118 (2021).
- [5] D. F. Dar, B. Minneker, and S. Fritzsche, *Phys. Rev. A* **107**, 053102 (2023).
- [6] W. R. Inc., *Mathematica*, Version 12.1, Champaign, IL, 2020.
- [7] I. Project, *Inkscape* 0.92.5, 2020.
- [8] J. Bezanson, A. Edelman, S. Karpinski, and V. B. Shah, *SIAM review* **59**, 65 (2017).
- [9] E. T. Whittaker, *A history of the theories of aether and electricity from the age of Descartes to the close of the nineteenth century* (Longmans, Green, and Co., London, New York, Bombay, and Calcutta, 1910).
- [10] J. C. Maxwell, *Philosophical Transactions of the Royal Society of London* **155**, 459 (1865).
- [11] A. Einstein, *Annalen der Physik* **322**, 132 (1905).
- [12] M. Planck, *Annalen der Physik* **309**, 553 (1901).
- [13] E. Schrödinger, *Phys. Rev.* **28**, 1049 (1926).
- [14] P. A. M. Dirac and R. H. Fowler, *Proceedings of the Royal Society of London. Series A, Containing Papers of a Mathematical and Physical Character* **117**, 610 (1928).
- [15] W. Pauli, *Zeitschrift für Physik* **229**, 765 (1925).
- [16] L. Keldysh *et al.*, *Sov. Phys.-JETP* **47**, 1307 (1964).

-
- [17] A. McPherson *et al.*, J. Opt. Soc. Am. B **4**, 595 (1987).
- [18] B. Walker *et al.*, Phys. Rev. Lett. **73**, 1227 (1994).
- [19] M. Hentschel *et al.*, Nature **414**, 509 (2001).
- [20] P. B. Corkum and F. Krausz, Nature Physics **3**, 381 (2007).
- [21] F. Calegari, G. Sansone, S. Stagira, C. Vozzi, and M. Nisoli, J. Phys. B: At. Mol. **49**, 062001 (2016).
- [22] J. Itatani *et al.*, Phys. Rev. Lett. **88**, 173903 (2002).
- [23] M. W. Walser, C. H. Keitel, A. Scrinzi, and T. Brabec, Phys. Rev. Lett. **85**, 5082 (2000).
- [24] D. B. Milošević, S. Hu, and W. Becker, Phys. Rev. A **63**, 011403 (2000).
- [25] T. Popmintchev *et al.*, Science **336**, 1287 (2012).
- [26] P. Colosimo *et al.*, Nature Physics **4**, 386 (2008).
- [27] D. J. Griffiths, *Introduction to electrodynamics* (Pearson, 2013).
- [28] J. D. Jackson and R. F. Fox, *Classical Electrodynamics* (American Journal of Physics, 1999).
- [29] B. E. Saleh and M. C. Teich, *Fundamentals of photonics* (John Wiley & Sons, Ltd, 1991).
- [30] E. Pisanty *et al.*, New J. Phys. **20**, 053036 (2018).
- [31] S. Fritzsche and B. Böning, Phys. Rev. Res. **4**, 033031 (2022).
- [32] O. Matula, A. G. Hayrapetyan, V. G. Serbo, A. Surzhykov, and S. Fritzsche, J. Phys. B: At. Mol. **46**, 205002 (2013).
- [33] Z. Chang, *Fundamentals of attosecond optics* (CRC press, 2016).
- [34] D. Milošević, G. Paulus, D. Bauer, and W. Becker, J. Phys. B: At. Mol. **39**, R203 (2006).
- [35] L. Allen, M. W. Beijersbergen, R. J. C. Spreeuw, and J. P. Woerdman, Phys. Rev. A **45**, 8185 (1992).
- [36] D. L. Andrews and M. Babiker, *The angular momentum of light* (Cambridge

- University Press, 2012).
- [37] A. Afanasev *et al.*, *New J. Phys.* **20**, 023032 (2018).
- [38] A. Surzhykov, D. Seipt, V. Serbo, and S. Fritzsche, *Phys. Rev. A* **91**, 013403 (2015).
- [39] M. Ferray *et al.*, *J. Phys. B: At. Mol.* **21**, L31 (1988).
- [40] J. L. Krause, K. J. Schafer, and K. C. Kulander, *Phys. Rev. Lett.* **68**, 3535 (1992).
- [41] N. Burnett, H. Baldis, M. Richardson, and G. Enright, *Appl. Phys. Lett.* **31**, 172 (1977).
- [42] S. Ghimire and D. A. Reis, *Nature Physics* **15**, 10 (2019).
- [43] S. Ghimire *et al.*, *Nature Physics* **7**, 138 (2011).
- [44] R. Torres *et al.*, *Phys. Rev. Lett.* **98**, 203007 (2007).
- [45] P. Wernet, J. Gaudin, K. Godehusen, O. Schwarzkopf, and W. Eberhardt, *Rev. Sci. Instrum.* **82**, 063114 (2011).
- [46] D. Popmintchev *et al.*, *Phys. Rev. Lett.* **120**, 093002 (2018).
- [47] P. Moulton, *Optics News* **8**, 9 (1982).
- [48] P. F. Moulton, *J. Opt. Soc. Am. B* **3**, 125 (1986).
- [49] J. Geusic, H. Marcos, and L. Van Uitert, *Appl. Phys. Lett.* **4**, 182 (1964).
- [50] K. Amini *et al.*, *Rep. Prog. Phys.* **82**, 116001 (2019).
- [51] P. B. Corkum, *Phys. Rev. Lett.* **71**, 1994 (1993).
- [52] G. G. Paulus, W. Becker, W. Nicklich, and H. Walther, *J. Phys. B: At. Mol.* **27**, L703 (1994).
- [53] G. L. Yudin and M. Y. Ivanov, *Phys. Rev. A* **64**, 013409 (2001).
- [54] M. Gavrilin, *Atoms in intense laser fields* (Academic Press Inc, 1992).
- [55] M. V. Ammosov, N. B. Delone, and V. P. Krainov, *Sov. Phys. JETP* **64**, 1191 (1986).
- [56] A. Perelomov, V. Popov, and M. Terent'ev, *Sov. Phys. JETP* **23**, 924 (1966).

- [57] S. Larochelle, A. Talebpour, and S. Chin, *J. Phys. B: At. Mol.* **31**, 1215 (1998).
- [58] R. Klas *et al.*, *PhotonIX* **2**, 1 (2021).
- [59] A. Comby *et al.*, *Optics Express* **27**, 20383 (2019).
- [60] D. Popmintchev *et al.*, *Science* **350**, 1225 (2015).
- [61] R. Weissenbilder *et al.*, *Nat. Rev. Phys.* **4**, 713 (2022).
- [62] F. W. J. Olver *et al.*, *NIST Digital Library of Mathematical Functions* (<https://dlmf.nist.gov/>, Release 1.1.11 of 2023-09-15).
- [63] D. B. Milošević, *J. Opt. Soc. Am. B* **23**, 308 (2006).
- [64] E. A. Gibson *et al.*, *Phys. Rev. Lett.* **92**, 033001 (2004).
- [65] T. Popmintchev *et al.*, *Proceedings of the National Academy of Sciences* **106**, 10516 (2009).
- [66] A.-T. Le, H. Wei, C. Jin, and C. Lin, *J. Phys. B: At. Mol.* **49**, 053001 (2016).
- [67] D. M. Wolkow, *Zeitschrift für Physik* **94**, 250 (1935).
- [68] D. Bauer, D. Milošević, and W. Becker, *Phys. Rev. A* **72**, 023415 (2005).
- [69] Y.-C. Han and L. B. Madsen, *Phys. Rev. A* **81**, 063430 (2010).
- [70] W. Becker and D. Milošević, *Laser Physics* **19**, 1621 (2009).
- [71] M. Klaiber, K. Z. Hatsagortsyan, and C. H. Keitel, *Phys. Rev. A* **73**, 053411 (2006).
- [72] Y. V. Vanne and A. Saenz, *Phys. Rev. A* **79**, 023421 (2009).
- [73] Y. Aharonov and D. Bohm, *Phys. Rev.* **115**, 485 (1959).
- [74] K.-H. Yang, *Annals of Physics* **101**, 62 (1976).
- [75] S. Popruzhenko, *J. Phys. B: At. Mol.* **47**, 204001 (2014).
- [76] L. B. Madsen, *Phys. Rev. A* **65**, 053417 (2002).
- [77] M. O. Scully and M. S. Zubairy, *Quantum Optics* (Cambridge University Press, 1997).
- [78] C. Cohen-Tannoudji, J. Dupont-Roc, C. Fabre, and G. Grynberg, *Phys. Rev. A* **8**,

- 2747 (1973).
- [79] G. Grynberg and E. Giacobino, *J. Phys. B: At. Mol.* (1968-1987) **12**, L93 (1979).
- [80] C. Cohen-Tannoudji, B. Diu, and C. Laloë, *Quantum Mechanics* (Hermann/Wiley, 1977).
- [81] M. Lewenstein, P. Balcou, M. Y. Ivanov, A. L'Huillier, and P. B. Corkum, *Phys. Rev. A* **49**, 2117 (1994).
- [82] K. Kulander, K. Schafer, and J. Krause, *Dynamics of short-pulse excitation, ionization and harmonic conversion* (Springer US, 1993).
- [83] U. Gerlach, *Linear mathematics in infinite dimensions signals boundary value problems and special functions* (<http://people.math.osu.edu/gerlach.1/math/BVtypset>, 2015).
- [84] N. G. De Bruijn, *Asymptotic methods in analysis* (Courier Corporation, 1981).
- [85] N. Bleistein and R. A. Handelsman, *Asymptotic expansions of integrals* (Arden Media, 1975).
- [86] G. B. Arfken and H. J. Weber, *Mathematical methods for physicists* (American Association of Physics Teachers, 1999).
- [87] P. Salières *et al.*, *Science* **292**, 902 (2001).
- [88] P. Lacovara, H. Choi, C. Wang, R. Aggarwal, and T. Fan, *Optics Letters* **16**, 1089 (1991).
- [89] D. Milošević and W. Becker, *Phys. Rev. A* **66**, 063417 (2002).
- [90] E. Pisanty, M. F. Ciappina, and M. Lewenstein, *J. Phys. Photonics* **2**, 034013 (2020).
- [91] R. Haight and D. Peale, *Phys. Rev. Lett.* **70**, 3979 (1993).
- [92] D. J. Batey *et al.*, *Phys. Rev. Lett.* **126**, 193902 (2021).
- [93] N. J. Kylstra, R. Potvliege, and C. Joachain, *J. Phys. B: At. Mol.* **34**, L55 (2001).
- [94] D. B. Milošević, S. Hu, and W. Becker, *Laser Physics* **12**, 389 (2002).
- [95] X.-M. Tong and S.-I. Chu, *Phys. Rev. A* **57**, 452 (1998).

- [96] H. R. Reiss, Phys. Rev. A **22**, 1786 (1980).
- [97] D. J. Wilson *et al.*, Scientific Reports **9**, 1 (2019).
- [98] C. Chirilă, N. J. Kylstra, R. Potvliege, and C. Joachain, Phys. Rev. A **66**, 063411 (2002).
- [99] D. Habibović and D. B. Milošević, Phys. Rev. A **106**, 033101 (2022).
- [100] S. Brennecke and M. Lein, J. Phys. B: At. Mol. **51**, 094005 (2018).
- [101] M. Klaiber, K. Z. Hatsagortsyan, and C. H. Keitel, Phys. Rev. A **71**, 033408 (2005).
- [102] T. Keil and D. Bauer, J. Phys. B: At. Mol. **50**, 194002 (2017).
- [103] R. c. v. Kahvedžić and S. Gräfe, Phys. Rev. A **105**, 063102 (2022).
- [104] A. Hartung *et al.*, Phys. Rev. Lett. **126**, 053202 (2021).
- [105] P.-L. He, D. Lao, and F. He, Phys. Rev. Lett. **118**, 163203 (2017).
- [106] L. D. Landau, *The classical theory of fields* (Elsevier, 2013).
- [107] E. Sarachik and G. Schappert, Phys. Rev. D **1**, 2738 (1970).
- [108] H. Reiss, Phys. Rev. Lett. **101**, 043002 (2008).
- [109] H. Reiss, J. Phys. B: At. Mol. **47**, 204006 (2014).
- [110] B. Böning, W. Paufler, and S. Fritzsche, Phys. Rev. A **99**, 053404 (2019).
- [111] L. Rosenberg and F. Zhou, Phys. Rev. A **47**, 2146 (1993).
- [112] B. Böning, *Above-threshold ionization driven by spatially structured laser fields*, PhD thesis, Dissertation, Jena, Friedrich-Schiller-Universität Jena, 2020.
- [113] K. Krajewska and J. Kamiński, Phys. Rev. A **92**, 043419 (2015).
- [114] M. Klaiber, E. Yakaboylu, H. Bauke, K. Z. Hatsagortsyan, and C. H. Keitel, Phys. Rev. Lett. **110**, 153004 (2013).
- [115] N. J. Kylstra *et al.*, Phys. Rev. Lett. **85**, 1835 (2000).
- [116] M. W. Walser, C. H. Keitel, A. Scrinzi, and T. Brabec, Phys. Rev. Lett. **85**, 5082 (2000).

-
- [117] B. Wang *et al.*, J. Phys. B: At. Mol. **53**, 215601 (2020).
- [118] A. Hartung *et al.*, Nature Physics **15**, 1222 (2019).
- [119] B. Böning and S. Fritzsche, Phys. Rev. A **106**, 043102 (2022).
- [120] M.-C. Chen *et al.*, Proceedings of the National Academy of Sciences **111**, E2361 (2014).
- [121] A. Shiner *et al.*, Phys. Rev. Lett. **103**, 073902 (2009).
- [122] E. L. Falcao-Filho, V.-M. Gkortsas, A. Gordon, and F. X. Kärtner, Optics Express **17**, 11217 (2009).
- [123] V.-M. Gkortsas *et al.*, J. Phys. B: At. Mol. **44**, 045601 (2011).
- [124] E. Constant *et al.*, Phys. Rev. Lett. **82**, 1668 (1999).
- [125] P. Balcou and A. L’Huillier, Phys. Rev. A **47**, 1447 (1993).
- [126] C. Altucci *et al.*, J. Opt. Soc. Am. B **13**, 148 (1996).
- [127] T. Popmintchev, M.-C. Chen, P. Arpin, M. M. Murnane, and H. C. Kapteyn, Nature Photonics **4**, 822 (2010).
- [128] J. Rothhardt *et al.*, New J. Phys. **16**, 033022 (2014).
- [129] W. Paufler, B. Böning, and S. Fritzsche, Phys. Rev. A **100**, 013422 (2019).
- [130] J. Rothhardt *et al.*, New J. Phys. **16**, 033022 (2014).
- [131] P. Balcou, P. Salieres, A. L’Huillier, and M. Lewenstein, Phys. Rev. A **55**, 3204 (1997).
- [132] R. Klas, *Efficiency Scaling of High Harmonic Generation Using Ultrashort Fiber Lasers*, PhD thesis, Dissertation, Jena, Friedrich-Schiller-Universität Jena, 2021.
- [133] P. Salieres, A. L’Huillier, and M. Lewenstein, Phys. Rev. Lett. **74**, 3776 (1995).
- [134] A. Dalgarno and A. Kingston, Proceedings of the Royal Society of London. Series A. Mathematical and Physical Sciences **259**, 424 (1960).
- [135] M. Born and E. Wolf, *Principles of optics: electromagnetic theory of propagation, interference and diffraction of light* (Elsevier, 2013).
- [136] C. Chantler *et al.*, *X-Ray Form Factor, Attenuation and Scattering Tables* (NIST,

Gaithersburg, MD., 2005).

- [137] S. Hädrich *et al.*, J. Phys. B: At. Mol. **49**, 172002 (2016).
- [138] D. Veberic, arXiv preprint arXiv:1003.1628 (2010).
- [139] S.-F. Zhao, L. Liu, and X.-X. Zhou, Optics Communications **313**, 74 (2014).
- [140] S. G. Johnson, Quadgk.jl: Gauss-Kronrod integration in Julia, 2013.
- [141] P. K. Mogensen and A. N. Riseth, Journal of Open Source Software **3** (2018).
- [142] F. Köttig, D. Schade, J. Koehler, P. S. J. Russell, and F. Tani, Optics Express **28**, 9099 (2020).
- [143] C. Grebing, M. Müller, J. Buldt, H. Stark, and J. Limpert, Optics Letters **45**, 6250 (2020).
- [144] C. Vozzi, M. Nisoli, G. Sansone, S. Stagira, and S. De Silvestri, App. Phys. B **80**, 285 (2005).

EHRENWÖRTLICHE ERKLÄRUNG

Ich erkläre hiermit ehrenwörtlich, dass ich die vorliegende Arbeit selbstständig, ohne unzulässige Hilfe dritter und ohne Benutzung anderer als der angegebenen Hilfsmittel und Literatur angefertigt habe. Die aus anderen Quellen direkt oder indirekt übernommenen Daten und Konzepte sind unter Angabe der Quelle gekennzeichnet. Bei der Anfertigung dieser Arbeit haben mir meine Betreuer und die Koautoren oben genannter Publikationen geholfen.

Weitere Personen waren an der inhaltlich-materiellen Erstellung der vorliegenden Arbeit nicht beteiligt. Insbesondere habe ich hierfür nicht die entgeltliche Hilfe von Vermittlungs- bzw. Beratungsdiensten (Promotionsberater oder andere Personen) in Anspruch genommen.

Niemand hat von mir unmittelbar oder mittelbar geldwerte Leistungen für Arbeiten erhalten, die im Zusammenhang mit dem Inhalt der vorgelegten Dissertation stehen. Die Arbeit wurde bisher weder im In- noch im Ausland in gleicher oder ähnlicher Form einer anderen Prüfungsbehörde vorgelegt. Die geltende Promotionsordnung der Physikalisch-Astronomischen Fakultät ist mir bekannt. Ich versichere ehrenwörtlich, dass ich nach bestem Wissen die reine Wahrheit gesagt und nichts verschwiegen habe.

Jena, 24.10.2023

Björn Minneker

